THE UNIVERSITY OF
SYDNEY

DYNAMIC MODELING OF THE GEOLOGICAL CO_2 STORAGE IN FRACTURED AQUIFERS

–APPLICATION TO THE ORDOS BASIN CCS PROJECT

A thesis submitted in fulfilment of the requirements for
the degree of Doctor of Philosophy

Faculty of Engineering and Information Technologies
The University of Sydney

CAI LI

April 2016

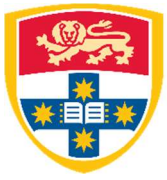

THE UNIVERSITY OF
SYDNEY

ABSTRACT

Unique reservoir performance was observed in the Shenhua (100,000 metric tons/year) Carbon Capture and Storage (SHCCS) Demonstration Project. Suggested by the reservoir pre-assessments, hydraulic fracturing and a multi-layer injection procedure were employed to improve the reservoir injectivity and to reduce the risk of overpressure. However, in-situ data showed that the total injection rate and the injection index increased over the years, while the corresponding injection initiation pressure decreased. No strong pressure build-up occurred in the reservoir. Although 21 saline aquifers were chosen to be the injection layers, only four of them did absorb CO_2 during all of the injection tests from 2011 to 2014. The other layers, including most of the hydraulically-fractured layers, stopped absorbing CO_2 in the injection tests after 2011. Additionally, the uppermost injection layer (with depths of 1690 m to 1699 m), which was unfractured, had a considerable increase in injectivity over the years and absorbed the majority of the injected CO_2 from 2012. It showed a potential to meet the injection target by itself without a strong pressure build-up.

Investigation into reservoir performance dynamics for this project was conducted through numerical simulations using TOUGH2-MP-ECO2N. The main features of the reservoir performance were reproduced through a heterogeneous model by using a time-dependent pressure boundary condition at the injection well and calibrating the permeability distributions in the injection layers against 2.5 years' historical data. Several scenarios were simulated to access the impacts of permeability distribution, induced fractures and the intermittent injection procedure on the reservoir performance.

The simulation results indicated that the heterogeneous distributions of permeability in the injection layers could be the cause for the dynamic reservoir performance shown by the monitoring data in the SHCCS Project. Predominance of the uppermost injection layer in absorbing CO_2 could be attributed to its much higher overall permeability than that of other injection layers. A substantial increase in injectivity of this layer over the years could be explained by the permeability becoming considerably higher away from the injection well in a north-westerly direction. The induced fractures in the reservoir greatly improved the injectivity at the beginning of the injection, but this improvement dramatically declined afterwards. The intermittent injection procedure employed in this project was helpful in retaining the pressure build-up low in the reservoir and kept the injection rate at the target level. The hysteresis effects accompanying the intermittent injection procedure could improve the injectivity and storage safety.

The reservoir performance from December 2013 to December 2015 was estimated by assuming that the injection procedure from December 2012 to December 2013 was repeated twice successively. The cumulative injected CO_2 mass reached 300,000 tons in December 2015, but the yearly average injection rate dropped slightly. The predicted results could be underestimated because the higher performance in the 2014 injection test was not accounted for in the calibration.

The sensitivity analysis showed that the model was most sensitive to boundary conditions. A closed lateral boundary condition could cause serious boundary effects for the simulation. The storage volume for CO_2 gained from the changes of pore volume response to injection pressure could be of significance if the reservoir had compressibility in the magnitude order of 10^{-9} pa^{-1} or greater. Changes in S_{lr}, S_{gr} and entry capillary pressure in this research did not show significant influence. The use of the rate boundary at the injection well made it more challenging to match the monitored pressure at the four points than the use of the pressure boundary. The main reason for this may come from the uncertainty in the rate allocation between the injection layers and the use of Darcy's law to describe the fluid flow in the well.

Key words:

Geological CO_2 storage, reservoir performance, dynamic modeling, history matching, the Ordos Basin, heterogeneity, injection procedure, hysteresis effects.

TABLE OF CONTENTS

LIST OF FIGURES

LIST OF TABLES

CHAPTER 1 INTRODUCTION

1.1 Background

Carbon capture and storage (CCS)，also known as carbon capture and sequestration, refers to the capture of CO_2 from large scale emission sources (like the traditional coal-fired power plants) and the storage of the captured CO_2 in the deep subsurface for a long period of time (White et al., 2003). CCS is an integrated three-stage process that includes (1) capture of CO_2 from large-scale coal- or gas-fired power plants or other industrial process facilities, (2) transport of the captured and compressed CO_2 to a suitable storage site, and (3) storage of the CO_2 by injecting it into deep underground rock formations, often at depths of 1000 m or more and overlain by impermeable formations that could prevent the injected CO_2 from migrating upward (GCCSI, 2015; USEPA, 2012).

CCS is indispensable to effectively respond to climate change (GCCSI, 2014). There is over 95% confidence that over 50% of the rise in the observed global average surface temperature from 1951 to 2010 has been caused by the anthropogenic increases in concentration of greenhouse gases and other human activities (IPCC, 2014). CO_2 emissions from fossil fuel combustion and industrial processes made up 55% to 65% of the total annual anthropogenic greenhouse gas emissions between 1970 and 2010 (IPCC, 2014). Given that demand for fossil fuels is most likely to remain as strong as today, reducing CO_2 emissions to the atmosphere is of great significance in the battle against global warming. As part of the portfolio of actions, CCS accounts for 14% of total energy-related CO_2 reductions needed by 2050 (IEA, 2014). Specifically, merely in the United States, CCS technologies can contribute 80% to 90% to the reduction of CO_2 emissions from fossil-fuel-combusted power plants, where over 40% of CO_2 emissions in this country come from (USEPA, 2012).

Geological CO_2 storage (GCS), by injecting supercritical CO_2 into deep geologic formations, has been studied for more than two decades as an option to reduce CO_2 emissions (Bachu, 2002; Bachu, 2015; Bachu and Adams, 2003; Herzog et al., 2000; Hitchon et al., 1999; Holloway, 1996, 2005; IPCC, 2005; van der Meer, 1992; White et al., 2003). Earlier CO_2 storage projects and over 30 years' experience in CO_2–enhanced oil recovery (EOR) have proved that long-term storage is feasible in geologic formations selected appropriately (Benson, 2006). Deep saline aquifers, depleted oil or gas fields and unmineable coal seams are

commonly considered as viable reservoirs for GCS. Among the three options, deep saline aquifers are believed to be the most promising candidates because of their widespread presence all over the world and huge potential storage capacities (Bachu and Adams, 2003; IPCC, 2005).

Injectivity is one of the key factors for GCS, because it indicates the ease with which a fluid can be injected into a formation and it often relates to the storage capacity of the reservoir (Bachu, 2015; Eiken et al., 2011). Injectivity is defined as the injection rate divided by the pressure difference at the well (kg/(s*Pa)) (IPCC, 2005), or the product of the permeability of the aquifer and its thickness (Darcy-meter, Dm) (Hosa et al., 2011). For projects that employ reservoirs with low porosity and low permeability, injectivity usually poses a big challenge on them, like the CCS operations on In Salah and Snøhvit (Eiken et al., 2011). Injectivity can be improved by increasing the number of injection wells, or by creating higher conductivity paths in the aquifers surrounding the wellbores through hydraulic fracturing (Bachu, 2015; Goodarzi et al., 2011; Lucier and Zoback, 2008; Raziperchikolaee et al., 2013).

However, some negative effects may associate with injectivity improvement. For example, at In Salah, three wells were drilled to the same reservoir zone to facilitate the injection, but pressure at the bottomhole was believed to be still considerably high and probably caused hydraulic stimulation of fractures within the reservoir (Eiken et al., 2011). A few centimeters of uplift on the surface was observed around the injection wells (Ringrose et al., 2009; Vasco et al., 2008). Breakthrough of CO_2 from one of the injection wells was detected in a suspended appraisal well nearby, resulting in the appraisal well being plugged and abandoned (Ringrose et al., 2009). Therefore, the issues associating with injectivity improvement also needed to be weighted when evaluating the reservoir performance for a real project.

1.2 The SHCCS Demonstration Project in the Ordos Basin in China

The Shenhua Carbon Capture and Storage (SHCCS) Demonstration Project was the first pilot project for geologic storage of CO_2 in saline aquifers in China, as well as the first coal-based CCS pilot project with an entire chain from capture to storage (Wu, 2014). This project was designed to capture and store 100,000 metric tons of CO_2 per year for a coal-to-gasoline factory in the Shenhua Group. The project started CO_2 injection in May 2011.

The pre-injection assessments showed that the target injection rate could not be met by a single injection layer and that the resulting pressure build-up was highly likely to exceed the safety limit over a short period (Wang et al., 2010; YLHYOIL, 2010). To improve the

injectivity of the reservoir and to reduce the risk of overpressure, hydraulic fracturing and a 21-layer injection procedure were employed to increase the reservoir injectivity to meet the injection target and reduce the overpressure risk (Wu, 2014).

However, unique reservoir performance was observed in this demonstration project. From May 2011, a 16-day injection test, including four cycles of two-day injection followed by two-day shut-in, was conducted annually to evaluate the reservoir performance. In each of the annual tests, injection profile logging was applied to measure the pressure, temperature and flow rates into each injection layer. In-situ data showed that the total injection rates in the annual injection tests from 2011 to 2014 increased over the years, along with a large decrease in the wellhead and bottomhole injection pressure and a several-fold increase in the injection indexes. No strong pressure build-up was observed in the reservoir after the injection started. Only four out of the 21 injection layers remained absorbing CO_2 through the annual injection tests from 2011 to 2014, and other injection layers, including most of those being artificially fractured, stopped absorbing CO_2 after the 2011 injection test. Additionally, the uppermost injection layer, which was not hydraulically fractured, grew substantially in injectivity during the injection tests, and became the critical layer by absorbing over 60% of the injected CO_2 from 2012. Such a substantial increase in injectivity made the uppermost injection layer potentially capable of meeting the injection target by itself.

1.3 Research Objectives

To understand why the reservoir in the SHCCS Project behaved in such unique way, research was conducted with the following objectives:

(1) To develop numerical modelling approaches to capture the dynamic process of CO_2 flow in fractured aquifers.

(2) To calibrate the developed model with field data obtained from the SHCCS project and explore explanations for the unique pattern of reservoir performance in this project.

(3) To assess the impacts of hydraulic fracturing and injection procedures on reservoir performance, including injectivity change during injection.

1.4 Outline of the Thesis

There are eight chapters in this thesis.

Chapter 1 gives introduction to this research.

Chapter 2 is a literature review, focusing on modeling approaches and describing the multiphase and multi-component system where pure CO_2 is injected into a deep saline aquifer, and the means of depicting the fractures in the aquifer reservoir. Existing studies relevant to the SHCCS Demonstration Project are also summarized in this chapter.

Chapter 3 provides detailed information about the SHCCS Demonstration Project, with respect to experiments in the project, like hydraulic fracturing operations, injection procedures, experimental data processing and reservoir performance assessment methods.

Chapter 4 is about the model development for this project, including setup, choices of the key parameters for numerical simulations and how the model was calibrated.

Chapter 5 presents the results of the experimental analysis of reservoir performance in this project.

Chapter 6 shows the results from numerical simulations, including the analysis of 'goodness of fit' between the simulated results and the monitoring data, the impacts of reservoir heterogeneity, the hysteresis effects and injection procedures on reservoir performance, and the sensitivity analysis of this model.

Chapter 7 provides suggestions on dynamic reservoir performance assessment and injection procedure design for a low permeability and low porosity reservoir.

Chapter 8 draws the main conclusions from the simulation results in this research.

CHAPTER 2 LITERATURE REVIEW

2.1 Synopsis

This chapter reviews the literature regarding general equations that govern a CO_2-brine system, approaches for modeling a fractured reservoir and model applications for some geological CO_2 storage sites. The studies regarding dynamic reservoir performance simulation for the SHCCS project are given at the end of this chapter.

2.2 General Governing Equations in a CO_2-Brine System

Injection of a large amount of supercritical CO_2 into a deep saline aquifer for carbon storage creates a multiphase, multi-component flow system. In this system, there are mainly two phases: the aqueous phase (brine) and the 'gas' phase (CO_2-rich phase, if no distinction is made between the gaseous CO_2 and the liquid CO_2), and three mass components: water, salt and CO_2. There may also be present a solid phase of salt and other components, like rock minerals.

CO_2 movement in such a system involves associated processes of multiphase fluid flow, heat transfer, geochemical reactions and mechanical effects. The governing equations to describe this system can be different, depending on which process is the most significant within the time and spatial scales of the storage process involved. The basic equations of mass and energy balance are generally dealt with in all models.

Mass Balance Equations

A basic mass balance equation for the mass components in the system can be written as follows:

$$\frac{\partial}{\partial t}\sum_{\beta}(\rho_{\beta}\phi s_{\beta}m_{\beta}^{\kappa})+\sum_{\beta}\left[\nabla\bullet(\rho_{\beta}\mathbf{u}_{\beta}m_{\beta}^{\kappa}+\mathbf{j}_{\beta}^{\kappa})\right]=\sum_{\beta}q_{\beta}^{\kappa} \qquad (2\text{-}1)$$

where β is labeling the phase (aqueous or gas), κ stands for the mass component (CO_2, H_2O, salt), ρ_{β} is the density of phase β, ϕ is porosity of the aquifer, s_{β} is the saturation of fluid phase β (the fraction of pore volume occupied by phase β), m_{β}^{κ} is the mass fraction of component κ

in phase β, $\mathbf{u}_\beta$ is the volumetric flux vector (or Darcy flux) for phase β, $\mathbf{j}_\beta^\kappa$ is the non-advective flux vector (due to diffusion and hydrodynamic dispersion) for component κ in phase β, and q_β^κ are the external sources or sinks of mass for component κ in phase β. These mass balance equations need to be augmented by constitutive equations and equations of state (EOS).

$\mathbf{u}_\beta$, the Darcy flux of phase β, is normally written as:

$$\mathbf{u}_\beta = -\frac{k_{r\beta}\mathbf{k}}{\mu_\beta} \bullet (\nabla p_\beta - \rho_\beta \mathbf{g}) \qquad (2\text{-}2)$$

where $k_{r\beta}$ is relatively permeabilityle to phase β, μ_β is the viscosity of phase β, $\mathbf{k}$ is the absolute permeability tensor, p_β is the pressure of phase β, and**and** $\mathbf{g}$ is the gravitational acceleration vector.

p_β is calculated by:

$$p_\beta = p + p_{c\beta} = p + p(s_\beta) \qquad (2\text{-}3)$$

where p is the pressure of a reference phase (usually taken to be the aqueous gaseous phase) and $p_{c\beta}$ is the capillary pressure of phase β, which relates to the saturation of phase β.

The diffusive flux in $\mathbf{j}_\beta^\kappa$ is usually written in a form of Fick's law, as being in proportion to the gradient of mass fraction of κ, and the dispersive flux can be written as follows:

$$\mathbf{F}_{dis\beta}^{\kappa} = -\sum_\beta \rho_\beta \overline{\mathbf{D}}_\beta^\kappa \nabla m_\beta^k \qquad (2\text{-}4)$$

where $\overline{\mathbf{D}}_\beta^\kappa$ is the hydraulic dispersion tensor (De Marsily, 1986).

Constraints on mass fractions and saturations in the system are $\sum_\kappa m_\beta^\kappa = 1$ (for both phases) and $\sum s_\beta = 1$, respectively.

Partitioning of H_2O and CO_2 in a system where aqueous and gas phases coexist can be calculated from correlations developed by Spycher and Pruess (2005), where the equilibrium composition of aqueous and gas phases can be predicted as functions of temperature, pressure and salinity. The functions developed by Spycher and Pruess (2005) are valid for temperatures from 12°C to 110°C, for pressures up to 60 MPa, and for salinity up to saturated NaCl brines.

The density and viscosity of the involved phases in the system can also be modeled as functions of temperature, pressure, composition and partitioning of components among these phases (Altunin, 1975; Haas Jr, 1976; Himmelblau, 1959; Phillips, 1981; Span and Wagner, 1996).

Energy Balance Equations

Similarly, when thermal equilibrium is assumed, the energy balance in the system is written as follows:

$$\frac{\partial e_t}{\partial t} + \nabla \bullet \mathbf{f}_t = Q_t \tag{2-5}$$

$$e_t = \phi \sum_{\beta} \rho_\beta s_\beta v_\beta + (1-\phi)\rho_R c_R T \tag{2-6}$$

$$\mathbf{f}_t = \sum_{\beta} \rho_\beta \mathbf{u}_\beta h_\beta - \lambda \nabla T \tag{2-7}$$

where, Q_t is the external thermal source or sink, v_β is the specific internal energy in phase β, ρ_R is the grain density of rock, c_R is the specific heat of rock, T is temperature, h_β is the specific enthalpy in phase β and λ is thermal conductivity.

Solutions to the governing equations presented above provide the basis of practical models for CO_2 injection and migration in saline aquifers. Due to the multi-phase system, capillary pressure and relative permeability lead to a highly non-linear set of partial differential equations. Moreover, a set of geochemical reactions and the equations for geomechanics are sometimes coupled with component mass balance equations, which makes these equations even more complicated. Such fully-coupled models are conceptually straight forward, but practically, it is extremely computationally demanding, and so far no fully-coupled simulation has been achieved for the carbon storage system (Celia et al., 2015). Therefore, practical simulations usually maintain the equations of flow, and a few other equations (energy equations and geomechanic equations, geochemistry equations) depending on which process is of most interest, how the problem is set up, and the availability of data and information about CO_2 storage.

2.3 Approaches for Modeling Fractured Reservoirs

Significant progress has been made in the numerical simulation of fluid flow and transport processes in fractured reservoirs since the 1960s. The common modeling approaches

include the dual-porosity model (Barenblast and Zheltov, 1960; Warren and Root, 1963), the multiple interacting continua (MINC) model (Pruess, 1985), the dual-porosity and permeability model (Gilman and Kazemi, 1988; Hill and Thomas, 1985; Quandalle and Sabathier, 1989; Zhang et al., 2000; Zhang and Woodbury, 2000), and the discrete fracture network (DFN) model (Cacas et al., 1990b; Dershowitz and Lapointe, 1994; Jafari and Babadagli, 2012; Long et al., 1982; Narr et al., 2006; Parney et al., 2000; Woodbury and Zhang, 2001; Zhang and Woodbury, 2002).

Dual-porosity models are commonly thought to be the simplest way to describe a fractured reservoir. Barenblast and Zheltov (1960) first proposed this approach by treating the porous matrix and the fracture network as two superimposed and mutually communicating media with different porosities. Warren and Root (1963) later improved this approach by including permeability as another characterizing parameter for the two media systems. A fractured porous medium is idealized by identical rectangular matrix blocks, separated by an orthogonal network of fractures (Figure 2-1). The fracture network is assumed to be the path where fluid flow occurs, and the matrix blocks are assumed to be the fluid containers to feed the fractures. Both fracture permeability and matrix permeability are assumed to be independent of stress and pressure, and are constant during simulation. Dual-porosity models are useful in describing the interaction between matrices and fractures, but they are too simple to capture the complex structure of fracture networks and are limited to describing the dynamic process of reservoir permeability response to stress and pressure.

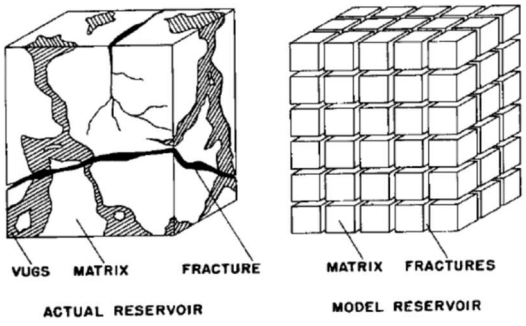

Figure 2-1 Dual-porosity model (Warren and Root, 1963).

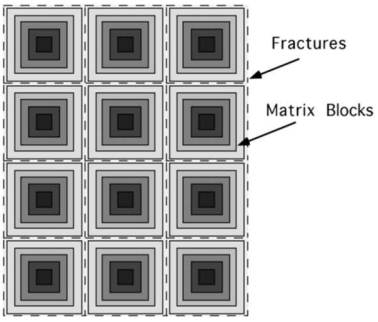

Figure 2-2 MINC model (Pruess, 1985).

The MINC model by Pruess and Narasimhan (1985) discretizes the matrix block into smaller units (Figure 2-2). This model is based on the notion that the propagation of changes in fluid pressure (or temperature, phase composition, etc.) in response to the presence of sinks or sources (production or injection wells) is rapid through the fracture system, while it is much slower in the matrix. Therefore, changes in matrix conditions are locally controlled by the

distance to the fractures. Fluid and heat flow from the fractures into the matrix blocks, or vice versa, can then be modeled by means of one-dimensional strings of nested grid blocks, as shown in Figure 2-2. This approach is often used to simulate fractured geothermal systems and has been implemented in TOUGH2 (Pruess et al., 1999) to address multiphase fluid and heat flows in fractured porous media. The MINC approach is very efficient because it substantially reduces the computational cost by modeling a 3-D fractured porous system as a 1-D problem. However, the specification of equivalent hydraulic properties, especially permeability for the fracture network, is not easy. This approach is not applicable to a system where fracturing is too sparse to be approximated as a continuum (Pruess et al., 1999). The concept of 'dual permeability' model was introduced by Hill and Thomas (1985), assuming that Darcian flow occurs in both the fracture blocks and the neighboring matrix blocks, which is different from the dual-porosity model, where flow is assumed to occur only in the fractures. Gilman and Kazemi (1988) and Quandalle and Sabathier (1989) developed two numerical simulation models based on the dual-porosity-permeability approaches. The dual-porosity-permeability models provide a more practical method for simulating the fluid flow in fractured reservoirs than dual-porosity models.

The discrete fracture network (DFN) approach originated from the effective medium theory by Kirkpatrick (1973), which was developed and applied in modeling fluid flow in fractured porous media by Long et al. (1982), Cacas et al. (1990) , David et al. (1990), Dershowitz and Lapointe (1994), Parney et al. (2000), Narr et al. (2006), and Jafari and Babadagli (2012). The underlying idea of this model is to infer an average conducting parameter for the heterogeneous disordered media from the statistics of local conducting elements. In the DFN approach, a grid block containing fractures is deemed an effective medium, which is defined as a homogeneous equivalent network for which the macroscopic conductive (transport) properties are the same as for the heterogeneous system (David et al., 1990). Therefore, the hydraulic conductive property of the grid block can be expressed as an equivalent value. For instance, the real permeability of a grid block can be represented by an equivalent fracture network permeability tensor (Long et al., 1982), which is dependent on the fracture connectivity and the fracture geometry (length, aperture and orientation). Some contributions of interest have been made to calculate the equivalent fracture network permeability; for example, by Oda (1985), Long et al. (1985), Cacas et al. (1990a), Odling (1992), Lough et al. (1997), Bourbiaux et al. (1998), Nakashima et al. (2000), Teimoori et al. (2003), Min et al. (2004), and (Jafari, 2011). A dynamic modeling approach can be achieved

by defining the equivalent values of the transport properties for each grid block in the fractured system (Jafari, 2011). The DFN approach is suitable when modeling an inhomogeneous geological medium with a complex fracture network (Parney et al., 2000). The DFN models are more capable of addressing the connectivity characteristics of fracture networks than the dual-porosity models (Dershowitz et al., 2000). However, the DFN models are still limited to modeling a fractured reservoir with complicated dynamic processes due to their complex fracture geometry (Jafari, 2011).

2.4 Applications to Geological CO_2 Storage Sites

Various CO_2 projects around the world, from a pilot scale that injects thousands to hundreds of thousands of metric tons of CO_2 in a short duration to a large scale that injects millions of metric tons of CO_2, effectively addressed specific technical problems for CO_2 storage, like monitoring CO_2 movement in the deep reservoirs, modeling reservoir, and calibrating models by using field data. Modeling studies of various scale injections into deep saline aquifers are reviewed in this section, with a focus on how modeling research can help to understand the reservoir behavior in geological CO_2 storage. The large-scale injection projects discussed in this section include the ongoing Sleipner Project (injecting one million metric tons of CO_2 per year since 1996) into the North Sea, the In Salah project (injecting 0.5 million metric tons of CO_2 per year from 2004 to 2011) in Algeria, the Snøhvit Project (injecting 0.5 million to 0.7 million metric tons of CO_2 per year since 2008), the Cranfield Project (injecting over one million tons of CO_2 in a few years), and the Decatur Project (injecting one million tons of CO_2 in three years). The former three are the main industrial-scale projects in saline aquifers. The pilot-scale projects discussed here include the Frio CO_2 injection experiment project, the Otway Project in Australia, and the Ketzin Project in Germany.

The Sleipner injection site is thought to be the most successful and most studied CO_2 injection operation in the world (Celia et al., 2015). The striking feature of this reservoir is that the thick storage formation (184 m) consists of a series of very high permeability (about two Darcy, or 2×10^{-12} m^2) and porosity (about 35%) sandstone layers in tens of thicknesses interbedded within much thinner (<1 m) shale layers. The net-to-gross ratio reaches 95% (Eiken et al., 2011). CO_2 was injected into the lower part of the formation under the lowest shale baffle and it was found to rapidly migrate upward and get through the shale layers to reach the top shale barrier in the formation (Singh et al., 2010). By using mass balance measures and percolation-type simulations, Cavanagh and Haszeldine (2014) postulated that

the existence of micro-fractures in the shale lenses allows the CO_2 to seep through. The CO_2 plume in the uppermost layer was simulated through vertical equilibrium models and calibrated with seismic data by some researchers; for example, Nilsen et al. (2011), Bandilla et al. (2014), and Cavanagh and Haszeldine (2014). Other studies (Cavanagh and Haszeldine, 2014; Gasda et al., 2013) concluded that fluid temperature had a significant impact on CO_2 migration in the uppermost layer. A reactive transport simulation for this project indicated that the magnitude of the reduction in the reservoir's permeability and porosity, due to geochemical reactions, is nearly negligible (Johnson et al., 2004).

Unlike the Sleipner site, the In Salah injection site in Algeria is characterized as a thin formation (20 m) with low permeability (around 10 mD, or 10^{-14} m^2) and porosity (about 15%). This project distinguishes itself by detecting surface elevation changes using interferometric synthetic aperture radar (InSAR). There was up to 20 mm of uplift observed around the injection wells over the injection period. Geomechanics simulations inferred that the measured surface uplift was mainly caused by the elevated pressure near all the injection wells, and the double-lobed uplift at KB-502 closely related to a high permeability, vertical fault/fracture zone running through one of the injection wells (Bond et al., 2013; Gemmer et al., 2012; Iding and Ringrose, 2010; Morris et al., 2011; Rinaldi and Rutqvist, 2013; Ringrose et al., 2009; Rutqvist et al., 2010; Vasco et al., 2008; Vasco et al., 2010).

The reservoir for CO_2 storage at Snøhvit is characterized by a 2700m-deep sandstone-dominating formation interlayered with shales and minor coals, having porosities of 10% to 15%, permeabilities of 185 mD to 883 mD and high net-to-gross ratios (Estublier and Lackner, 2009; Maldal and Tappel, 2004). Faults exist in the reservoir as the formation is situated in a faulted block with throws over 200 m (Eiken et al., 2011). The injection started in April 2008 and was supposed to dispose about 23 million metric tons of CO_2 for the 30 years. Pressure in the reservoir grew quickly as the injection was conducted at the planned rate. The injection was stopped for a few times to allow the reservoir to recover, but even a 4.5-month stop was not long enough to stabilize pressure (Shi et al., 2013). 4D seismic survey indicated that only a small part at the lower reservoir received most of the CO_2 (Eiken et al., 2011; Shi et al., 2013). Numerical simulations were used not only to evaluate the safety of long-term storage (Estublier and Lackner, 2009; Maldal and Tappel, 2004; Pham et al., 2011), but also to assess injection performance by matching the injection well pressure history over 32 months (Shi et al., 2013). A model domain considerably smaller than the whole reservoir formation was found to be necessary for fitting the flowing bottomhole pressure history by Shi et al. (2013). Both facies

modeling and 4D seismic mapping indicated that lateral heterogeneities in fluvial deposition environment made a major contribution to reduction in effective permeability, and in turn, the CO_2 injectivity (Eiken et al., 2011; Shi et al., 2013).

The Cranfield project, running since December of 2009, has injected more than one million metric tons of CO_2 into a 3200m-deep brine-leg of an operating oil field near Natchez, Mississippi, in the U.S. This project set a record for the deepest application of electrical resistance tomography (ERT) for tracking the movement of CO_2 in saline aquifers (Doetsch et al., 2013). Multiple flow paths were found to exist in both cross sections between the two monitoring wells (F2 and F3) where CO_2 migration was imaged by ERT (Doetsch et al., 2013); times of CO_2 arrival at F2 and F3 were different, shown by tracer tests (Doetsch et al., 2013). Doetsch et al. (2013) successfully demonstrated that ERT-derived resistivity distribution and gas composition data could be coupled in iTOUGH to invert the reservoir width and permeabilities for a simplified layer-wise model. Heterogeneity and channeling in the reservoir were believed to be the cause of the multiple flow paths between the two monitoring wells (Doetsch et al., 2013). Hosseini et al. (2013) discussed a systematic approach for reservoir characterization and numerical simulation of CO_2 sequestration for this project. Integrating various dynamic data into the initial static model seemed challenging, but effective in reducing the uncertainty of model parameters, and the relative permeability curves were found to be an important factor affecting pressure response and plume extent in the reservoir in this study.

The Decatur Project in Illinois injected about one million metric tons of CO_2 from November 2011 to November 2014, with a goal of demonstrating the safety of CO_2 injection and the capability of existing monitoring techniques to track CO_2 plumes (Finley, 2014). Experience from this pilot project enabled the expansion to a commercial-scale operation (Gollakota and McDonald, 2014). The Mt Simon Formation, which was chosen to be the reservoir for CO_2 storage, displayed quite laminated distribution of porosity and permeability in this interval (Senel et al., 2014). The lower part of this formation, which has the highest porosities and permeabilities, was selected to be the primary injection zone; while the middle part, which has much lower porosities and permeabilities, was believed to be able to greatly retard the upward migration of CO_2. Progressively-updated models were used to simulate the CO_2 storage for this project, and the latest updated model was calibrated against the pressure histories in the injection well and the verification well, and the time-lapse CO_2 saturation profiles around the two wells, by manually adjusting the permeabilities, skin factors and relative permeability curves in sequence (Senel et al., 2014).

Pressure effects from the injection of hundreds of millions metric tons of CO_2 into a large basin could be significant, according to some numerical studies on hypothesized massive amounts of CO_2 being injected through multiple wells into the Illinois Basin in the U.S. (Bandilla et al., 2012; Birkholzer et al., 2009; Person et al., 2010; Zhou et al., 2010). Simulated results showed that although the CO_2 plumes remained relatively localized, the pressure perturbations spread throughout the basin with significant overlap and there was interaction between the pressure perturbations associated with each injection location. The pressure response to the assumed massive injection was found to be sensitive to the choice of compressibility values in the models.

The Frio CO_2 injection experiment in the U.S. injected about 1,600 metric tons of CO_2 over 10 days into a fault block in a formation at a depth of about 1,500 m underground. Impacts of reservoir heterogeneity on CO_2 storage and appropriate techniques to measure the CO_2 plume evolution were studied in this project (Doughty and Pruess, 2004; Hovorka et al., 2006; Hovorka et al., 2004). The experiment proved successful in measuring and modeling the CO_2 injection, and the conceptual model of CO_2 migration over short space and time scales was validated (Celia et al., 2015; Doughty et al., 2008).

The Ketzin Project in Germany injected 70,000 metric tons of CO_2 into a formation at a depth of 630-650 m from 2008 to 2013 (Martens et al., 2012). Studies on site characterization from seismic data, dynamic simulation of reservoir behavior, reservoir heterogeneity impacts on CO_2 plume distribution and storage safety assessment, were found in many publications (Kempka et al., 2013a; Kempka et al., 2013b; Kempka and Kühn, 2013; Kempka et al., 2010; Klein et al., 2013; Lengler et al., 2010; Norden and Frykman, 2013; Wiese et al., 2010; Würdemann et al., 2010). This project demonstrated that the applied monitoring techniques were able to detect the CO_2 plume. Three different simulators (ECLIPSE 100, ECLIPSE 300, and MUFTE-UG) were tested for estimating the arrival times of CO_2 in the first monitoring well (CO2 Ktzi 200/2007), and results from these simulators showed a good match with the measured arrival times at the well with deviations of 8.1%, 9.2% and 17.7%, respectively, by using the real injection regime (Kempka et al., 2010). However, the arrival times of CO_2 in the second monitoring well (CO2 Ktzi 202/2007) could not be matched by these codes in the same way. Kempka and Kühn (2013) demonstrated that both ECLIPSE and TOUGH2-MP could match the observed arrival times of CO_2 in the two monitoring wells and reservoir pressure by differently modifying the permeabilities of the near- and far-field well areas in the geological model refined with incorporation of a facies-based heterogeneity near the wells.

The Otway Project in Australia was a successful demonstration of the CO_2 storage in a depleted gas field (Underschultz et al., 2011). In the first experiment, 65,445 metric tons of CO_2 were injected into a formation at a depth of 2,060 m over a period of 17 months. In the second experiment, 150 metric tons of pure CO_2 were injected into the reservoir and then 454 metric tons of formation water were successively injected in order to investigate the residual trapping in the reservoir (Paterson et al., 2013). All of the methods deployed in the study were able to measure residual trapping with varying accuracies. Before the dynamic model to predict the CO_2 migration in the depleted field, it was calibrated by adjusting bulk and relative permeability to match the pressure history prior to the injection. Simulation results from the latest dynamic model for the project generally reproduced the vertical distribution of CO_2 concentration in the reservoir gained from the U-tube sampling system installed in the well, but

As discussed above, different modeling approaches can be applied to carbon storage. Usually, the choice of modeling approach depends on the scale of the problem, the aspect of interest and the available data. However, modeling results can be sensitive to many factors, often the bulk permeability and relative permeabilities. Several studies have been conducted to investigate the impact of these factors on simulation results. Pruess et al. (2002) concluded that different simulators tended to agree with each other, and that any discrepancies stemmed mainly from different representations of fluid properties. Model calibration in these projects mentioned above followed the history-match convention that matches the simulated pressure in the reservoir and/or the arrival times of CO_2 in certain places with the measurements by mainly adjusting the reservoir permeability and/or relative permeability for the dynamic model under a given injection rate regime. Nevertheless, this traditional way to calibrate the dynamic model for a project may not be effective when the injection rate records were fragmented but the injection pressure records were continuous. In this situation, reverse of the data and boundary conditions by using injection pressure as input to mimic the injection rate or cumulative injected mass, would be more sensible.

2.5 Dynamic Reservoir Simulation in the SHCCS Project

Modeling of CO_2 storage in the reservoir of this project can be found in some recent publications, which can assist in the understanding of the geo-hydrological, thermal, mechanical and geochemical processes involved in CO_2 movement in saline aquifers. Zhang et al. (2012), taking this project as a case, demonstrated that three different approaches to

represent the wellbore in a simulation (i.e., fixed pressure in the top screen, distributed pressure, and injection from a virtual element of the grid) could result in different allocation of injected CO_2 among different layers when TOUGH2-ECO2N (Pruess, 2005) was used to simulate CO_2 movement in saline aquifers, and advised that an approach that best represents the field operation should be chosen. Ling et al. (2013) predicted the pressure evolution and CO_2 movement in the reservoir with a three year constant-rate injection plan, and evaluated the reservoir storage capacity and the role of hydraulic fracturing to improve injectivity. They estimated that the maximum travel distance of CO_2 in 3 years could be up to 350 m, and indicated that hydraulic fracturing could greatly facilitate the injection. Liu et al. (2014) studied the effects of temperature, injection rates and lateral model boundary conditions on CO_2 movement in the reservoir for 500 years, and concluded that the injection could also cause a significant pressure perturbation in the reservoir and that injection temperature and rate were the two most influential factors governing the CO_2 plume in the reservoir. Kuang et al. (2014) indicated that the injection rate would greatly affect the CO_2 phase composition and the pH distribution in the reservoir. Bandilla et al. (2014) analyzed the thermo-hydro-mechanical (THM) response of the reservoir to the injection using a 2D THM model, with a focus on the mechanical process, and suggested an uplift of tens of centimeters at the surface. Wei et al. (2014) studied the influence of sub-core scale structure heterogeneity on the flooding properties of the sandstone in the dominant injection layer through experiments and numerical simulations, and concluded that sub-core porosity heterogeneity would notably affect the CO_2 migration. Jiang et al. (2014) focused on the thermal process in the injection well and found that heat extraction from rocks, CO_2 compressibility, and loss in potential energy were three factors contributing to the increase in CO_2 temperature in the well from the wellhead to the bottom, but their contribution share depended on the injection rate and temperature. Liu et al. (2015) evaluated the mineral trapping capacity of the formations in the reservoir by simulating the chemical reactions between CO_2-brine-rock on four sandstone samples, and concluded that the uppermost injection formation had the highest mineral trapping capacity. Though Xie et al. (2015a, 2015b) did not present a good match of the simulated reservoir pressures to the monitored data, their results suggested high safety of long-term CO_2 storage in the reservoir. Core-flood experiments were conducted under pressure over 8 MPa and temperature constantly at 40 ℃ on sandstones sampled from the Formations of Liujiagou and Shanxi in this project, with an aim to study dynamic displacement, non-equilibrium dissolution of supercritical CO_2 and mass transfer in porous medium with low permeability (Chang et al., 2014; Chang et al.,

2013). Absolute permeability and porosity of these cores were found to be less than 1 mD and between 12.4% and 15.10%, respectively. Results from the CO_2-flood tests indicated that the relative CO_2 permeability at the measured water residual saturation of 0.52 could be in the range from 0.13 to 0.23 (Chang et al., 2013). Non-equilibrium dissolution of CO_2 observed in the water-flood experiments suggested that the dissolution of supercritical CO_2 during displacement made free-phase CO_2 more mobile through the cores and may enhance the effects of snap-off, which could result in more CO_2 trapped (Chang et al., 2014; Chang et al., 2013). Most of the studies placed their emphasis on the long-term post-injection storage safety of the project. Their positive results helped to build up confidence on this project.

Although the studies mentioned above have contributed important knowledge about the storage process in the reservoir to this project, a unique pattern of reservoir responses has not been studied in depth yet. The monitoring data collected in-situ showed that the injectivity of the uppermost injection layer, which was hydraulically fractured, rose largely with the injection time. During the four annual injection tests from 2011 to 2014, the CO_2 mass ratio in this layer increased from around 10% in 2011 to nearly 90% in 2014, and the total injection mass rate also increased from below the target to well above it. These observations indicated that only this layer itself could meet the target rate. Meanwhile, the injection initiation pressure at the well head in the injection tests decreased about 30% over the four years. These tendencies indicated that the it was becoming easier to inject CO_2 into the reservoir. Moreover, no strong pressure build-up was observed in this site (Jiang et al., 2014; Xie et al., 2015a; Xie et al., 2015b). The reservoir showed a very dynamic performance, different from the previous estimation by Wang et al. (2010) and YLHYOIL (2010).

In this thesis, the reservoir performance was investigated through numerical simulations with a comparison against 2.5 years' historical monitoring data. This study significantly differed from previous studies in the following aspects. Firstly, the heterogeneity in permeability and porosity in the injection layers was fully considered, unlike the homogeneous models used in the previous research (Bandilla et al., 2014; Jiang et al., 2014; Ling et al., 2013; Liu et al., 2014; Xie et al., 2015b). Secondly, 2.5-year injection rate, cumulative mass and pressure applied in the model were reconstructed from the available monitoring data. Thirdly, the reservoir performance was assessed for the period from December 2013 to December 2015 in that concerns with CO_2 cumulative injection mass if the injection procedure continued as from December 2012 to December 2013. Finally, reservoir heterogeneity, hydraulic fracturing, injection procedures and hysteretic effects on reservoir

performance were discussed in this study. Results from this research will help to further understand the reservoir dynamics in this project, and give explanations about why the reservoir acted the way it did.

CHAPTER 3 METHODS

3.1 Synopsis

This chapter presents the characterization of the SHCCS Project site, the injection operations conducted in this project, monitoring data that have been obtained and the method of data processing.

3.2 Demonstration Site

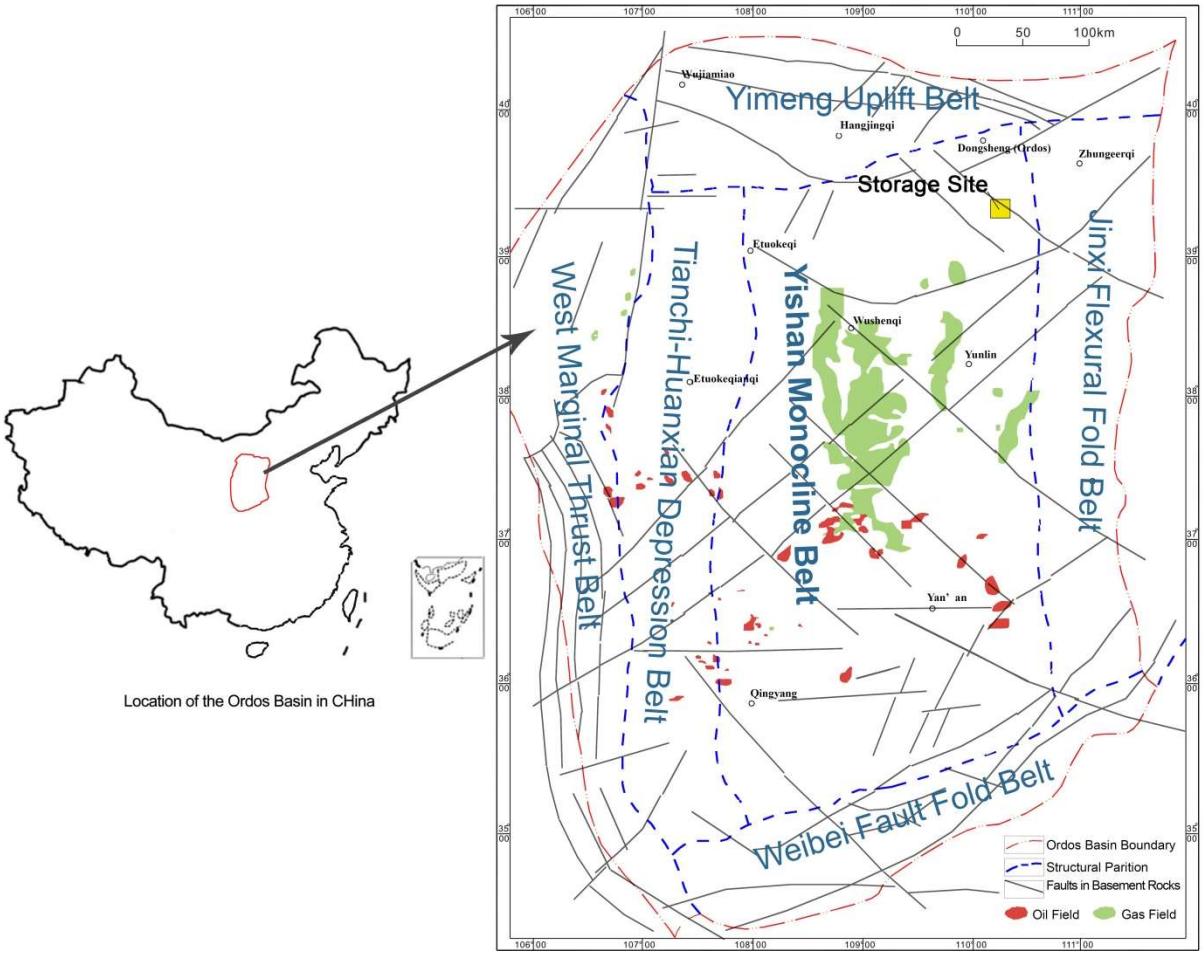

Figure 3-1 Location of the storage site in the tectonic background of the Ordos Basin (modified from He (2003)).

3.2.1 General Geological Settings

The storage site is onshore, located in the Inner Mongolia Autonomous Region of China. It lies in the northeast of the massive Yishan Monocline in the Ordos Basin (Figure 3-1). The Ordos Basin, a typical cratonic basin developed on the Archaeozoic to Proterozoic

metamorphic rock series, has two major hydrocarbon systems: the Paleozoic gas system and the Mesozoic oil system (Yang et al., 2005). The sedimentary strata in this basin includes three major sequences: early Paleozoic, late Paleozoic and Mesozoic, with a total thickness ranging between 4000 m and 6000 m (Xiao et al., 2005). The Yishan Monocline, the major tectonic sub-partition with a very gentle slope from northeast to southwest, accommodates the majority of oil and gas fields in the Ordos Basin. The presence of hydrocarbon reservoirs demonstrates that there are highly effective geological sealing features in this region. Therefore, the geological background of the storage site is suitable for CO_2 sequestration, meeting the general criteria for site selection, suggested by Bachu (2000).

3.2.2 Candidate Formations

A seismic survey, covering an area of about 175 km^2, was conducted on the site in 2010 to reveal the main structural characteristics of the formations at depths of 1500 m to 3000 m. Characteristics of fault occurrences, potential combinations of reservoir, seal, and spread features, and hydraulic properties of the potential reservoirs, were identified or estimated in this survey (He et al., 2010). The involved strata, from top to bottom, includes the Heshanggou Formation (T_{1h}) and the Liujiagou Formation (T_{1l}) in the lower Triassic Series, the Shiqianfeng Formation (P_{3s}), the Shihezi Formation (P_{2sh}), the Shanxi Formation (P_{1s}) and the Taiyuan Formation (P_{1t}) in the Permian System, the Benxi Formation (C_{2b}) in the lower Carboniferous Series, and the Majagou Formation (O_{2m}) in the lower Ordovician Series.

145 faults in total were interpreted from the seismic data with three different levels of confidence. Figure 3-2 shows the tectonic structures at the bottom of the five formations of T_{1l}, P_{3s}, P_{2sh}, P_{1t} and O_{2m}, respectively. Only 15 faults were confirmed, nine faults were considered highly likely to exist, and the remainder were merely suspected. The confirmed and highly-likely faults developed in the northern part of the site, several kilometres away from the injection well location, and mainly vertically intersected the three formations of P_{2sh}, P_{1t}, and O_{2m}. The suspected faults have the most dense population in the T_{1l} formation.

Five potential combinations of reservoir and seal, from top to bottom, in the systems of Triassic, Permian, and Ordovician, were suggested as candidate storage reservoirs by this survey (He et al., 2010) in the formations of T_{1l}, P_{3s}, P_{2sh}, P_{1s}, and O_{2m}, respectively. Sandstone and mudstone were interbedded in the former four formations, which were the reservoir and the sealing cap, respectively, while in the fifth formation, O_{2m} dolomite and mudstone were the reservoir and the sealing cap.

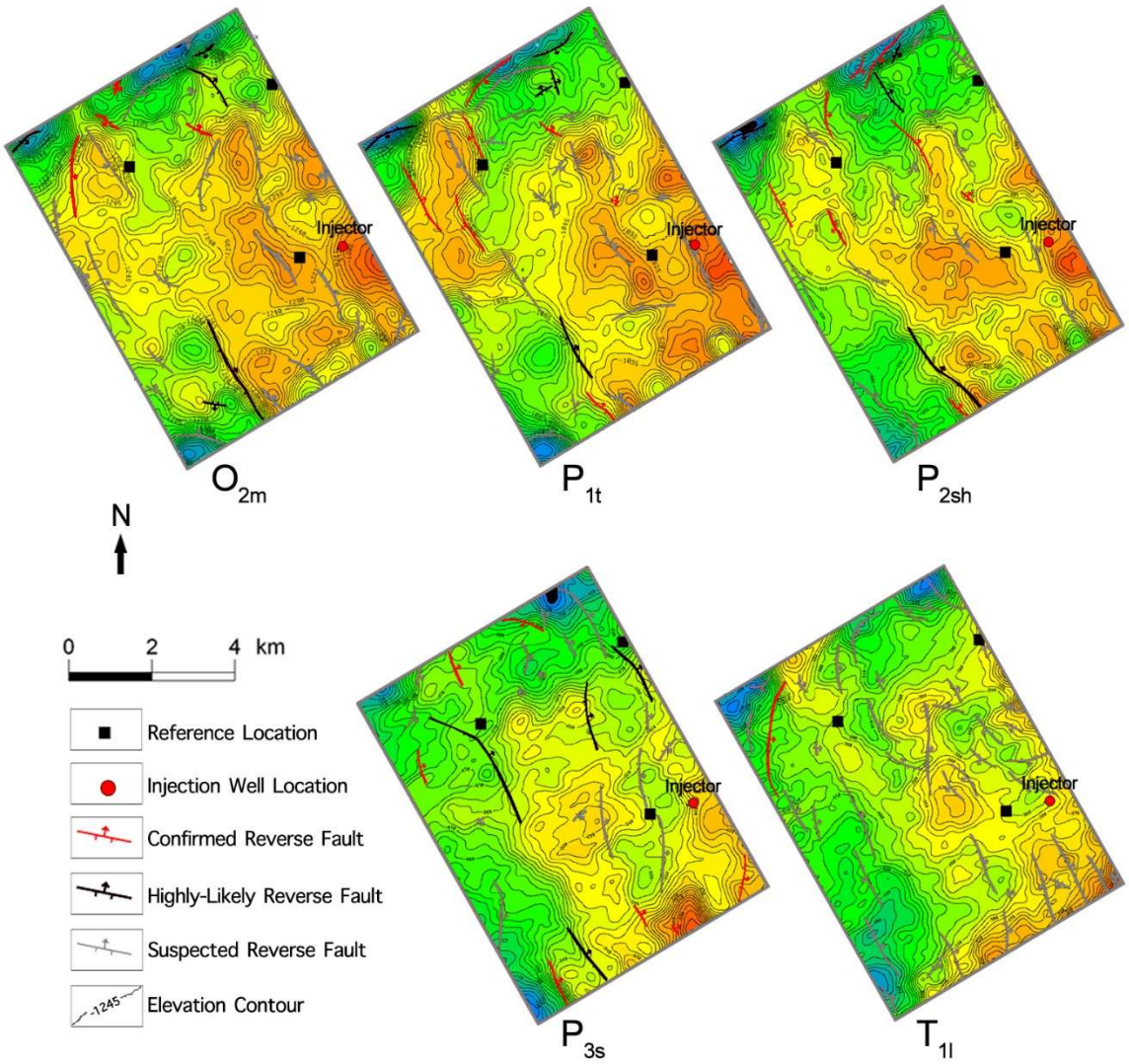

Figure 3-2 Tectonic structures of the formation bottoms reflected by the seismic survey (modified from He et al. (2010)).

Figure 3-3 presents isopach maps of sandstone in the lower section of the formations of P_{3s}, P_{2sh}, and P_{1s}, respectively, as well as estimated distributions of porosity and permeability in sandstone derived from an amplitude versus offset (AVO) analysis (He et al., 2010), which has been widely used to determine physical parameters (e.g., density), hydrogeological characteristics (e.g., porosity and permeability), and fluid content in rocks (e.g., water, oil, or gas) (He et al., 2010). Note, however, that He et al. (2010) only used data of rock elasticity, mud content, porosity and water saturation from other wells in the same region to derive the S-wave resistance log on which the AVO analysis was based.

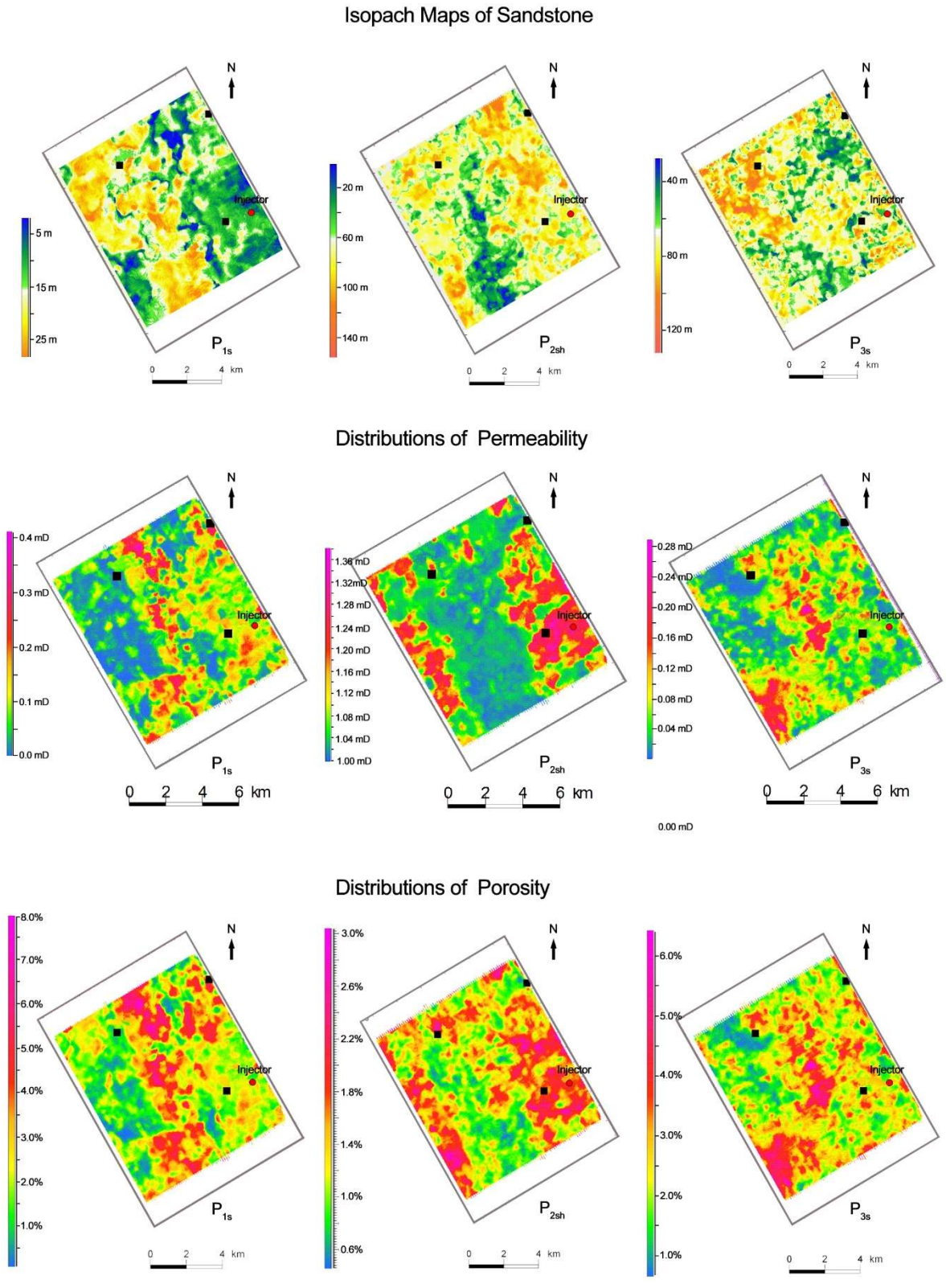

Figure 3-3 Isopach maps of sandstone and distributions of permeability and porosity of the sandstone in the lower section of the formations of P_{1s}, P_{2sh}, and P_{3s} (modified from He et al. (2010)).

Permeability and porosity in these formations were positively correlated, which means permeability increases with porosity. The resulting permeability and porosity were generally

below 10 mD (10^{-14} m^2) and 10%, respectively. Permeabilities of sandstone cores from T_{1l} and P_{1s} were measured to be 0.56 mD and 0.93 mD, respectively; porosities of these cores were 12.4% and 15.1%, respectively (Chang et al., 2013). Such low permeabilities and porosities indicate that the reservoir might not be a viable for geological CO_2 storage. On the other hand, mudstone thicknesses in the upper section of the formations of P_{2sh} range from 80 m to 180 m, and in P_{3s} are between 40 m and 120 m. Such huge thicknesses indicate a good sealing feature for storage (Figure 3-4).

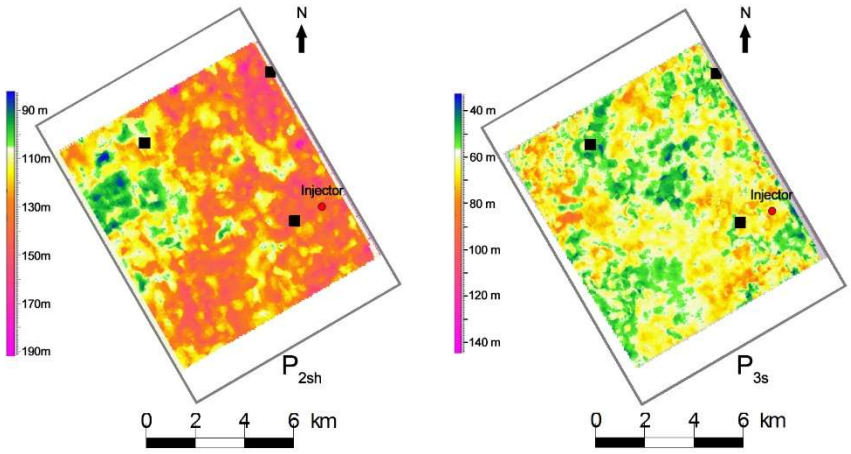

Figure 3-4 Isopach maps of mudstone in the upper section of the formations of P_{2sh} and P_{3s} (modified from He et al. (2010).

An exploration well was drilled to the depth of nearly 3000 m on the site in late 2010, and this provided more information about the strata (Figure 3-5). The injection depths were determined based on the aquifers identified from the well log (CNPC, 2010). A multi-layer injection strategy was employed to use all the aquifers. 21 intervals in the well were -perforated, from which CO_2 would enter the reservoir (Figure 3-5).

3.2.3 Hydraulic Fracturing

Hydraulic fracturing was operated at three depth ranges to fracture some of the injection layers (Figure 3-5) (CNPC, 2010; Meng, 2010). The total thickness of all the injection layers (sandstone) was 112.6 m. Mudstone in T_{1l} above the uppermost injection layer acted as the primary seal for CO_2 storage. All formations above T_{1l} acted as the secondary sealing structure for the whole project at regional scales. The exploration well was converted into the injection well later.

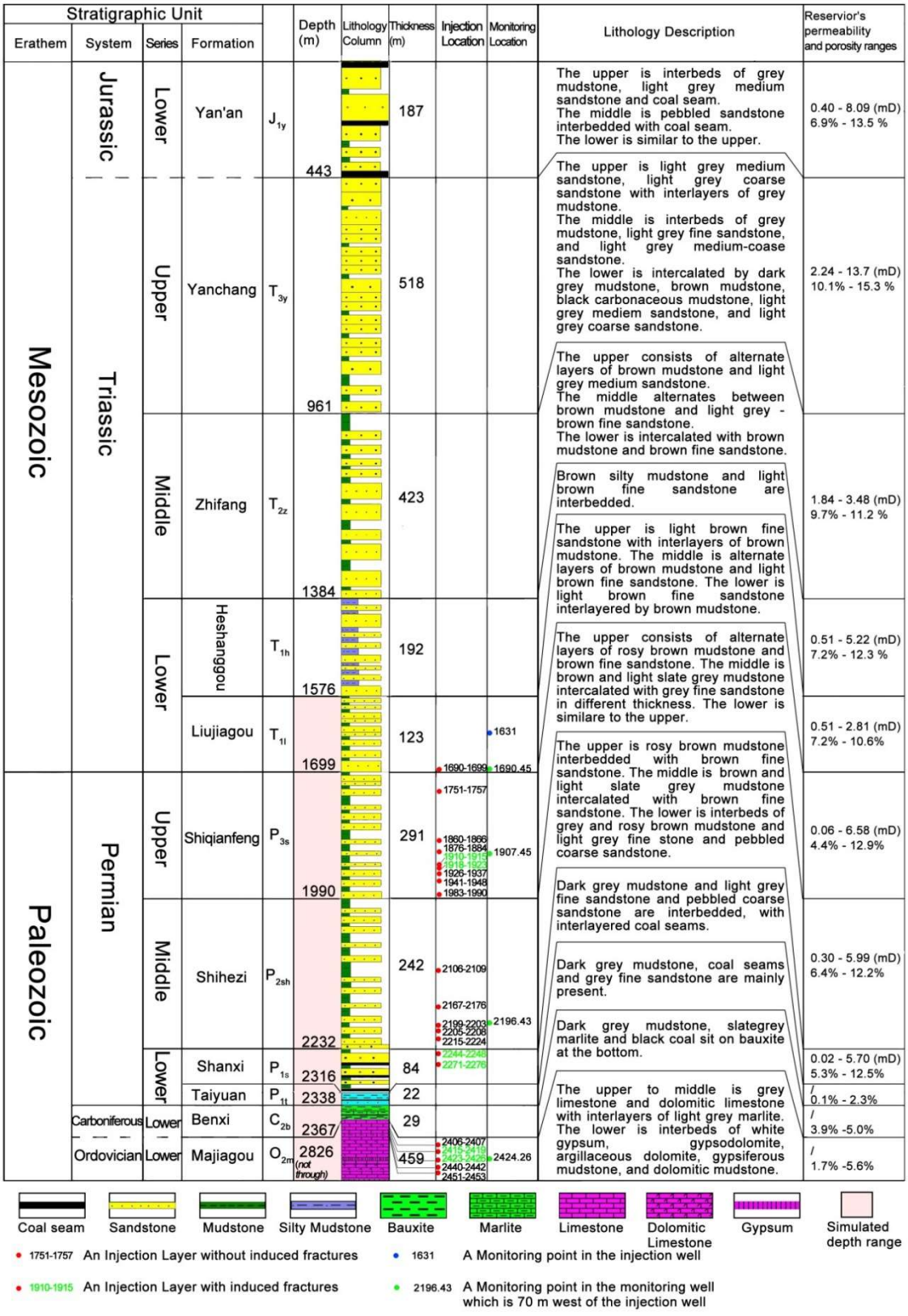

Figure 3-5 Lithological column of the exploration (injection) well from the Jurassic System downward.

Fracturing was conducted in three formations at depths between 1909.8 m and 1922.8 m in P_{3s}, between 2241.2 m and 2275.6 m in P_{1s}, and between 2415.0 m and 2426.4 m

in O_{2m} (Figure 3-5). According to the fracturing operation report (Meng, 2010), the induced fractures followed the direction of the principal in-situ stress at 80-85 degrees (clockwise from the north) and had a half-wing length of around 45 m and an opening width of about 5 cm. These fractures were filled with ceramic grains (proppant) of medium to heavy density, and had permeability between 100 mD and 1000 mD, and porosity between 20% and 30%, as estimated by Meng (2010).

3.3 Injection Operation

3.3.1 Injection Tests

An injection test was conducted once a year from May 2011 when the injections began. Each test included a 4-cycle operation normally lasting for 16 days, and each cycle consisted of a 48-hour injection followed by a 48-hour shut-in period (SPTEGI, 2011, 2012, 2013, 2014). Various injection pressures were applied at the wellhead in each test to establish a relationship between the injection pressure and the volume flux. During the injection hours, the temperature, pressure and flow rate into each storage layer were obtained by injection profile logging.

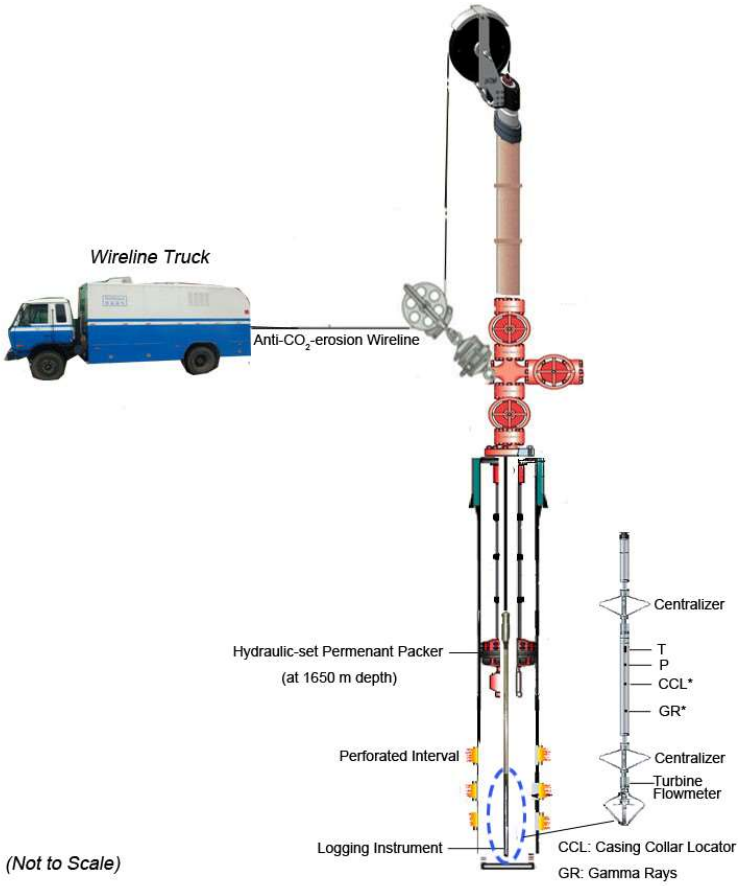

Figure 3-6 Schematic diagram of injection profile logging.

As shown in Figure 3-6, the injection profile logging was performed by lowering a logging instrument on the end of an anti-CO_2-erosion wireline into to the wellbore, and recording the needed properties, like T, P and volume flux, by using a variety of devices equipped in the instrument. For one injection cycle in this project, the flow profile and the P-T profile were logged separately. Firstly, the logging instrument was lowered to 1650 m depth (right below the packer), and then the installed flowmeter recorded the flow rate into each perforated layer as the instrument moved down through the wellbore to the depth of 2500 m. Then the instrument was pulled back to the starting place and began another trip at a different rate. After four trips with the rates at 10 m/min, 20 m/min, 30 m/min and 40 m/min, respectively, the flow profile logging was finished and the instrument was pulled out of the well and the data stored in the flowmeter were transferred to computer. Afterwards, the logging instrument was lowered in the injection well again for the P-T profile logging, but this time the starting place was the well bottom at 2500 m depth. As the instrument climbed up to the well head, the pressure and temperature at certain depths were recorded by the equipped pressure gauge and thermometer, respectively. Only one trip was made for the P-T profile logging. The recorded P-T data were also transferred to computer after the instrument was pull out of the well. Finally, after data processing, the complete injection profile including the flow allocation between the perforated layers and the P-T variations along the injection well in the test would be obtained.

Figure 3-7 shows that the volume flux and pressure had a linear relationship within each injection test. The injection initiation pressure in each injection test, defined as the minimum pressure at the wellhead needed to inject CO_2 into the reservoir, was calculated by letting the volume flux become equal to zero. The injection index was defined as the volume flux increase by every 1MPa pressure rise above the injection initiation pressure. The injection initiation pressure decreased by 27.5%, from 6.19 MPa in 2011 to 4.49 MPa in 2014. Meanwhile, the corresponding injection index increased by 7.35 times, from 4.06 m^3/hr/MPa to 33.92 m^3/hr/MPa. The pressure at well head and at bottomhole (PBH) during injection decreased year after year, while the corresponding injection rates in the tests increased or remained similar (Table 3-1). These data indicated that the overall injectivity of the reservoir increased over the years.

Only in the 2011 test did all 21 injection layers absorb CO_2 (mass ratio exceeds 0) and the number of layers that absorbed CO_2 decreased dramatically to below 10 from the 2012 injection test (Table 3-1). In fact, only four layers absorbed CO_2 throughout the four tests, at depths ranging from 1690 m to 1699 m, from 1751.4 m to 1756.8 m, from 1909.8 m to

1915.2 m, and from 2406.2 m to 2407 m, respectively. The mass ratio of the uppermost injection layer (from 1690 m to 1699 m) increased substantially from around 10% in 2011 to 68% in 2012, then to almost 80% in 2013, and eventually to about 90% in 2014. This layer showed a potential capacity to meet the target injection rate (3.17 kg/s) by itself.

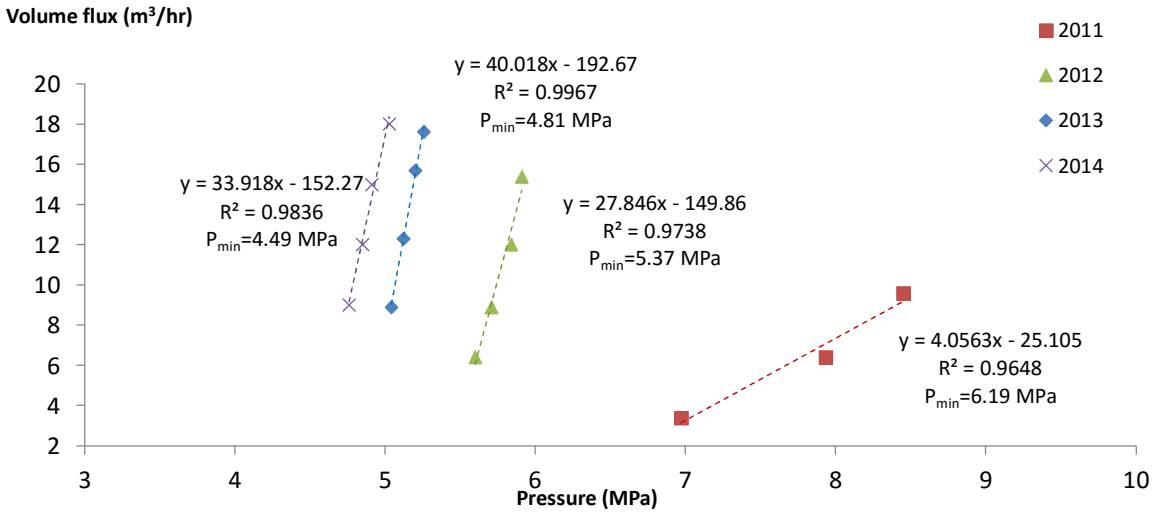

Figure 3-7 Pressure vs. volume flux at the well head in the injection tests from 2011 to 2014 (SPTEGI, 2011, 2012, 2013, 2014).

Table 3-1 Well head pressure (WHP), well head temperature (WHT), bottomhole pressure at 2500 m depth (BHP), volume flux, injection rate, and mass ratio in each injection layer in each cycle in the four injection tests (SPTEGI, 2011, 2012, 2013, 2014).

	2011				2012				2013				2014			
	1	2	3	4	1	2	3	4	1	2	3	4	1	2	3	4
WHP (MPa)	6.50	8.02	8.83	8.19	6.64*	7.02*	6.76*	6.89*	5.70*	6.06*	6.05*	6.24*	5.86*	5.93*	6.07*	6.11*
WHT (℃)	18.1	22.5	7.98	22.7	-2.2*	2.72*	-4.4*	-4.6*	1.00*	0.07*	-0.6*	-0.9*	0.84*	-1.9*	-1.3*	-2.7*
Volume flux (m^3/h)	3.4	6.4	9.6	12.8	6.4	8.9	12	15.4	8.9	12.3	15.7	17.6	9	12	15	18
CO_2 density** at well head (kg/m^3)	810	804	922	806	964*	939*	977*	979*	939*	948*	951*	955*	942*	958*	956*	964*
Injection rate*** (kg/s)	0.77	1.43	2.46	2.87	1.71	2.32	3.26	4.18	2.32	3.24	4.15	4.67	2.35	3.19	3.98	4.82
BHP (MPa)	26.88	29.43	30.56	30.28	27.22	27.53	27.68	27.87	26.56	26.95	27.04	27.16	26.37	26.71	26.87	26.98
Rate/PBH ($kg \cdot s^{-1} \cdot MPa^{-1}$)	0.028	0.049	0.080	0.095	0.063	0.084	0.118	0.150	0.087	0.120	0.153	0.172	0.089	0.120	0.148	0.179
Number of CO_2-absorbing layers	19	21	21	21	8	8	8	8	7	6	7	7	5	5	5	5

Mass ratio in depth range (%)																
	1690.0-1699.0 m	13.6	10.4	8.7	6.4	53.3	67.7	71.0	77.7	79.2	81.8	77.3	78.6	88.2	87.8	89.2	87.4
	1751.4-1756.8 m	8.5	13.6	15.5	57.2	11.8	2.5	8.1	4.6	4.6	3.3	6.1	5.4	3.5	5.1	4.4	4.5
	1860.4-1866.0 m	2.1	7.8	8.3	2.4	0.0	0.0	0.0	0.0	0.3	0.0	0.0	0.0	0.0	0.0	0.0	0.0
	1876.0-1883.6 m	8.4	11.3	11.1	5.8	0.0	0.0	0.0	0.0	0.0	0.0	0.0	0.0	0.0	0.0	0.0	0.0
	1909.8-1915.2 m (HF)	4.8	13.1	6.9	6.4	17.9	5.4	6.4	2.8	4.1	2.1	2.3	3.8	4.0	1.7	2.3	2.4
	1918.4-1922.8 m (HF)	17.9	0.6	14.1	1.6	0.0	0.0	0.0	0.0	3.6	5.4	5.4	3.8	0.0	0.0	0.0	0.0
	1926.2-1936.6 m	17.0	12.9	10.1	6.1	2.8	4.2	5.9	3.6	0.0	0.0	0.0	0.0	0.0	0.0	0.0	0.0
	1940.6-1947.8 m	1.5	0.6	5.1	0.5	2.0	6.0	4.3	2.8	0.0	0.0	0.0	0.0	0.0	0.0	0.0	0.0
	1982.8-1990.0 m	1.5	0.4	2.2	0.3	0.0	0.0	0.0	0.0	0.0	0.0	0.0	0.0	0.0	0.0	0.0	0.0
	2105.8-2109.0 m	1.5	1.6	1.9	0.8	0.0	0.0	0.0	0.0	0.0	0.0	0.0	0.0	0.0	0.0	0.0	0.0
	2167.0-2175.6 m	1.0	4.5	3.9	1.7	0.0	0.0	0.0	0.0	0.0	0.0	0.0	0.0	0.0	0.0	0.0	0.0
	2197.8-2203.4 m	0.3	0.0	0.3	2.5	0.0	0.0	0.0	0.0	0.0	0.0	0.0	0.0	0.0	0.0	0.0	0.0
	2204.6-2208.2 m	2.8	2.7	2.3	2.0	3.5	6.1	1.6	2.9	0.0	0.0	0.0	0.0	0.0	0.0	0.0	0.0
	2215.0-2223.6 m	2.5	1.7	1.8	0.4	0.0	0.0	0.0	0.0	5.0	4.0	5.9	3.6	0.0	0.0	0.0	0.0
	2243.6-2247.8 m (HF)	5.5	4.5	0.2	0.1	0.0	0.0	0.0	0.0	0.0	0.0	0.0	0.0	1.7	2.1	2.3	1.5
	2271.2-2275.6 m (HF)	1.0	1.5	2.1	1.4	4.0	3.9	1.1	2.8	0.0	3.4	0.0	0.0	0.0	0.0	0.0	0.0
	2406.2-2407.0 m	1.8	1.5	1.4	0.4	4.7	4.2	1.6	2.9	3.3	0.0	3.1	4.8	2.7	3.3	1.8	4.2
	2415.0-2419.0 m (HF)	2.3	0.2	0.9	0.9	0.0	0.0	0.0	0.0	0.0	0.0	0.0	0.0	0.0	0.0	0.0	0.0
	2423.4-2426.4 m (HF)	6.1	7.3	2.2	0.9	0.0	0.0	0.0	0.0	0.0	0.0	0.0	0.0	0.0	0.0	0.0	0.0
	2440.0-2442.4 m	0.0	2.7	0.2	1.2	0.0	0.0	0.0	0.0	0.0	0.0	0.0	0.0	0.0	0.0	0.0	0.0
	2451.0-2453.0 m	0.0	1.1	0.8	1.0	0.0	0.0	0.0	0.0	0.0	0.0	0.0	0.0	0.0	0.0	0.0	0.0

*: data were obtained at 100 m depth in the injection well. **: CO_2 density was calculated from the monitored pressure and temperature based on the Span-Wagner model (Span and Wagner,1996). ***: injection rate was computed by multiplying the calculated density and the volume flux. HF: hydraulically fractured.

3.3.2 Monitoring

Monitoring was conducted in the injection well and two nearby monitoring wells. The injection well was monitored for the injection process. Measurement was carried out at two points in the injection well: INJ1 at the wellhead for the pressure, temperature, volume flux and cumulative injected volume, and INJ2 at the depth of 1631 m for only pressure and temperature (Figure 3-8). Monitoring Well 1, 70 m west of the injection well, was used for continuous recording of the pressure and temperature response to the injection at four points of CH1 at the depth of 2424.26 m, CH2 at the depth of 2196.43 m, CH3 at the depth of 1907 m, and CH4 at the depth of 1690.45 m, respectively (Figure 3-8). Monitoring Well 2, 30 m

northwest of the injection well, was used for the vertical seismic profiling (VSP) test to estimate the extent of gas CO_2 plume in the reservoir, and for periodical groundwater sampling in the aquifers above the top sealing to detect possible leakage of CO_2 (Xie et al., 2015b).

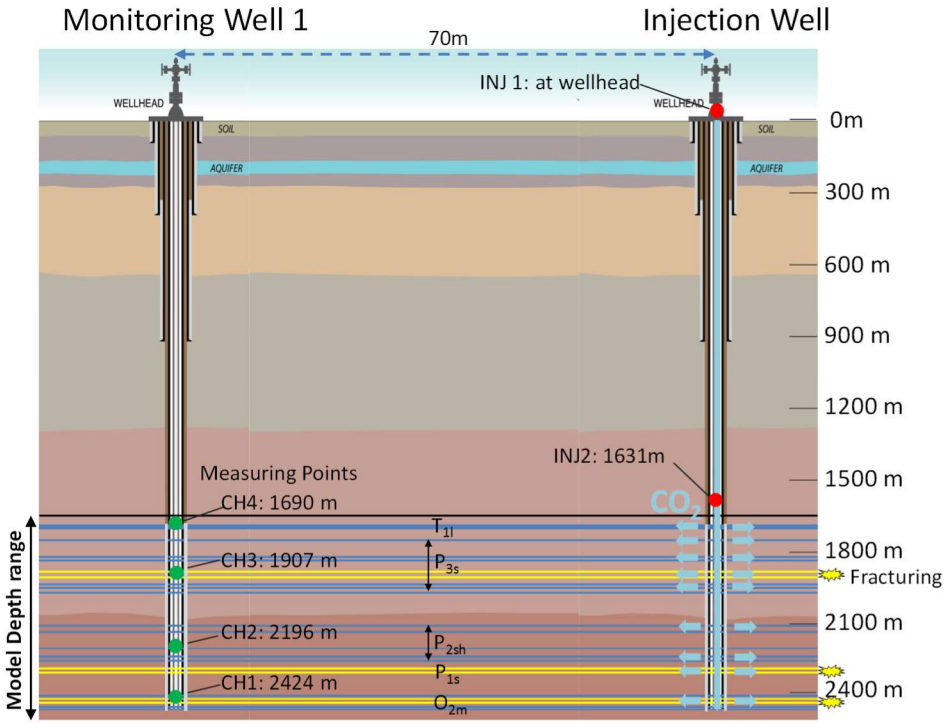

Figure 3-8 Schematic cross-section between Monitoring Well 1 and Injection Well.

Continuous measurement was conducted at six points: INJ1, INJ2 and CH1 to CH4. The reading frequency varied from every five seconds to every 30 seconds at these points, depending on the injection status. The original data were processed to daily average values in the research. Because the total injection mass rate was not directly measured, it was calculated from the volume flux and the concurrent CO_2 density at INJ1, the latter calculated from the pressure and temperature at INJ1 using the model developed by Span and Wagner (1996). The total injection mass rates over time were estimated from the data measured at INJ1, when available.

However, 30% of the records at INJ1 in the period from May 09, 2011 to Dec 18, 2013 were missing for unknown reasons (Figure 3-9), which resulted in a fragmented history of the total injection mass rate. Records at INJ2 were continuous in the same period, showing a complete history of pressure and temperature over 2.5 years. As the whole injection history was a prerequisite for the reservoir history-match simulation, it was necessary to fill in the gaps due to data loss based on all the data available. In addition to the history of the total injection

rate, the history of injection rate allocated to each injection layer, the history of cumulative injected mass, and the history of pressure distribution along the injection well, were reconstructed too. The process of reconstructing these histories is described in Subsections 3.4.1 to 3.4. 3.

Records at CH1, CH2, CH3 and CH4 were continuously recorded from the very beginning of the injection period to September of 2013; however, some of the records at CH1 and CH2 were out of the normal ranges, compared with the regional pressure coefficient and the geothermal gradient (Xiao et al., 2005; Yang et al., 2005) as shown in Figure 3-10 and Figure 3-11. The process of filtering these data at CH1 and CH2 is described in Subsection 3.4.4.

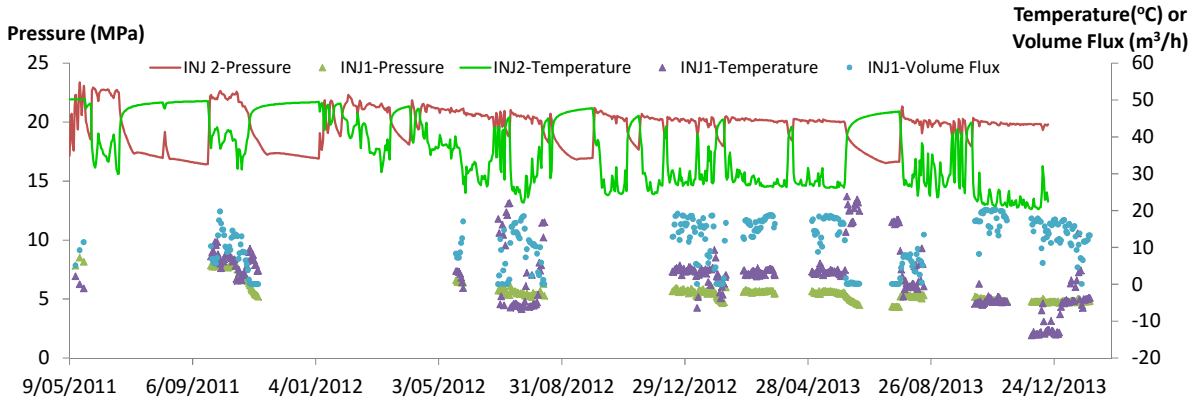

Figure 3-9 Raw injection data monitored at INJ1 and INJ2 in the injection well.

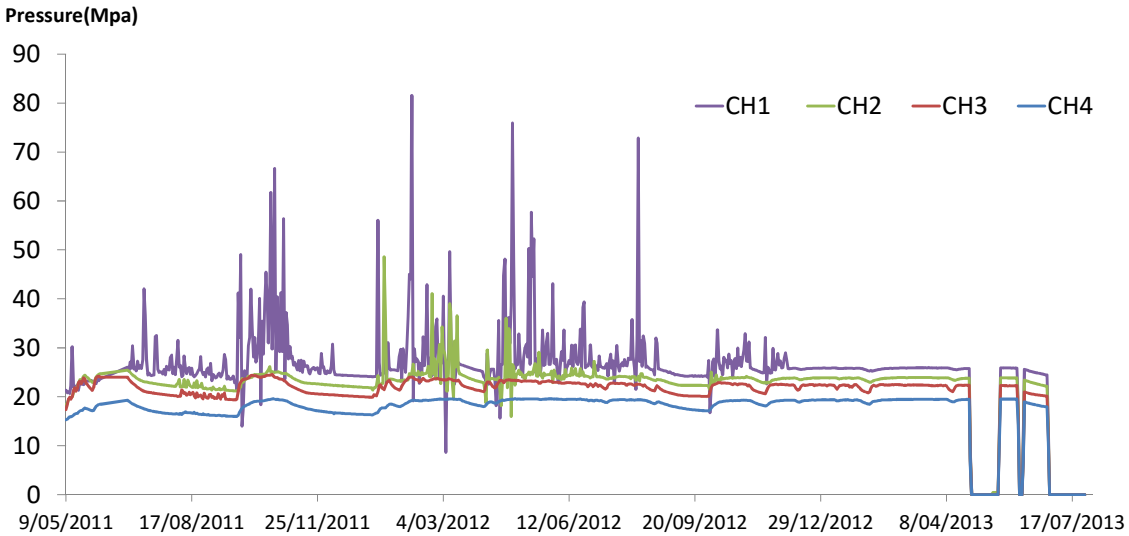

Figure 3-10 Raw monitored pressure at CH1 - CH4 in Monitoring Well 1.

Figure 3-11 Raw monitored temperature at CH1 - CH4 in Monitoring Well 1.

3.4 Data Processing

3.4.1 Reconstruction of Injection Pressure

Lack of volume flux data at INJ2 made it unsuitable for applying a wellbore flow model, e.g., Cronshaw and Bolling (1982), Lu and Connell (2008), Aunzo (2008), or Pan et al. (2011), to calculate the pressure distribution along the injection well depth. Through analysing the data at INJ1 and INJ2 on the dates when both points had data available (common dates), the pressure relationships between INJ1 and INJ2 were found to be dependent on the status of CO_2 flow (i.e., static or dynamic).

When the CO_2 flow was static (volume flux at INJ1 was zero or close to zero), the average CO_2 fluid density in the wellbore ($\overline{\rho_{co_2}}$, kg/m^3), was defined as:

$$\overline{\rho_{co_2}} = \frac{p_{INJ2} - p_{INJ1}}{(Z_{INJ2} - Z_{INJ1}) \cdot g} \quad \textbf{(Equation 3-1)}$$

where p_{INJ2} is the pressure at INJ2 (Pa), p_{INJ1} is the pressure at INJ1 (Pa), Z_{INJ2} is the depth of INJ2 (taken as positive, m), and Z_{INJ1} is the depth of INJ1 (= 0 m in this case), g is the gravitational acceleration (m/s^2), and $\overline{\rho_{co_2}} \cdot g$ is linear with the CO_2 density at INJ2 (kg/m^3) (Figure 3-12). So, the pressure along the injection well depth on those injection-suspended days was calculated as:

$$p_i = p_{INJ2} + \overline{\rho_{co_2}} \cdot g \cdot (Z_i - Z_{INJ2}) \quad \textbf{(Equation 3-2)}$$

where P_i is the pressure at point *i* in the injection well (Pa), Z_i is the depth of point i (taken as positive, m). Replace $\overline{\rho_{co_2}} \cdot g$ with the relationship with the density at INJ2 to get:

$$p_i = p_{INJ2} + (a \cdot \rho_{INJ2} + b) \times (Z_i - Z_{INJ2}) \quad \textbf{(Equation 3-3)}$$

where ρ_{INJ2} is the density of CO_2 at INJ2 (kg/m^3), which is determined by the pressure and temperature at INJ2, a is the coefficient (= 11.07111, m/s^2), and b is the constant (= -657.44582, Pa/m). Therefore, the pressure at Point i in the injection well on the shut-in days is only related to the pressure and temperature at INJ2. Thus, after the daily densities at INJ2 on the shut-in days during the whole monitoring period were calculated from the monitored pressures and temperatures at this point using the model by Span and Wagner (1996), pressures at other points in the injection well on the same days were obtained too.

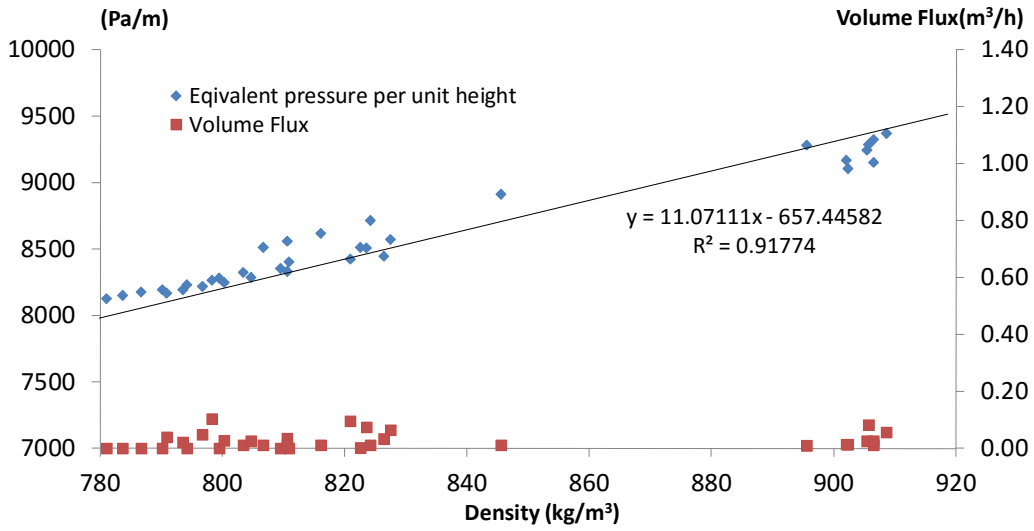

Figure 3-12 Relationship between $\overline{\rho_{co_2}} \cdot g$ and the density of CO_2 at INJ2 when injection was paused (based on data available at both INJ1 and INJ2).

In the injection tests, when the CO_2 flow was dynamic during the injection period, the pressure monitored at every 500 m down in the injection well showed a linear relationship with the depth (Figure 3-13). The slope was around 0.0080 MPa/m, which was independent from the volume flux; the intercept was various, but it was easy to be determined for an injection day by substituting the pressure at INJ2 on that day and the depth of INJ2 into the linear function. Thus, pressure at other depths in the injection well on the same day could be calculated.

Therefore, the whole history of pressure distribution along the injection well was obtained according to these two relationships, based on the status of CO_2 flow. The status of CO_2 flow was determined by the pressure at INJ2. The length of time between the start of a sharp rise and the start of a gradual decrease in pressure was considered to be an injection period, and the rest days were considered to be shut-in time (Figure 3-14).

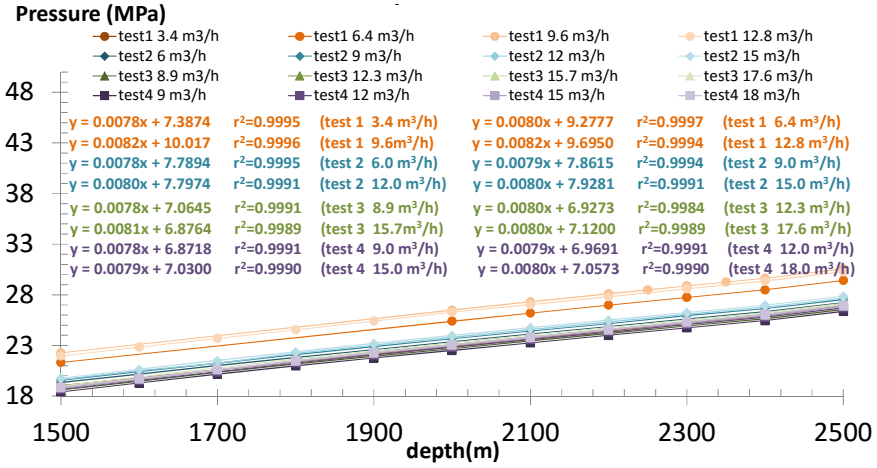

Figure 3-13 Relationship between pressure and depth in the injection well during injection in the injection tests.

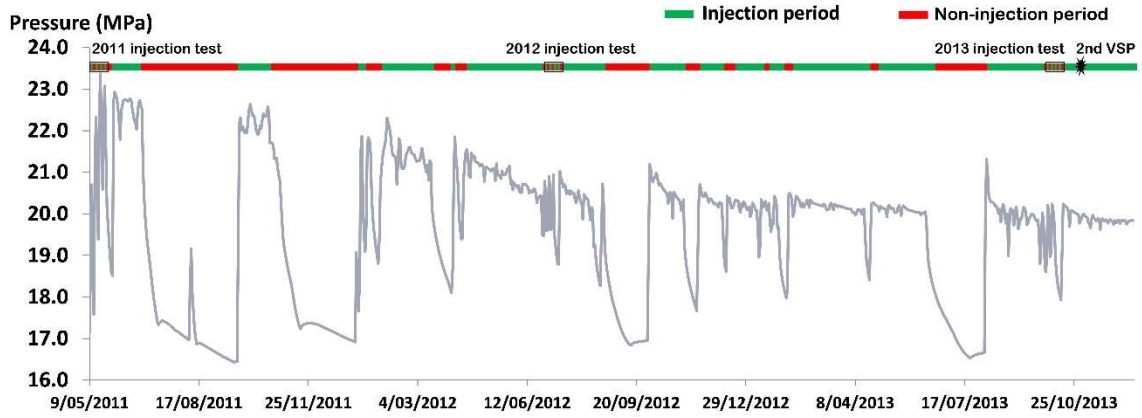

Figure 3-14 Injection periods and non-injection periods determined from the pressure data at INJ2, and the injection tests from 2011 to 2013.

3.4.2 Reconstruction of Cumulative Injected CO_2 Mass

The reconstruction of cumulative mass history consisted of four steps. Two assumptions were made: (1) the injection lasts 24 hours on an injection day; (2) when comparing with the cumulative mass recorded for a single date, the obtained error is systematic and time-independent.

The first step was to determine the relationship between the volume fluxes at INJ1 (F_{INJ1}, m^3/hr) and INJ2 (F_{INJ2}, m^3/hr) on the common dates. Because there were no perforated sections between INJ1 and INJ2 in the injection well, the mass rates ($q = \rho \cdot F$, where q is the mass rate, kg/hr, ρ is the density, kg/m^3, F is the volume flux, m^3/hr) at INJ1 and INJ2 were equal, i.e., $\rho_{INJ2} \cdot F_{INJ2} = \rho_{INJ1} \cdot F_{INJ1}$, so the volume flux at INJ2 was obtained by the equation from

densities at INJ1 and INJ2, determined by the monitored pressure and temperature. F_{INJ1} and the calculated F_{INJ2} were linearly correlated (Figure 3-15).

The second step was to reconstruct the volume flux at INJ1 on the remaining dates, according to the cumulative injected volume of CO_2 and the injection status (injection or shut-in). Note that the original cumulative injected volume data were calibrated to the very beginning of the injection time because they had been reset to zero a few times in 2011. Then, based on the injection status, the volume flux at INJ1 on a remaining date was estimated. If the remaining date was in a shut-in period, the volume flux was zero; if the remaining date was in an injection period, the volume flux was the average value of the nearest three to five measurements available.

The third step was to calculate the volume flux at INJ2 and the total injection rate. The volume flux at INJ2 on a remaining date was calculated according to the linear relationship obtained in the first step and the volume flux at INJ1, reconstructed in the second step. The total injection rate was then calculated by multiplying the volume flux at INJ2 and the CO_2 density at INJ2 on the same date.

The fourth step was to reconstruct the daily cumulative injected mass history based on the mass rates obtained in the third step, with the assumption about injection duration on an injection day, except on the dates of the injection tests.

Lastly, all the reconstructed cumulative masses were compensated by 1%, the difference from the official figure at a certain time point reported by Wu (2014), with the assumption about calibrating error .

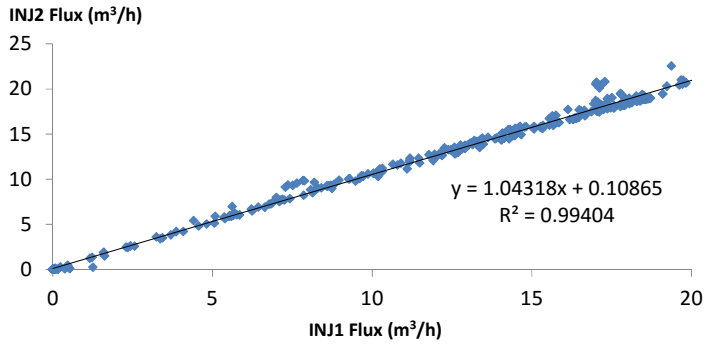

Figure 3-15 Correlation between F_{inj1} and F_{inj2}.

3.4.3 Reconstruction of Injection Rate Allocated to Each Injection Layer

It was difficult to determine the history of the injection rate into each injection layer because the data about mass allocation to each injection layer was very scarce. Each injection layer had only 12 entries about mass allocation from the injection tests in the 955 days from May 9, 2011 to December 18, 2013, during which the total injection rate was reconstructed

(Table 3-1). The mass allocation in the injection layers on other days had to be estimated. It was explicitly assumed that the mass ratio difference of an injection layer between two injection tests was linear to the injection days between the two tests. Then the mass rate of each injection layer on each day was calculated from its mass ratio and the correspondent total rate, which has been explained in 3.4.2.

3.4.4 Data Filtering for CH1 and CH2

Some data at CH1 and CH2 were far out of the normal range, so data filtering was conducted to reset these data. It was assumed that the data on the first date was within the normal range.

Daily relative pressure change (r) is defined as the pressure difference between two consecutive days divided by the pressure of the previous day; i.e.,

$$r_i = (P_i - P_{i-1}) / P_{i-1} \quad \textbf{(Equation 3-4)}$$

where P_i is the pressure on day i during the monitoring period and P_{i-1} is the pressure on day i-1.

So, both monitoring points (CH1 and CH2) had such a daily relative pressure change on each recorded date except on the first day. Whether an original pressure on a date ($P_{i\_original}$, i>1) was kept or not depended on the daily relative pressure change on that day (r_i, i>1) and the pressure on the previous day (P_{i-1}, i>1). The data at CH1 and CH2 were processed according to the following principle. Given a certain value θ and a small number t ($t < \theta/r_i$), if r_i>θ, then $r_{i\_new} = r_i * t$, and $P_{i\_new} = P_{i-1} * r_{i\_new}$. If $r_i <= \theta$ and P_{i-1} was not reset, $P_{i\_new} = P_{i\_original}$; if $r_i <= \theta$ and P_{i-1} had been reset to P_{i-1_new}, $P_{i\_new} = P_{i-1\_new} * r_i$. θ and t were determined through trial-and-error tests until the new curve not only represented the overall tendency in the original data, but also reserved the data within the normal range as much as possible.

Temperature resetting was made much easier because the data at CH3 and CH4 were mostly the same. Therefore, the isothermal process was assumed. The outranging temperature data at CH1 and CH2 were reset to the average value of the data that were in the normal ranges.

3.5 Summary

The reservoir of the project had a good sealing structure for CO_2 storage, but the permeability of the injection layers was not high. Hydraulic fracturing was carried out in three depth ranges, which involved six injection layers, to improve the injectivity. Injection tests that carried out annually from 2011 to 2014 showed a considerable increase in injectivity, but this increase was mainly contributed by an unfractured injection layer. With the aim to reconstruct

the injection histories of pressure and cumulative mass in the period from May 2011 to December 2013, the relationships between the pressure and the depth in the injection well, as well as between the injection volume flux and the injection pressure, were established by analyzing the available monitoring data.

CHAPTER 4 RESERVOIR DYNAMICS MODELING

4.1 Synopsis

This chapter provides details about how the reservoir of the SHCCS Project was modeled, including the approaches used to represent the injection well, the determination of key parameters of the model, the aspects considered to calibrate the model against the historical data, and the simulation scenarios designed during this research.

4.2 Simulation of Multiphase Flow in the Reservoir

The formations from T_{1l} to O_{2m} (Figure 3-5), consisting of sealing layers alternated with injection layers, were involved in the simulations. CO_2 movement in the reservoir may involve the processes associated with multiphase fluid flow, heat transfer, chemical reactions, and mechanical deformation of the reservoir; however, the multiphase fluid movement in the reservoir was mainly considered in this research. Other processes were not explicitly accounted for, either because of the time scales involved or the intensity of the processes. Heat transfer was not considered because temperature data at CH1, CH2, CH3 and CH4 showed no significant changes (Figure 3-11), so the thermal conditions of the reservoir were assumed to be constant in the simulations. Mechanical deformation of the reservoir was neglected too because no deformation was observed on the ground surface of the site since injection began. Chemical reactions, except for the equilibrium of water and CO_2 between different phases, were ignored in the simulation because the injection duration (less than three years) was too short for significant mineral trapping to take place.

The simulations in this research were run in TOUGH2-MP-ECO2N (Pruess, 2005; Pruess et al., 1999; Zhang et al., 2008), the massively parallel version of TOUGH2 with the fluid property module 'ECO2N', which describes the non-isothermal multiphase flow in the system H_2O-NaCl-CO_2. Fluids in ECO2N are presented in two phases: a water-rich phase (hereafter referred to as 'liquid'), and a CO_2-rich phase (hereafter referred to as 'gas'). The equilibrium phase partitioning water and CO_2 between the two phases in this module was modeled as a function of temperature, pressure and salinity, based on the correlations developed by Spycher and Pruess (2005). This module can model CO_2 disposal in a saline-

aquifer reservoir with temperatures from 12°C to 110°C, pressures up to 60 MPa, and salinity from zero to full saturation.

Two factors were critical in the simulation of this project. The first was about depicting the fractures created by hydraulic fracturing in the reservoir in the simulation. The other was about presenting the long injection well in the simulation.

Data about the hydraulic fractures provided by the operator company were very basic, with only simplistic information about the fracture dimensions and orientation available for simulation. No mechanical characteristics of the fractures and geo-mechanical data of this site were available when the research was conducted. Therefore, it was very difficult to handle the permeability of the fractures in a dynamic manner and taking into account the variation in the fracture permeability as a response to the change in the injection pressure. Thus, for the sake of simplicity, hydraulic fractures in the reservoir were treated as an equivalent porous medium, with high permeability and porosity estimated in the fracturing report (Meng, 2010).

Well representation in groundwater, geothermal, and oil reservoir simulations is conventionally done through a sink/source term approach, with flow rate distribution based on a mobility allocation method (Abou-Kassem et al., 2013). Although this approach works well for most well boundary simulations, it may result in physically incorrect solutions and poor numerical performance when backflow occurs in multi-layered wells within a thick, heterogeneous formation (Wu et al., 1996). The three approaches for injection-fluid allocation along a long-screened well are: ‘fixed pressure in the top screen’, ‘distributed pressure along the well’ and ‘injection from a virtual grid block’. These were proposed and the effectiveness between them was compared by applying them respectively to simulate the early stage for the SHCCS Project (Zhang et al., 2012).

Zhang et al. (2012) designed four scenarios to test these approaches. For the ‘fixed pressure in the top screen’ approach, constant injection pressure and rate were both tested as a first-type boundary condition on the top grid block of the well. The injection well was treated as an equivalent Darcy’s media (EDM), with a very high permeability. The distribution of CO_2 in injection layers was then determined by the pressure gradient and mobility of the layers in the model. For the ‘distributed pressure along the well’ approach, it was hypothesized that the injection pressure along the well was constant and 1.3 times the pressure at the same elevation generated from a hydrostatic pressure simulation. For the ‘injection from a virtual grid block’ approach, all the wellbore grid blocks were connected to a single virtual grid block, which also

maintained constant pressure in the simulation. The resulting CO_2 percentage and the gas saturation distribution in the injection layers among these approaches was compared, but the pressure response in the reservoir was disappointingly missed from the presented results.

An attempt was initially made in this research to use the 'fixed pressure in the top screen' approach by applying the continuous monitored pressure at INJ2 or the reconstructed injection rate on the top grid block of the injection well. Regardless, the EDM method for the injection well seemed inefficient in this research. High vertical permeability, shown either as 3.16×10^{-6} m^2, as advised by Hu et al. (2012), or as 10^{-8} m^2, indicated by Birkholzer et al. (2011), resulted in a very slow convergence in the well grid blocks, and CO_2 was only present in the top layer, rather than being distributed along the well length, as originally thought.

Therefore, the 'distributed pressure' approach was considered the best option because the distribution of pressure along the injection well length was obtained by data processing. This pressure distribution was time-dependent rather than constant, as indicated by Zhang et al. (2012). Theoretically, only pressure during the injection periods is necessary for this project, because the shut-in periods could be modeled as a hydrostatic condition. However, similar convergence problems were encountered when running the model as a hydrostatic condition for the shut-in periods. Consequently, in order to improve the simulation efficiency, the time-dependent pressure distribution along the well length was used as a fixed boundary condition to represent the injection well, in this research. In the sensitivity analysis, the injection well was also depicted as multiple sink/source terms, to evaluate the effects of boundary conditions at the injection well on the resulting reservoir performance.

4.3 Model Setup

4.3.1 Dimension and Mesh Discretization

A geological model was built by a third-party company with data obtained from the seismic survey, covering an area of nearly 96 km^2 (12 km × 8 km) and with a thickness of more than 1,000 m. Interfaces and thickness of the formations involved in the storage were determined from the interpretation of seismic data (He et al., 2010). Constructed using the spatial data obtained in the seismic survey, the geological model was composed of 43 layers from the top of T_{11} (around 1,550 m deep) to near the bottom of O_{2m} (around 2,700 m deep) with varying layer thicknesses from 21 m to 28 m, and 10,080 grid blocks (120 rows × 84 columns) in each layer, and measuring around 100 m × 100 m. Permeability and porosity of

each grid block in this geological model were interpolated to the grid blocks based on the distributions from AVO analysis.

Compared with the injection profile (Table 3-1) and the distance between the injection well and monitoring wells, the geological model needed to be remeshed for numerical simulation with a higher horizontal resolution around the injection well and a finer layering. Horizontally, within the 200 m radius from the injection well, the mesh was refined in a radical manner. Beyond this radius, the mesh was transformed to the rectangular mesh in the geological model (Figure 4-1). Vertically, layers from the 5th to 39th in the geological model were chosen for simulation and were refined. The thickness of these layers was adjusted to allow thickness of the injection layers in the simulation model to be identical to the injection profile (Table 4-1). Some original sealing layers in the geological model were combined into one to control the total number of layers. There were 52 layers in the simulation model, with depths starting at around 1,676 m and ending at 2,478 m (Table 4-1). One single hydraulically-fractured layer had one single fracture and all the fracture stretched out from the injection well along the principal stress direction with a half-wing length of 45 m (Figure 4-2). A subset of the geological model, with the side length of 1,020 m and centered at the injection well, was isolated and used in the dynamic model (Figure 4-1). The total number of the grid blocks for dynamic simulations was 95,094 (1761×52).

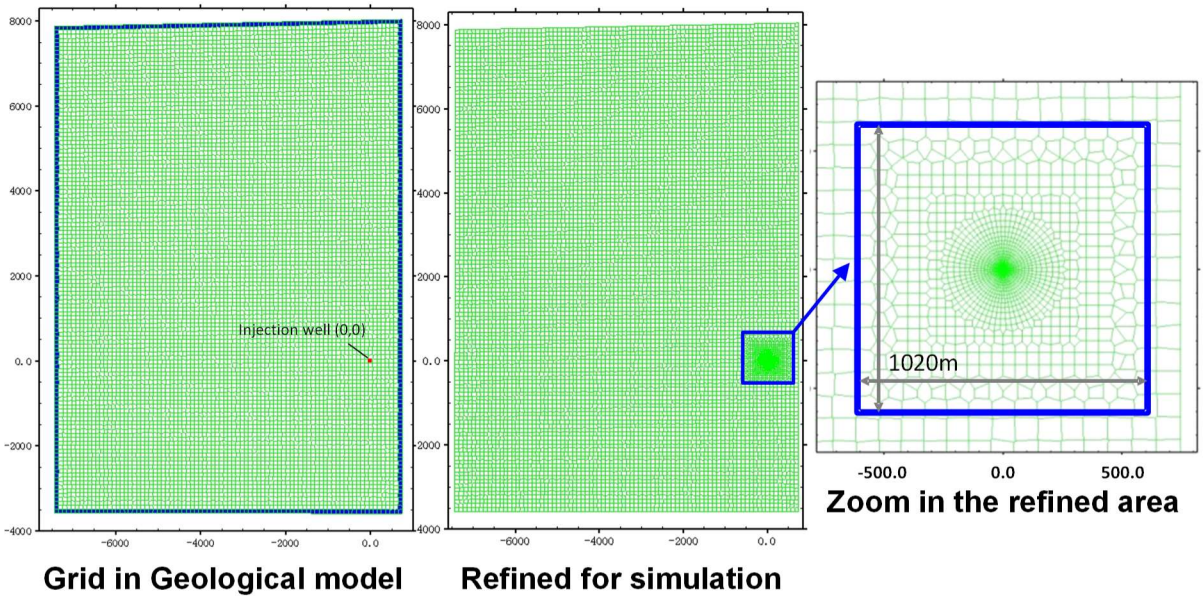

Figure 4-1 Grid in the geological model transformed for simulation.

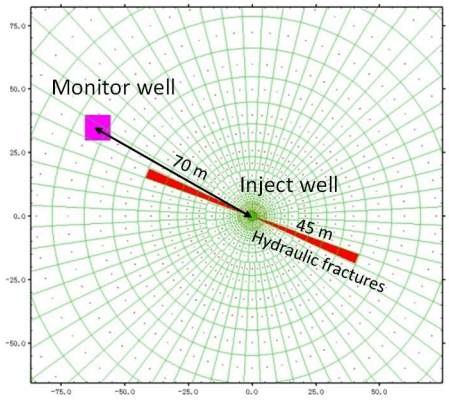

Figure 4-2 Configuration of the hydraulic fractures in the simulation model.

4.3.2 Permeability and Porosity Assignment

Permeability and porosity were interpolated into the new grid based on their distributions in the geological model. If a layer in the simulation model was involved two or more layers in the geological model, averaged values of permeability and porosity of these layers would be applied. Permeability and porosity distributions of the injection layers for simulation were shown in Figure 4-3.

The material in the grid blocks was parameterized by means of the absolute permeabilities in the X, Y, and Z directions, respectively, along with porosity, density, heat conductivity under fully liquid-saturated conditions, specific heat, as well as relative permeability and capillary pressure relationships. The permeabilities were isotropic and set to 1 mD (10^{-15} m^2), 10^{-5} mD (10^{-20} m^2), 10 D (10^{-11} m^2) and 100 mD (10^{-13} m^2) for the injection layers, the sealing layers, the injection well, and the fractures, respectively. Heterogeneous permeability in the reservoir was achieved in the simulation by assigning a permeability modifier number (PMOD) to each grid block (Pruess et al., 1999). The actual permeability of a grid block was the product of PMOD and its material permeability. Initial PMODs of the reservoir grid blocks were obtained by dividing their original permeability from the geological model by 10^{-15} m^2; PMODs of the injection well and the fractures were all assigned a value of 1.0. Porosity was directly assigned to each grid block after interpolation from the geological model; porosity of the fractures was set to 0.3, and porosity of the injection well was set to 0.99.

Table 4-1 Layering in part of the geological model and the simulation model, respectively.

Geological Model				Simulation Model	
No.	Bottom (m)	Relayered bottom (m)	Relayered thickness (m)	Thickness (m)	No.
4	1675.357300	1675.357300	/		
5	1702.580444	1690.000000	14.642700	14.64	1
		1699.000000	9.000000	9.00	2
		1702.580444	3.580444	30.80	3
6	1729.801392	1729.801392	27.220948		
7	1753.898071	1751.400000	21.598608	21.60	4
		1753.898071	2.498071	5.40	5
8	1777.991577	1756.800000	2.901929		
		1777.991577	21.191577	21.19	6
9	1802.087280	1802.087280	24.095703	72.29	7
10	1826.183472	1826.183472	24.096192		
11	1850.279175	1850.279175	24.095703		
12	1874.374390	1860.400000	10.120825	10.12	8
		1866.000000	5.600000	5.60	9
		1874.374390	8.374390	10.00	10
13	1898.470337	1876.000000	1.625610		
		1883.600000	7.600000	7.60	11
		1898.470337	14.870337	26.20	12
14	1922.564941	1909.800000	11.329663		
		1915.200000	5.400000	5.40	13 (HF)
		1918.400000	3.200000	3.20	14 (HF)
		1922.564941	4.164941	4.40	15 (HF)
15	1946.659668	1922.800000	0.235059		
		1926.200000	3.400000	3.40	16
		1936.600000	10.400000	10.40	17
		1940.600000	4.000000	4.00	18
		1946.659668	6.059668	7.20	19
16	1970.755981	1947.800000	1.140332		
		1970.755981	22.955981	35.00	20
17	1994.853271	1982.800000	12.044019		
		1990.000000	7.200000	7.20	21
		1994.853271	4.853271	26.73	22
18	2016.732300	2016.732300	21.879029		
19	2038.611450	2038.611450	21.879150	65.64	23
20	2060.491211	2060.491211	21.879761		
21	2082.371094	2082.371094	21.879883		
22	2104.251953	2104.251953	21.880859	23.43	24
23	2126.133057	2105.800000	1.548047		
		2109.000000	3.200000	3.20	25
		2126.133057	17.133057	17.13	26

Geological Model				Simulation Model	
No.	Bottom (m)	Relayered bottom (m)	Relayered thickness (m)	Thickness (m)	No.
24	2148.015625	2148.015625	21.882568	21.88	27
25	2169.896729	2167.000000	18.984375	18.98	28
		2169.896729	2.896729	8.60	29
26	2191.781006	2175.600000	5.703271		
		2191.781006	16.181006	22.20	30
27	2213.663330	2197.800000	6.018994		
		2203.400000	5.600000	5.60	31
		2204.600000	1.200000	1.20	32
		2208.200000	3.600000	3.60	33
		2213.663330	5.463330	6.80	34
28	2235.548584	2215.000000	1.336670		
		2223.600000	8.600000	8.60	35
		2235.548584	11.948584	20.00	36
29	2257.128174	2243.600000	8.051416		
		2247.800000	4.200000	4.20	37 (HF)
		2257.128174	9.328174	23.40	38 (HF)
30	2278.704834	2271.200000	14.071826		
		2275.600000	4.400000	4.40	39 (HF)
		2278.704834	3.104834	24.68	40
31	2300.281982	2300.281982	21.577148		
32	2321.859131	2321.859131	21.577149	87.27	41
33	2343.438232	2343.438232	21.579101		
34	2365.014893	2365.014893	21.576661		
35	2387.550781	2387.550781	22.535888		
36	2410.089600	2406.200000	18.649219	18.65	42
		2407.000000	0.800000	0.80	43
		2410.089600	3.089600	8.00	44
37	2432.629883	2415.000000	4.910400		
		2419.000000	4.000000	4.00	45 (HF)
		2423.400000	4.400000	4.40	46 (HF)
		2426.400000	3.000000	3.00	47 (HF)
		2432.629883	6.229883	13.60	48
38	2455.173096	2440.000000	7.370117		
		2442.400000	2.400000	2.40	49
		2451.000000	8.600000	8.60	50
		2453.000000	2.000000	2.00	51
		2455.173096	2.173096	24.72	52
39	2477.719482	2477.719482	22.546386		

*blue shade stands for the injection layer in the dynamic model.

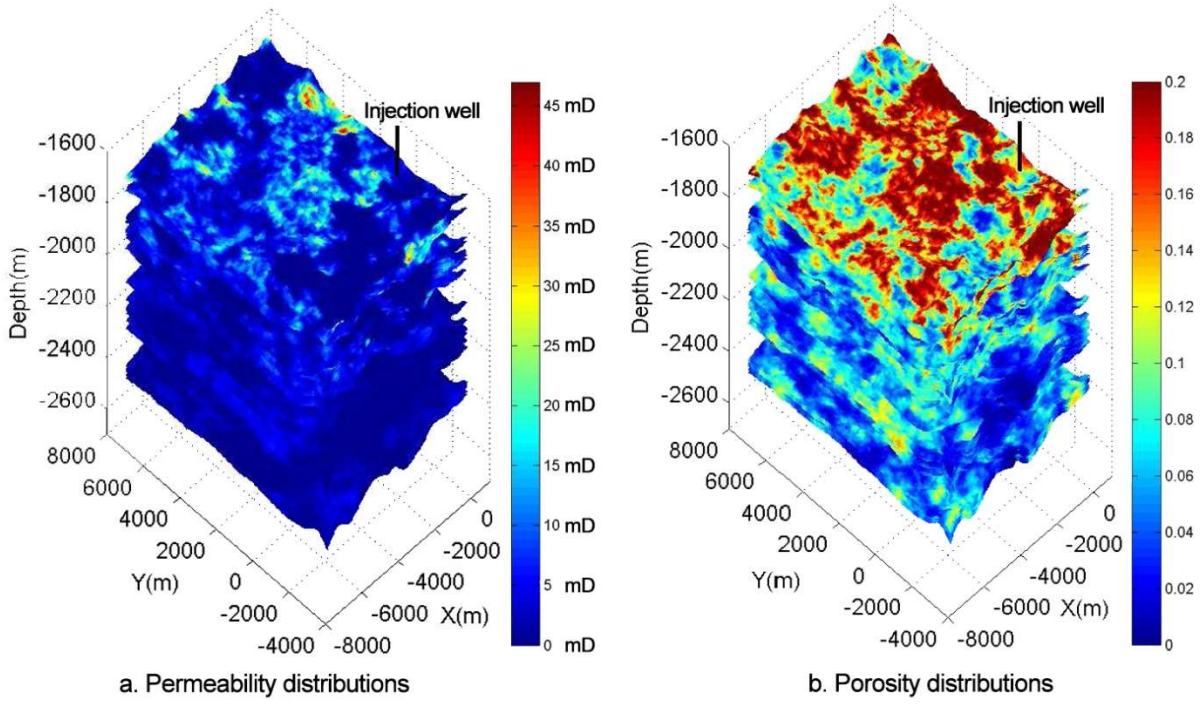

Figure 4-3 Distributions of permeability and porosity in the injection layers for simulation.

4.3.3 Initial Conditions

Based on the monitored data at CH1-CH4 prior to the injection, pressure and temperature in the reservoir were both linear with depth (Figure 4-4). Temperatures measured at the same depth in the injection well varied in the injection tests, but the average temperature was also found linear with depth (Figure 4-5). The initial temperature and pressure of a grid block were calculated using these relationships.

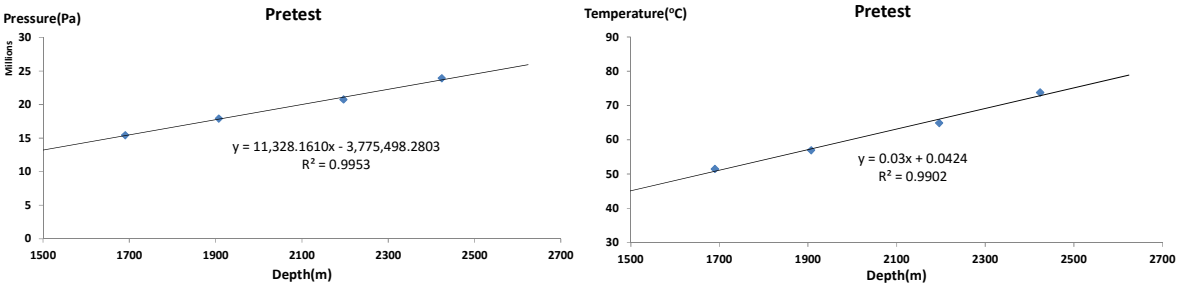

Figure 4-4 Relationships of pressure and temperature to depth, shown by monitored data at CH1-CH4.

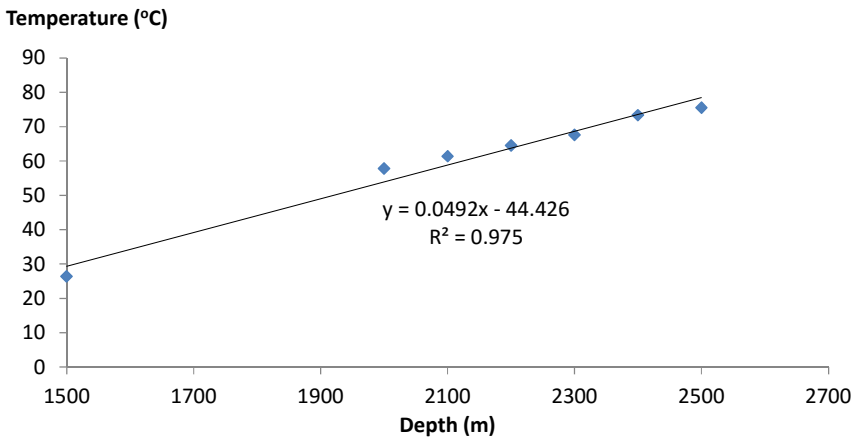

Figure 4-5 Relationship of temperature averaged over the injection tests to depth in the injection well.

The reservoir grid blocks were initialized with no CO_2 and saturated with saline water at 2% salinity (mass fraction). The injection well grid blocks were initialized with gas CO_2 at full saturation and with zero salinity. When the pressure boundary was used for the injection well, the initial conditions of the injection well were kept constant throughout the simulation; when the mass flux boundary was used, the conditions of pressure and CO_2 status in the injection well were allowed to change in the simulation.

4.3.4 Boundary Conditions

The lateral boundaries of the simulation model were set as Dirichlet boundaries, but done slightly differently from TOUGH2 by setting an extremely large volume (10^{50} m^3) to a lateral grid block. The volume of each lateral grid block in this research was increased by 120 times, to the order of 10^6 m^3 magnitude, equivalent to the volume of the remaining geological model. Given that the size of the model was around 100 km × 100 km, setting the lateral boundaries in this way would not cause the serious boundary effects that a closed boundary would, or have the same pressure results underestimated as would occur with a fixed-pressure boundary (Li et al., 2013). The effects of the three different boundary conditions on the simulation results are discussed in the sensitivity analysis in Chapter 6. The top and the bottom of the model were set as no-flow boundaries.

As stated earlier, two approaches for simulating the injection well (pressure boundary condition and mass rate boundary condition) were applied in this research. However, the use of the pressure boundary was preferred over that of the rate boundary, because the history of the pressure distribution along the injection well was reconstructed with higher certainty than

the history of the rate distribution. The reconstructed mass rate history was only used in the simulation for sensitivity analysis.

4.4 Other Key Parameters for Flow Simulation

The relative permeability to the liquid phase was calculated using the van Genuchten-Mualem method (Mualem, 1976; van Genuchten, 1980), expressed as Equation 4-7; and the relative permeability to the gas phase was calculated using the method by Corey (1954), written as Equation 4-8. Capillary pressure was calculated with the van Genuchten function (van Genuchten, 1980), written as Equation 4-9. S_{ls} (liquid-saturated saturation), S_{lr} (irreducible or residual liquid saturation), S_{gs} (gas saturated saturation), S_{gr} (irreducible or residual gas saturation) and exponent λ, were set to the same values for all materials, at 1.0, 0.05, 0.999, 0.05 and 0.457, respectively, including the fractures and the injection well (YLHYOIL, 2010). The entry capillary pressure for the layers ranged from 3.87 KPa to 100.01 KPa.

$$k_{rl} = \begin{cases} \sqrt{S^*}\left(1-\left(1-\left(S^*\right)^{1/\lambda}\right)^{\lambda}\right)^2, S_l < S_{ls} \\ 1, S_l \geq S_{ls} \end{cases} \quad (4\text{-}7)$$

here, $S^* = \left(S_l - S_{lr}\right)/\left(S_{ls} - S_{lr}\right)$;

$$k_{rg} = \begin{cases} 1-k_{rl}, S_{gr} = 0 \\ \left(1-\hat{S}\right)^2\left(1-\hat{S}^2\right), S_{gr} > 0 \end{cases} \quad (4\text{-}8)$$

here, $\hat{S} = \left(S_l - S_{lr}\right)/\left(1-S_{lr}-S_{gr}\right)$;

where k_{rl} is liquid relative permeability, k_{rg} is gas relative permeability, S_l is liquid saturation, S_{lr} is residual liquid saturation, S_{ls} is saturated liquid saturation, S_{gr} is residual gas saturation, λ is a parameter, usually as m in van Genuchten's notation. These equations are subject to the restriction $0 \leq k_{rl}, k_{rg} \leq 1$.

$$P_{cap} = -P_0\left(\left(S^*\right)^{-1/\lambda} - 1\right)^{1-\lambda} \quad (4\text{-}9)$$

where P_0 is capillary entry pressure. Equation 4-9 is subject to the restriction $-P_{\max} \le P_{cap} \le 0$. P_{max} was set to be 10^7 in the simulation.Pore compressibility for each layer was assigned in a range between 3.5×10^{-10} Pa^{-1} and 4.5×10^{-10} Pa^{-1}, decreasing with an increase in depth. The compressibility of fractures was assumed to be one order of magnitude larger, shown as 4.5×10^{-9} Pa^{-1}. Compressibility of the injection well was assumed to be zero.

4.5 Model Calibration

The model was calibrated against the monitored injected masses in the injection tests from 2011 to 2013 and the pressure response at the four points in Monitoring Well 1. Permeability was the major consideration during the calibration. Undoubtedly, porosity could influence the fluid movement in the simulation, but the permeability variation observed in the reservoir was much larger than the porosity variation (Lake and Jenson, 1991). Thus, permeability could have more significant effects on the fluid movement in the simulation. Simulations of existing projects were often calibrated by adjusting permeability of the reservoir (Shi et al., 2013; Doetsch et al., 2013; Senel et al., 2014; Kempka and Kühn, 2013; Paterson et al., 2013). Moreover, due to the complexity of the reservoir and variable individual injectivities of the injection layers, even if the sealing layers were not considered in calibration, there were still 21 permeability distributions (one distribution per injection layer) to be calibrated. If more parameters were taken into account for calibration, the likelihood that the optimal set of parameters was reliable would decrease.

It was assumed that all of the injection layers concurrently experience a change in capability of absorbing CO_2 at the start of an injection period between two injection tests, and this change is caused by the variation of permeability in the perforated layers. As the data from the injection tests indicated that the absorbing capability of each perforated layer dynamically changed over the years, permeability of each injection layer was modified entirely or partially in each time. The elements having no gas CO_2 ($S_{gs} < 0.01$) yet until the injection period assumed for absorbing-capability change, would have their PMOD adjusted. For each time of change, PMOD of these elements in the same layer were modified by the same factor, which was determined by the ratio of the monitored injected mass in this layer to the simulated injected mass during the injection test that the calibration was against.

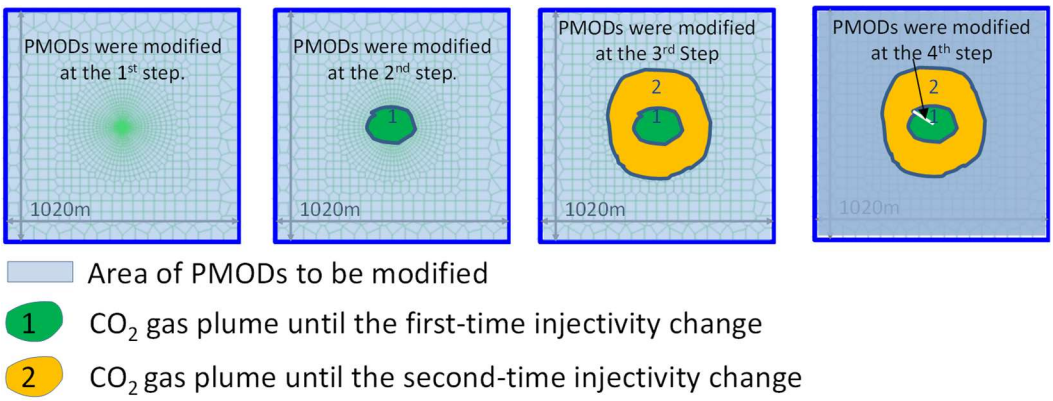

Figure 4-6 Schematic graph of the calibration process.

The calibration process included four steps, which were schematically illustrated in Figure 4-6. The first three steps were used to successively calibrate the injected masses measured in the injection tests from 2011 to 2013, and the last step was used to calibrate the pressure monitored at CH1 to CH4.

The first step was adjusting the permeability of all elements in the injection layers, except those for the injection well, to match the injected mass during the 2011 injection test. The calibration started with the model directly parameterized from the geologic model. The initial run of the model generated the simulated cumulative masses for certain durations, which included the injection tests from 2011 to 2013. By comparing the monitored and the simulated cumulative masses in each injection layer during the time of the 2011 test, a set of ratios (the monitored mass/simulated mass), $R1 = \{r_1, r_2, r_3, ..., r_{21}\}$, were obtained. Then PMOD of the elements in an injection layer were multiplied by the layer's ratio in R1. The model with the new PMODs was run again, which provided a new set of ratios. The process was repeated until the resulting ratio of each injection layer was between 0.90 and 1.10.

The second step was to calibrate against the 2012 injection test data, in which PMODs of the injection layer were partially modified. Since the last simulation run from the first step resulted in the simulated mass during the 2012 injection test, a set of ratios (R2) for the second injection test was obtained in the same way. For those layers became inactive (mass ratio = 0) in the 2012 test, their ratio was reset to 0.001 to prevent permeability from being 0 in the later simulations. If an injection period between the 2011 and 2012 tests was assumed to be the time for absorbing capability change, the permeability of the elements having no gas CO_2 until this change would be multiplied by the layer's ratio in R2. Then model with further-modified PMODs was run again and resulted in a new R2. The process was repeated for a few times until the absorbing layers in the 2012 test had their ratio in R2 in the range of 0.90 to 1.10. The

injection periods between the 2011 and 2012 tests was tested one after another, in order to have the simulated cumulative masses over the entire simulation time most close to the historical data .

Likewise, the third step was to calibrate against the mass data in the 2013 injection test. Because the injection pressure data in 2014 was lacked, the model was not calibrated against the 2014 injection test.

The last step was to calibrate against the pressure measured at CH1 to CH4. The monitored pressure in the monitoring well in the injection tests showed a good hydraulic connection between the two wells. Therefore, the elements that connected the two wells in the four pressure-monitored layers were given an identical, high layer-dependent value of PMOD.

4.6 Modeling Scenarios

Thirteen scenarios were simulated in the research (Table 4-2).

Scenario 1 was used for calibration, where the injection well was approached as a pressure history condition, and permeabilities of the injection layers were calibrated against the 2.5 year's cumulative injected CO_2 mass history, the mass ratios of the four layers that absorbed CO_2 throughout the injection tests and the pressure histories at CH1, CH2, CH3 and CH4. The area of the CO_2 gas plume in the uppermost injection layer in this scenario, was compared with the one estimated by the VSP survey.

Scenario 2 was used to evaluate the role of the induced fractures for improvement of injectivity, where no induced fractures were assumed. The results of the cumulative injected CO_2 masses and mass ratios of the four injection layers absorbing the most CO_2 were compared with Scenario 1.

Scenario 3 was set with the aim of assessing the effects of permeability distribution characteristics (homogenous or heterogeneous) on reservoir performance. Permeabilities of an injection layer in this scenario were all assigned the average value of the permeability in that layer in the geological model, so it was layer-wise homogeneous.

Scenario 4 was set to examine the effects of the injection procedure on reservoir performance, where the injection was hypothesized to be continuous through the simulation time.

Table 4-2 Summary of the simulation scenarios.

Scenario	Initial Conditions	Boundary for Injection	Lateral Boundary Condition	PMODs	Simulation Time	Purpose
1	Pre-injection	Reconstructed pressure history	Volume of the involved elements is enlarged by 120	Calibrated Heterogeneous	955 days (2011/05/09/ – 2013/12/18)	History match
2	Same as Scenario 1	Same as Scenario 1	Same as Scenario 1	Calibrated Heterogeneous, but with no induced fractures	Same as Scenario 1	Evaluate influence of the induced fractures
3	Same as Scenario 1	Same as Scenario 1	Same as Scenario 1	Homogeneous	Same as Scenario 1	Assess impacts of heterogeneous permeability on reservoir performance
4	Same as Scenario 1	Hypothesized pressure boundary for continuous injection	Same as Scenario 1	Same as Scenario 1	Same as Scenario 1	Assess impacts of injection procedure on pressure build-up
5	Same as Scenario 1	Same as Scenario 1	Same as Scenario 1	Same as Scenario 1	Same as Scenario 1	Examine impacts of hysteresis effects on reservoir performance
6	Results from Scenario 1	Twice Repetition of pressure from 2012/12/19 to 2013/12/18	Same as Scenario 1	Same as Scenario 1	730 days (2013/19/12/ – 2015/12/18/)	Predict reservoir's future performance
7	Same as Scenario 1	Reconstructed mass rate history	Same as Scenario 1	Same as Scenario 1	Same as Scenario 1	Sensitivity analysis – injection boundary
8	Same as Scenario 1	Same as Scenario 1	Volume of the involved elements is not enlarged	Same as Scenario 1	Same as Scenario 1	Sensitivity analysis – closed lateral boundary
9	Same as Scenario 1	Same as Scenario 1	Volume of the involved elements is enlarged to 10^{51} m^3	Same as Scenario 1	Same as Scenario 1	Sensitivity analysis – constant pressure lateral boundary
10	Same as Scenario 1	Same as Scenario 1	Same as Scenario 1	Same as Scenario 1	Same as Scenario 1	Sensitivity analysis – rock compressibility is one order of magnitude larger
11	Same as Scenario 1	Same as Scenario 1	Same as Scenario 1	Same as Scenario 1	Same as Scenario 1	Sensitivity analysis – rock compressibility is 0
12	Same as Scenario 1	Same as Scenario 1	Same as Scenario 1	Same as Scenario 1	Same as Scenario 1	Sensitivity analysis – S_{lr} = 0.20, S_{gr} = 0.0, entry capillary pressure 20% lower
13	Same as Scenario 1	Same as Scenario 1	Same as Scenario 1	Same as Scenario 1	Same as Scenario 1	Sensitivity analysis – *Slr* = 0.30, S*gr* = 0.10, entry capillary pressure 20% higher

Scenario 5 was set to see how hysteresis effects would affect the performance in the same intermittent injection procedure, but only in the four layers that absorbed CO_2 during all the injection tests (CO_2 mass ratio was not zero), though all the injection tests were assumed to be affected by hysteresis effects.

Scenario 6 was set to predict the future reservoir performance, where the initial condition was the resulting status at the end of the simulation in Scenario 1 and the injection

procedure was assumed to repeat the section between Dec 2012 and Dec 2013 for two more years.

Scenarios 7 to 13 were for the sensitivity analysis. Scenario 7 was used to look at how the injection well was approached in the simulation would affect the results, where the reconstructed mass rate history was used. Scenarios 8 and 9 were used to see how different lateral boundary conditions would influence the simulation results. Scenarios 10 and 11 were set to evaluate the influence of rock compressibility on the simulation results. Scenarios 12 and 13 were used to examine the impacts of different S_{lr}, S_{gr} and entry capillary pressure on the simulation results.

4.7 Summary

The dynamic model for simulating the CO_2 storage process in the saline aquifers was built on the geological model, which was parametrized from the seismic survey results. Thirteen scenarios were designed to investigate the reasons behind the observed reservoir behavior, and evaluate the sensitivity of the model.

CHAPTER 5 RESULTS –DATA ANALYSIS

5.1 Synopsis

This chapter presents the results of the reservoir performance analysis based on the experimental data. These results included injectivity variation of the injection layers over the years, the injection histories including pressure, cumulative injected mass, and injection rate, pressure at the four points in Monitoring Well 1, and the gas plume suggested by the VSP surveys. Some of the results will be compared with the simulation results in Chapter 6.

5.2 Injectivity of the Reservoir

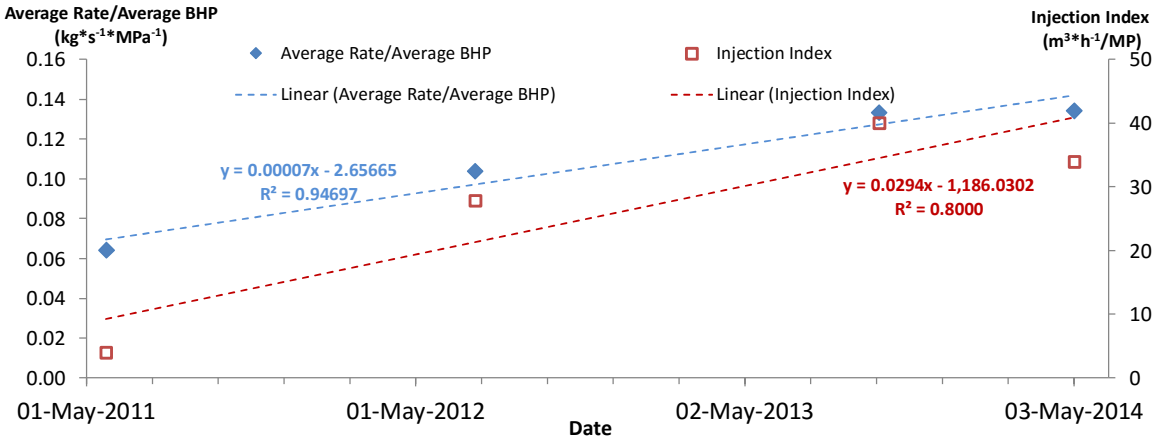

Figure 5-1 Ratios of average rate to average BHP and injection indices in the injection tests.

The ratio of average rate to average bottomhole pressure (BHP) in the injection test steadily over the years between 2011 and 2014, and the injection index increased over the same period of time. When correlated over the time, they both showed a linear relationship (Figure 5-1). The increase in both the ratio of average rate to average BHP and the injection index indicated that it became increasingly easier to inject CO_2 into the reservoir, meaning the injectivity was growing. Likewise, the average injection rate increased with the decrease of the number of the injection layers absorbing CO_2 (Table 5-1). Furthermore, the growth in the average injectivity over the injection periods in each year from 2011 to 2013 was also indicated by the reconstructed histories about the injection pressure and the total injection rate (Table 5-2). Such performance has rarely been observed in the practice of CO_2 storage in saline aquifers.

As mentioned earlier in Chapter 3, not all the injection layers absorbed CO_2 in the four injection tests. Many injection layers, including most of those being hydraulically fractured, stopped absorbing CO_2 from the 2012 injection test. A few among these that stopped absorbing CO_2 in the 2012 injection test restarted absorbing CO_2 in the 2013 or 2014 tests, but with a ratio of below 1%. Only four of the 21 layers kept absorbing CO_2 during all the tests, at depths of 1690 m to 1699 m, 1751 m to 1757 m, 1910 m to 1915 m, and 2406 m to 2407 m.

Table 5-1 Key information on the four injection tests from 2011 to 2014.

Year	Injection Initiation Pressure (MPa)	Injection Index (m^3/hr/MPa)	Average Injection Rate (kg/s)	Number of Layers Absorbing CO_2	Average Mass Ratio in the Uppermost Injection Layer (%)
2011	6.189	4.056	1.7657	21	9.75
2012	5.382	27.846	2.6835	8	67.42
2013	4.815	40.018	3.6218	7	79.21
2014	4.490	33.920	3.5878	5	88.14

Table 5-2 Average BHP over the injection periods in each year from 2011 to 2013 and the corresponding average injection rate and the ratio of the rate to the pressure.

Year	2011	2012	2013
Average BHP over the injection periods (MPa)	30.04	28.61	28.08
Average rate over the injection periods (kg/s)	3.08	2.97	3.10
Ratio of the rate to the pressure ($kg*s^{-1}*MPa^{-1}$)	0.103	0.104	0.111

Figure 5-2 displays the average mass ratios of these layers in the four tests, respectively, and also the sum of the ratios of these four layers in each test. The total mass ratios of these four layers indicated that they became the major absorbing layers from the 2012 injection test. To look at these layers individually, the two layers, from depths of 1690 m to 1699 m and 2406 m to 2407 m, experienced a mass ratio growth over the years. Mass ratio of the uppermost layer (from depths of 1690 m to 1699 m) increased substantially after the 2011 injection test: it rocketed from around 10% to 67% in the 2012 injection test, increased continuously in the later tests, and eventually reached up to about 90%. However, the other two layers, at depths of 1751 m to 1757 m and 1910 m to 1915 m, had an decline. The biggest drop in mass ratio of the layer with depths of 1751 m to 1757 m was seen between the tests of 2011 and 2012, from 23.6% to 6.7%. Despite the layer with depths of 1910 m to 1915 m having been hydraulically fractured with the purpose of increasing injectivity, its mass ratio dropped from 8.1% in the 2012 test to 3.1% in the 2013 test.

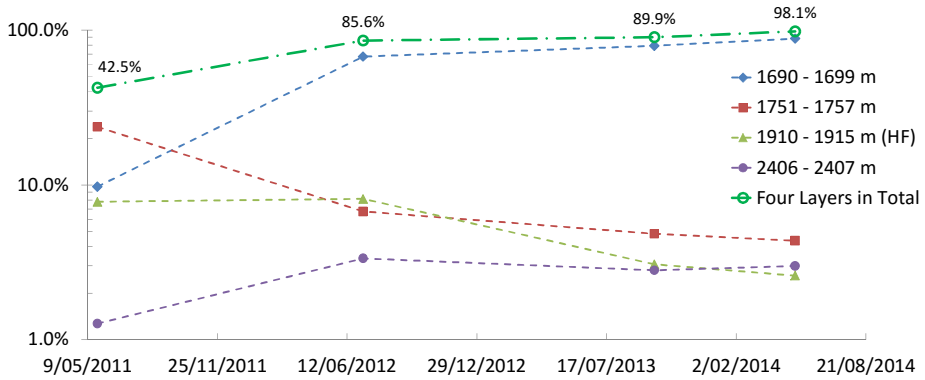

Figure 5-2 Mass ratios of the major layers and their total mass ratios over the injection tests.

To consider the contribution of all the hydraulically-fractured layers, the total mass ratios of the layers showed a similar tendency as the layer with depths of 1910 m to1915 m (Figure 5-3). Some fracture layers became incapable of absorbing CO_2 after the 2011 injection test. Only the uppermost fractured one (with depths of 1751 m to 1757 m) kept absorbent through the tests. Therefore, the mass ratio of these fractured layers was seen to have a big jump from 26% in the 2011 test to 11% in the 2012 test, and further declined to about 5% in the 2014 test. These data indicate that the induced fractures may only help to increase injectivity at the early stage of injection.

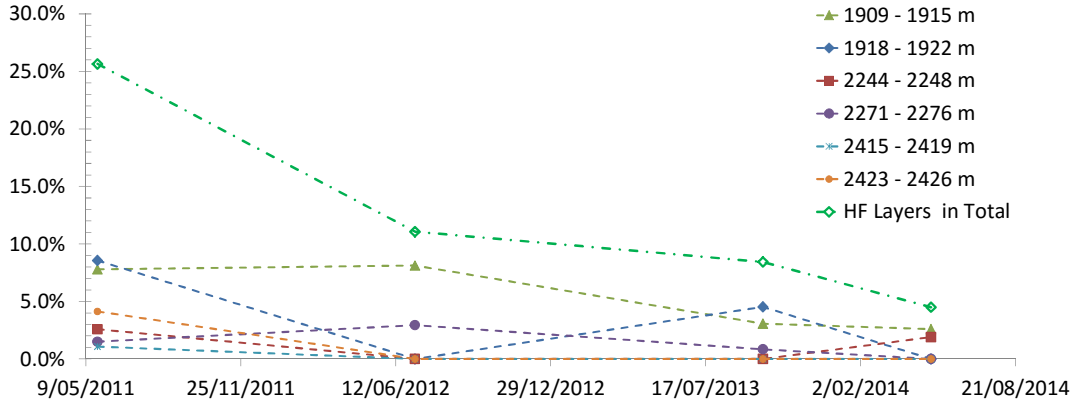

Figure 5-3 Mass ratios of the hydraulically-fractured layers and their total mass ratios over the injection tests.

The reason why some layers stopped absorbing CO_2 after the 2011 injection test may be connected with the permeability change due to the lithological variation in these layers. The area around the injection well may be higher permeable than other places in the same layer because this area was more disturbed by the well construction, and may have higher percentage of sandstone. For such a thick formation sequence used for CO_2 injection, another factor may relate to the decreasing pressure condition and the competition of permeability in the upper layers. When bottomhole pressure decreased, the column height of the injected CO_2 in the injection well may become smaller. Thus, the injected CO_2 may not reach to the bottom layers,

but just focusing on the upper layers. Therefore, when the injection pressure became lower in the later injection tests (Figure 3-7), it may not be high enough to drive CO_2 into lower layers with much less permeability.

In summary, although the injection layers that absorbed CO_2 became much fewer, the overall injectivity of the reservoir increased considerably over the years (Table 5-1, Table 5-2). The hydraulic fractures could only be effective in the early injection period to improve the injectivity of fractured layers. In this project, hydraulic fractures seemed to have no relation to the overall injectivity growth over the years.

5.3 Reconstructed Injection Histories

The pressure distribution along the injection well was obtained according to the relationships established in Chapter 3. Figure 5-4 shows the pressure histories at some depths in the injection well. Please note that, as the CO_2 density was assumed to be linear with depth (see Equation 3-2), the reconstructed pressure may deviate more with time from actual one at deeper formation.

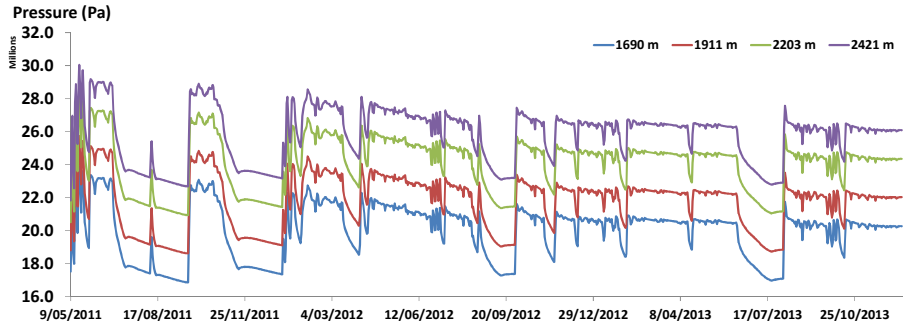

Figure 5-4 Reconstructed pressure histories at selected depths in the injection well.

Figure 5-5 shows the reconstructed cumulative injected CO_2 mass over the period during which INJ2 data were available. The reconstructed mass history is believed to be reasonable, compared to the numbers at two specific time points reported in two publications about the project. By March in 2013, the reconstructed cumulative mass was 105,000 tons, 12.5% less than the total injected mass reported by Jiang et al. (2014), which was over 120,000 tons. At the end of October in 2013, the reconstructed cumulative mass was 152,400 tons, 1% less than the 154,000 tons reported officially by the project owner (Wu, 2014). However, the number by Jiang et al. (2014) could have been overestimated because their figure suggested that the average injection rate from March 2013 to October 2013 was 2.62 kg/s, merely 83% of the target rate (3.17 kg/s), which is less than the official statement by Wu (2014) that the injection rate had reached or exceeded the target rate since the end of 2011. The average

injection rate based on the reconstructed data during the same period was 3.78 kg/s, consistent with the official statement about performance. The reconstructed cumulative masses were further increased by 1% to compensate the difference from the official number by assuming that the error was time-independent.

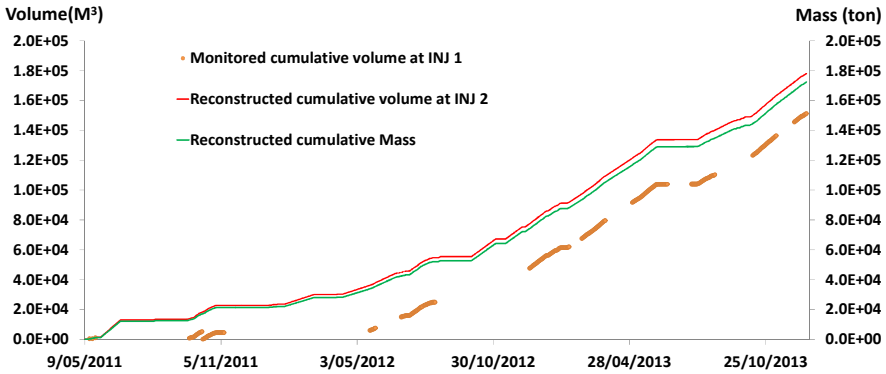

Figure 5-5 Monitored cumulative injected volumes at INJ1 and reconstructed cumulative injected volumes and masses at INJ2.

The injection rate of each injection layer was estimated based on the assumption that the mass ratio difference between two injection tests of an injection layer was linear with the injection days between the two injection tests. Figure 5-6 shows the mass rates of the four major injection layers in the period from May 9, 2011 to Dec 18, 2013.

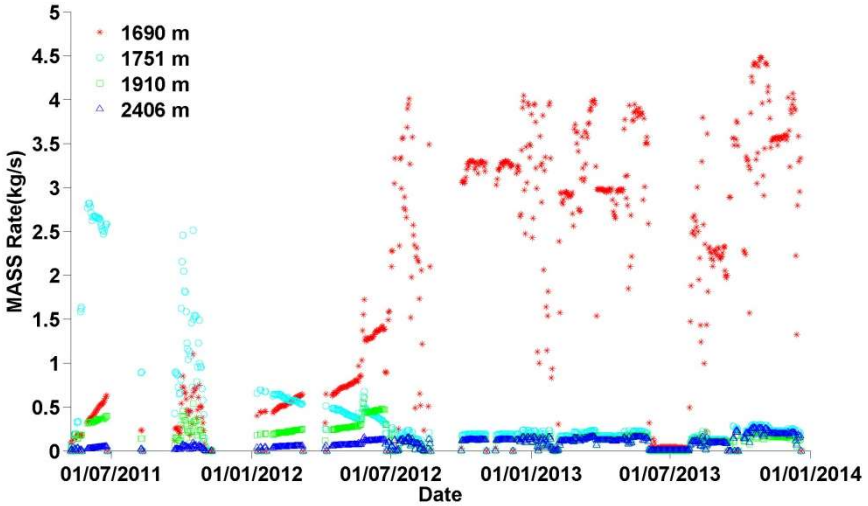

Figure 5-6 Histories of injection rates into the four layers that absorbed most CO_2.

5.4 Reservoir Response to the Injection

Monitoring data at CH1 and CH2 were filtered to reset those data far out of the normal range. Figure 5-7 shows the original and filtered pressure data at CH1 and CH2, respectively.

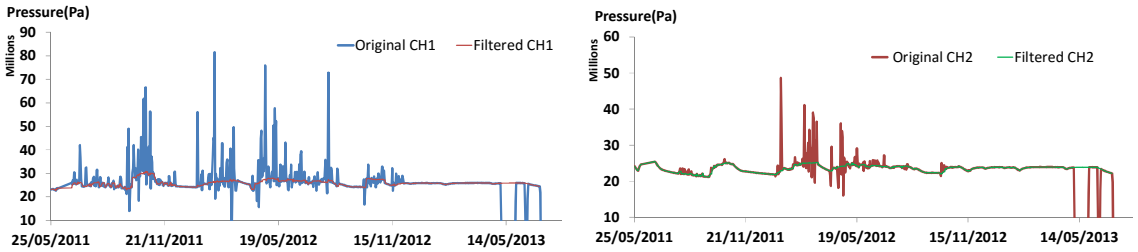

Figure 5-7 Raw and filtered pressure data at CH1 and CH2, respectively.

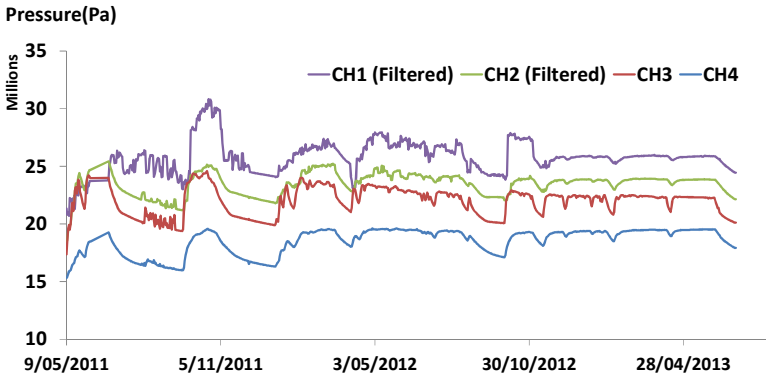

Figure 5-8 Pressure at the points of CH1 to CH4, respectively.

Recorded (filtered) pressures and temperatures at the four points of CH1, CH2, CH3, and CH4 reflected the reservoir response to the injection over time. Figure 5-8 shows the pressure response at these four points after data filtering. The four points can be divided into two groups according to the layer they were in. CH1 and CH3 were in a group of hydraulically-fractured layers, while CH2 and CH4 were in the group of unfractured layers. The shape of the pressure in the same group was similar, but pressure at CH1 and CH3 showed stronger fluctuations than that at CH2 and CH4. This could be attributed to the induced fractures that could facilitate the pressure propagation from the injection well.

Temperature at CH4, which was in the uppermost injection layer, showed little variation over time (Figure 3-11). This indicated an isothermal process in the reservoir.

5.5 CO_2 Migration Suggested by VSP Survey

Two VSP surveys conducted in 2011 and 2013 resulted in the determination of the CO_2 gas plume in the injection layers (CNPC, 2013). It was suggested by CNPC (2013) that T_{11} (Liujiagou Formation) accommodated the largest proportion of CO_2 among the formations (Figure 5-9), which was consistent with the data in the injection tests that indicated that the uppermost injection layer absorbed the most CO_2. The maximum travel distance of gas CO_2 in the injection layers was estimated to be around 350 m (Figure 5-10). The surveys also indicated

that no CO_2 had broken through the primary sealing, meaning that the storage area was safe so far.

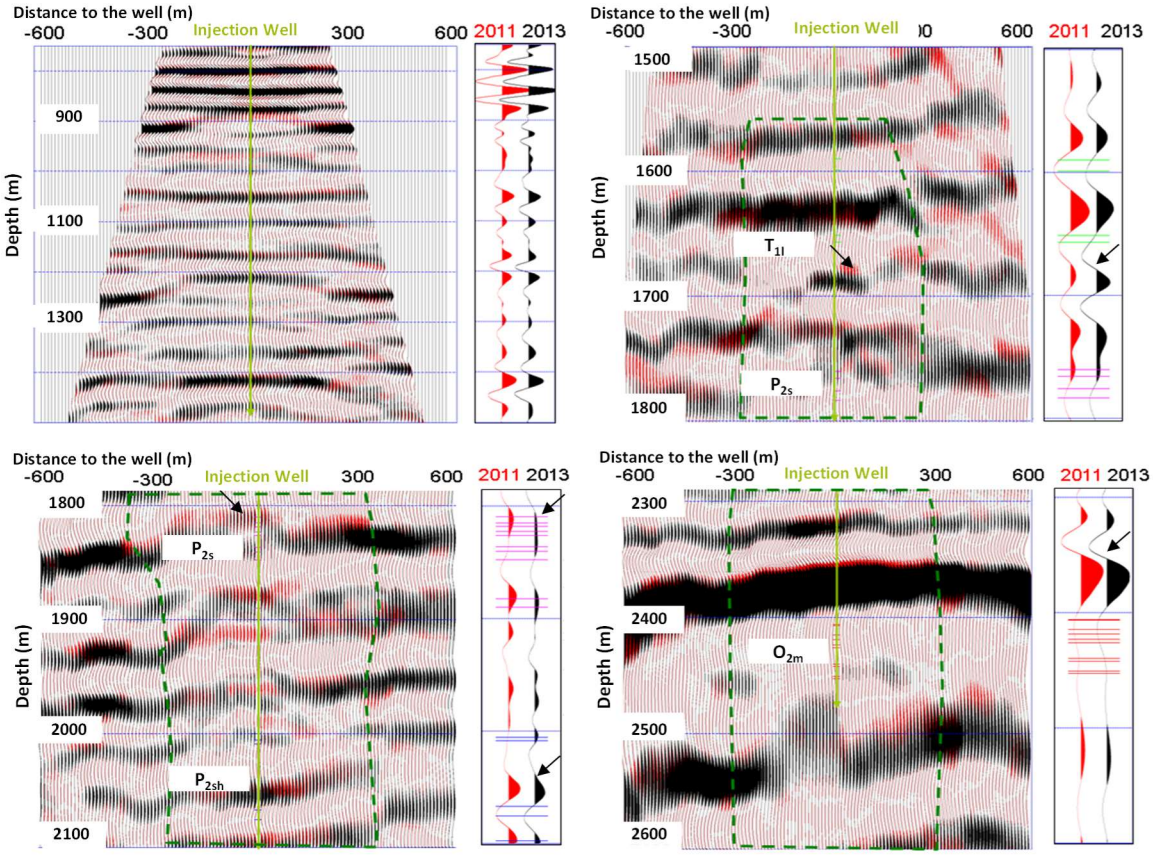

Figure 5-9 Wave comparisons on the cross section between the depths of 700 m and 2600 m, modified from CNPC (2013).

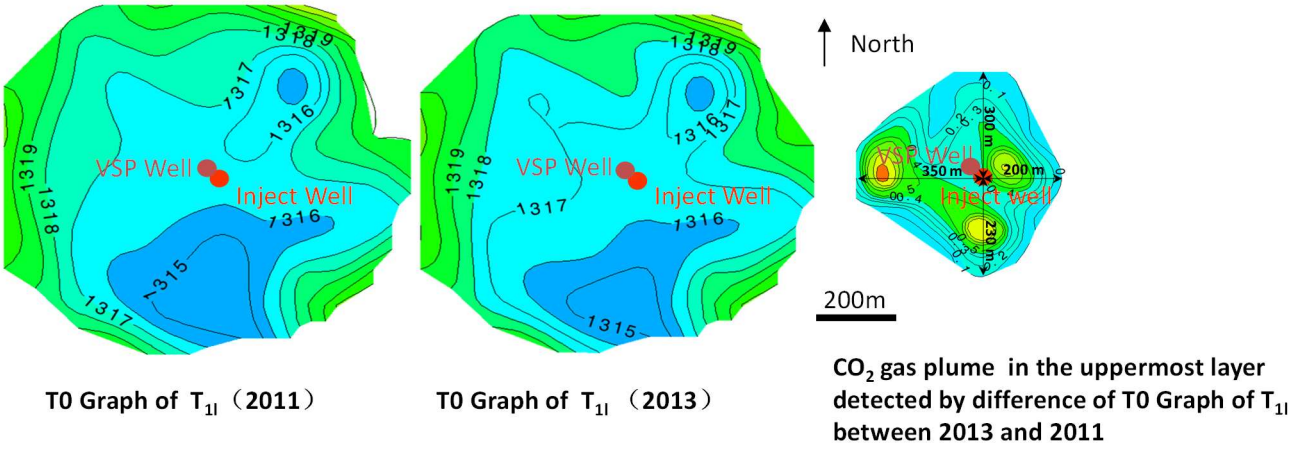

Figure 5-10 CO_2 gas plume in the uppermost layer derived from the SVP surveys, in planar view, modified from CNPC (2013).

5.6 Summary

This chapter analyzed the reservoir behavior by the field data. The in-situ data showed that the injectivity increased over the years. No strong pressure build-up occurred in the reservoir. Many injection layers, including most of the hydraulically-fractured layers, stopped absorbing CO_2 in the injection tests after 2011. The uppermost injection layer (with depths of 1690 m to 1699 m), which was unfractured, had a considerable increase in injectivity over the years and absorbed the majority of the injected CO_2 after 2011, showing a potential to meet the injection target by itself without a strong pressure build-up. The histories of the injection pressure distribution and the cumulative injected CO_2 mass were reconstructed.

CHAPTER 6 RESULTS – NUMERICAL MODELING AND ANALYSIS FOR RESEROVIR PERFORMANCE

6.1 Synopsis

This chapter presents the results of numerical modeling, about history matching, impacts of reservoir heterogeneity on reservoir performance, effectiveness of hydraulic fractures on injectivity improvement, impacts of injection procedure on reservoir performance, impacts of possible hysteresis effects accompanying the intermittent injection procedure on injectivity, and uncertainty analysis of the numerical simulations in this project.

6.2 History Match

Four aspects were considered in history matching, which is a wider range than previously in petroleum engineering with the focus on pressure in production wells. In addition to matching the pressure histories, the historical cumulative injected mass, the mass ratios in the injection layers and the CO_2 gas plume suggested by the VSP survey, were considered history matching in this thesis.

In this section, the results of history matching are presented in order. Firstly, the simulated cumulative CO_2 mass was compared with the (reconstructed) historical data because the pressure boundary was used for the injection well. Secondly, the CO_2 mass ratios in the four layers that absorbed CO_2 throughout the injection tests (at depths of 1690 m to 1699 m, 1751 m to 1756 m, 1910 m to 1923 m, and 2406 m to 2407 m) were compared with the measured data. Thirdly, the simulated pressure at CH1, CH2, CH3, and CH4, respectively, were compared against their measured data. Lastly, the resulting gas CO_2 plume in the uppermost injection layer was compared with the plume estimated by the VSP surveys. The correlation coefficient (R) and the normalized root-mean-square deviation (NRMSD) were applied to access the goodness of fit for the aspects of history matching, except for the gas CO_2 plume.

Figure 6-1 shows the simulated cumulative CO_2 mass in Scenario 1, compared with the reconstructed cumulative injected CO_2 mass history. Overall, the correlation coefficient (R) and NRMSD between the history and simulation results were 0.9822 and 8.08%, respectively. The degree of agreement between the two sequences varies in different sections. The simulated

mass matched the history well from May 2011 to around January 2012, while a 10% to 30% overestimation was found in the next 21 months, and a slight underestimation was found after September 2013. The simulated cumulative mass at the end of the simulation was around 5% less than the (reconstructed) historical data.

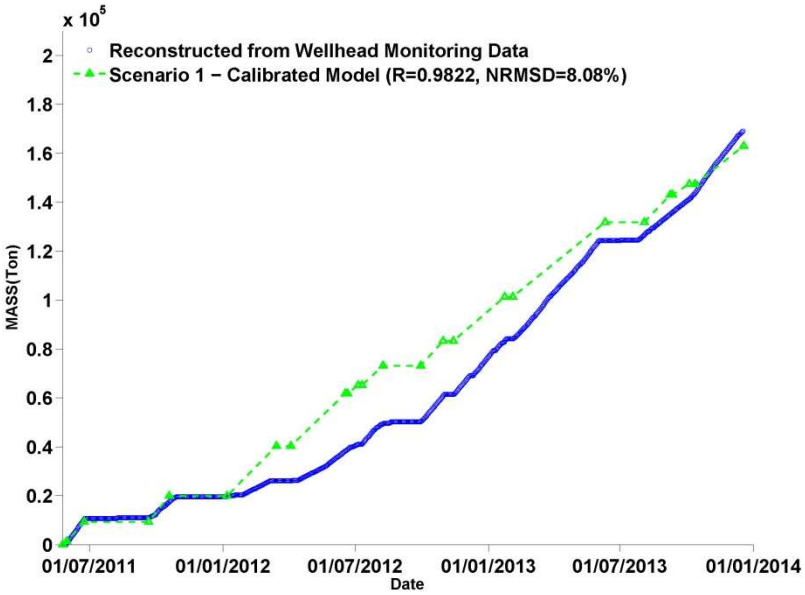

Figure 6-1 Simulated cumulative mass in Scenario 1 compared with the historical data.

As can be seen in Figure 6-2, the simulated CO_2 mass ratios in four layers that absorbed CO_2 during all the injection tests, generally matched the historical data. The monitored data showed that the mass ratios in the two layers at depths of 1690 m to 1699 m and 2406 m to 2407 m, increased over the years, while the mass ratios in the other two layers decreased over the years. In the uppermost layer (with depths of 1690 m to 1699 m), the simulated results had the best agreement with the historical data, showing the lowest NRMSD. A relatively good agreement between the simulated and the historical data was also observed in the layer at depths between 1751 m and 1756 m. In the other two layers, the resulting mass ratios showed greater NRMSDs, indicating that the agreement was not good, compared with the other two layers. The main characteristics of the performance of these layers were captured by the simulations. As only these four layers absorbed CO_2 during all the injection tests and accommodated the majority of the injected CO_2 mass from the 2012 test, the simulation results also represented the overall performance of the reservoir, in terms of contribution from these layers.

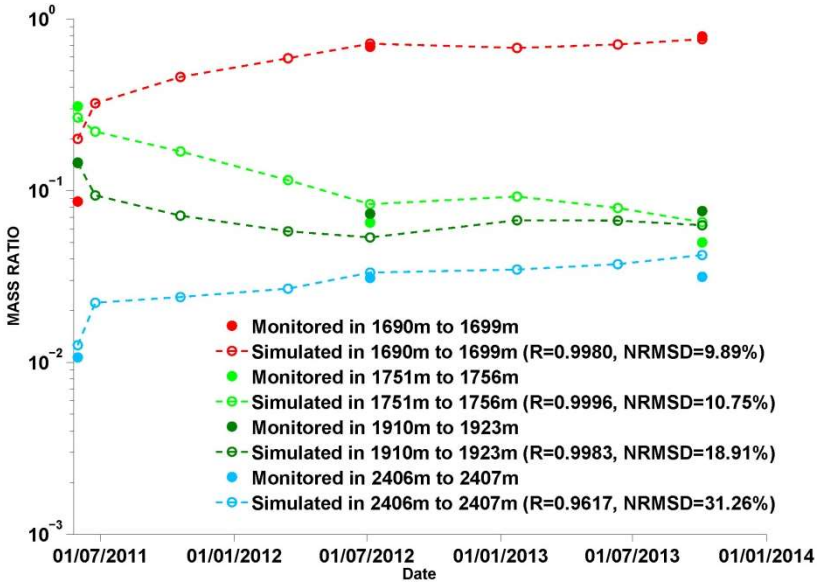

Figure 6-2 Simulated mass ratios in the four layers absorbing CO_2 in all the injection tests in Scenario 1, compared with their historical data.

Figure 6-3 shows the pressure response at CH1, CH2, CH3 and CH4 and how it replicated the histories at varying degrees of accuracy; Rs decreased and NRMSDs increased with depth, indicating a decline in goodness of fit with depth. Rs at CH1, CH2, CH3 and CH4 were 0.5304, 0.8308, 0.9330 and 0.9360, respectively, and the corresponding NRMSDs were 22.93%, 17.80%, 13.71% and 10.66%. Goodness of fit was high at CH2, CH3, and CH4, but not at CH1. The reason why the goodness of fit for CH1 was not good may come from the data filtering for this point. As the raw pressure at CH1 was extremely high (around 80 MPa) in the first half section, the filtered data in this section may not even represent the actual pressure. The simulated pressures were overestimated in the first few months, but they gradually matched the monitoring data later on. The simulated pressure series at all points matched the historical data well after November 2012, about 1.5 years after the injection started; however, the simulated pressure had a better agreement in the injection periods than in the shut-in periods, in which most of the simulated pressure was underestimated. This was because the reservoir in the shut-in periods was simulated under a dynamically-decreasing pressure boundary condition at the injection well, rather than at a hydrostatic status. Thus, the pressure drop-down in the reservoir was accelerated to some extent. The pressure series also reflects that the induced fractures facilitated pressure to transmit through the reservoir. Because CH1 and CH3 were within the hydraulically-fractured layers (Figure 3-5), the pressure fluctuations at CH1 and CH3 were more significant than those at CH2 and CH4, as both were observed in simulated results and monitoring data.

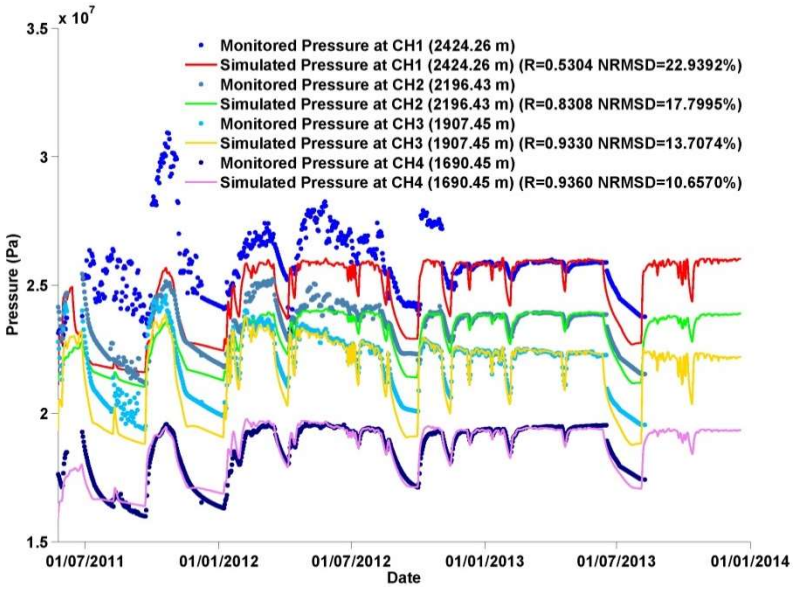

Figure 6-3 Simulated pressure at CH1 to CH4 in Scenario 1, compared with their corresponding history.

Figure 6-4 shows that the CO_2 gas plume in the uppermost injection layer (at depths of 1690 m to 1699 m) was smaller than the area detected by the VSP surveys in December 2013. Both plumes showed a movement favoring a north-westerly direction. The VSP-detected plume showed that the travel distance ranged from 200 m to 350 m. The western front of the simulated plume was about 100 m behind the VSP-estimated boundary, while other fronts were much closer to the VSP-estimated boundary. Given that the simulated cumulative mass was underestimated by 5% at the same time, it was expected that the simulated plume was smaller than the one observed.

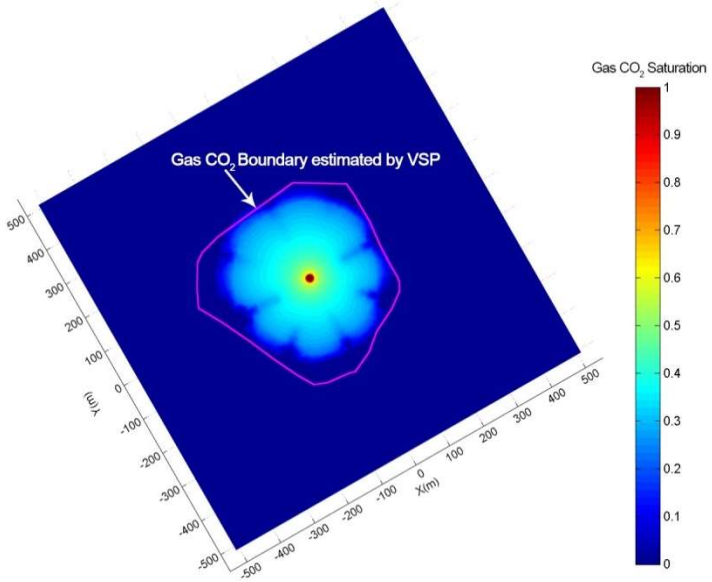

Figure 6-4 CO_2 gas plume in the uppermost layer in December 2013 in Scenario 1, compared with the VSP-estimated boundary.

Table 6-1 Comparison of average permeability of the four layers absorbing the most CO_2.

Layer	1690 m - 1699 m	1751 m - 1756 m	1910 m - 1923 m	2406 m - 2407 m
Average permeability based on AVO analysis (mD)	4.4	2.79	1.03	0.5
Average permeability based on calibrated value (mD)	37.5	1.42	1.84	1.03

The average permeability of each of the four injection layers that absorbed most CO_2 did not change significantly from the AVO-based value, due to calibration, except in the uppermost layer (at depths of 1690 m to 1699 m) (Table 6-1).

Figure 6-5 illustrates that the shape of the permeability distribution in the uppermost layer did not change to a relevant extent and neither did the planar pattern; however, the scale of permeability is different after calibration. This layer proved to be the most effective in absorbing CO_2 because its average permeability was one order of magnitude greater than that of the other layers. The calibrated distribution of this layer was meaningful, as the predominant permeability ranged between 12 mD and 40 mD, which is common in reservoirs. The calibrated permeability distribution in the uppermost injection indicated that the permeability of this layer, as suggested by the AVO, may be underestimated. The difference may be caused by the existence of small natural fractures that fell out of the AVO resolution, which could result in a high hydraulic conductivity in this layer.

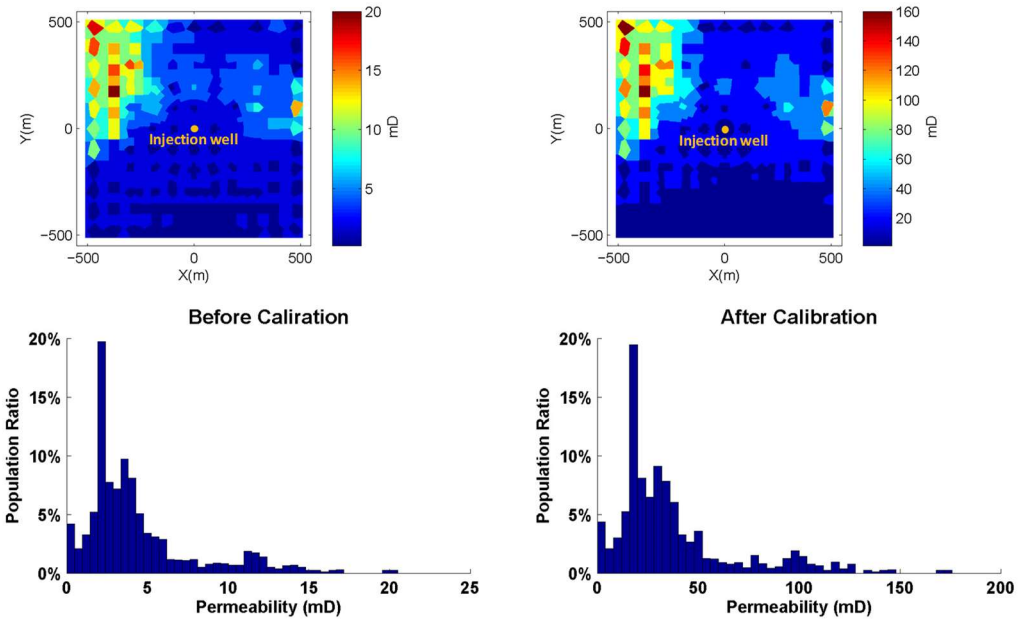

Figure 6-5 Permeability distributions in the uppermost injection layer (with depths of 1690 m to 1699 m) before and after calibration.

Figure 6-6 to Figure 6-8 show the permeability distribution changes in the other three layers. Except that a slightly significant change in the layer with depths from 1751 m and 1756 m was seen, the calibrated permeability in the other layers did not show a significant change from the AVO-based permeability.

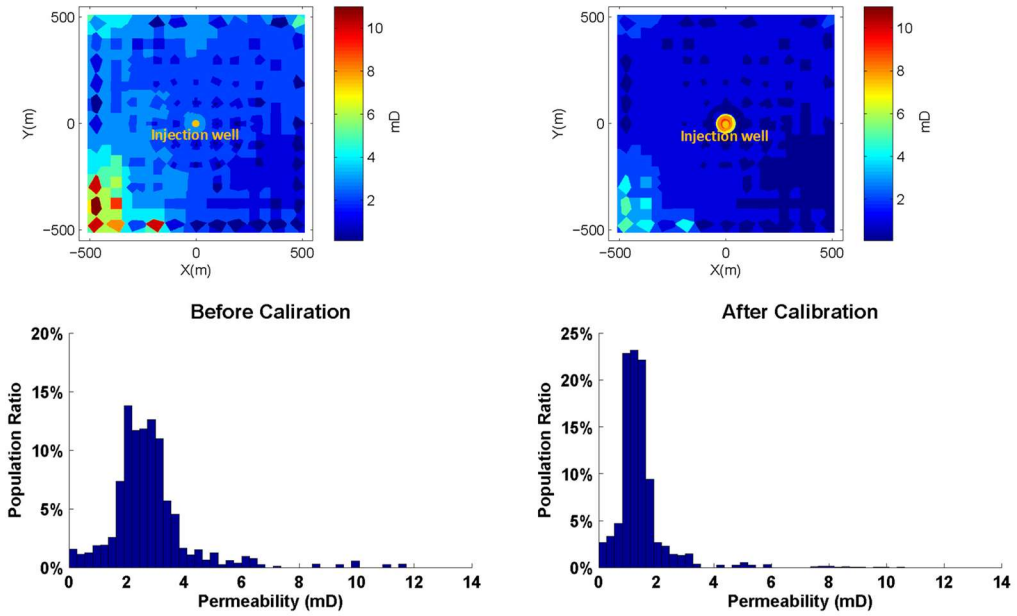

Figure 6-6 Permeability distributions in the layer with depths between 1751 m and 1756 m before and after calibration.

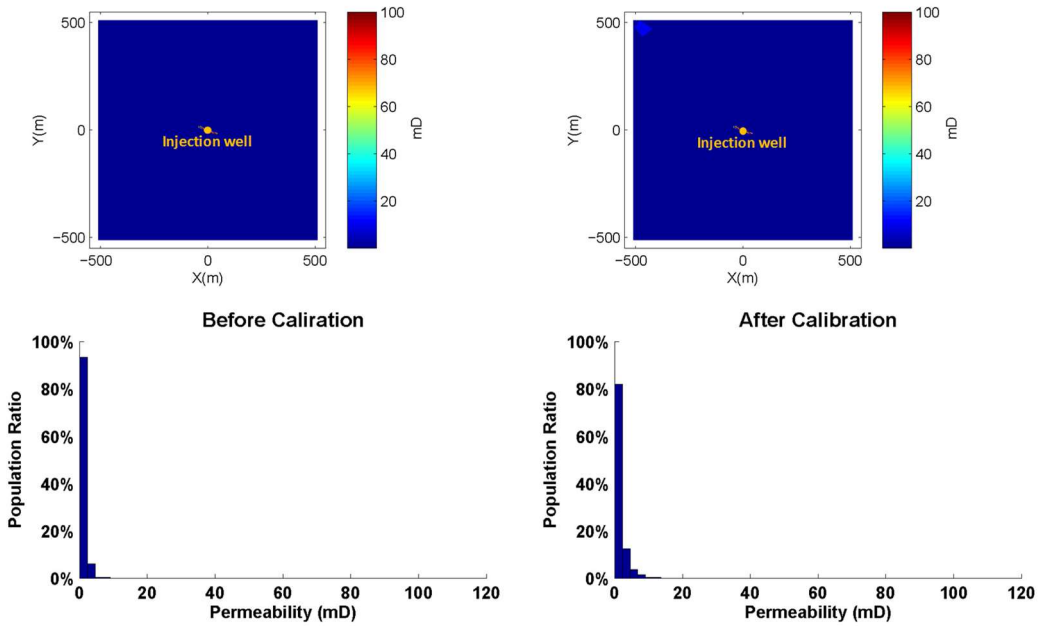

Figure 6-7 Permeability distributions in the layer with depths between 1910 m and 1923 m before and after calibration.

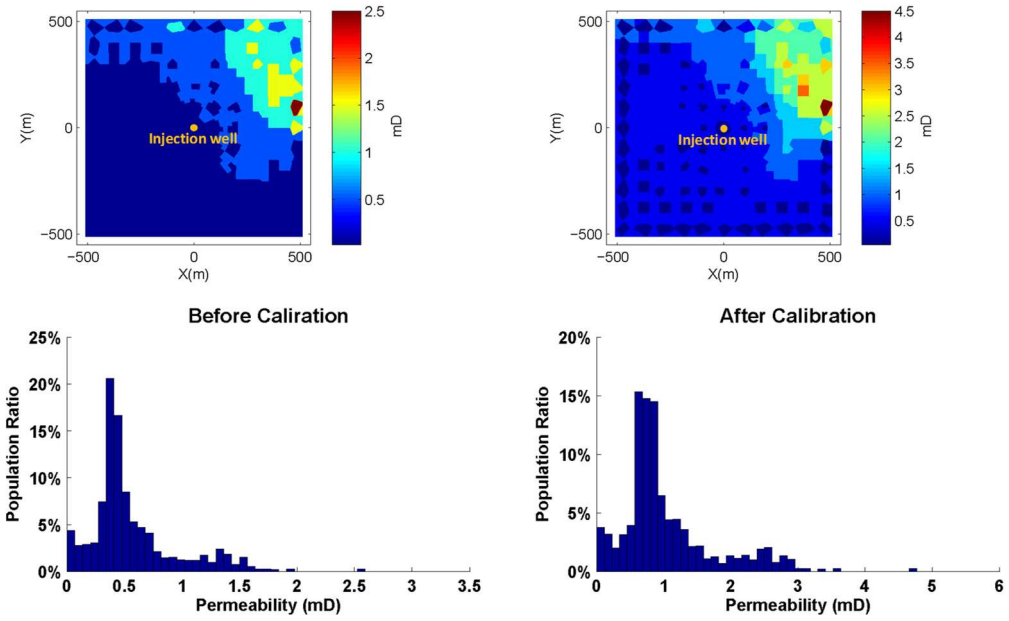

Figure 6-8 Permeability distributions in the layer with depths between 2406 m and 2407 m before and after calibration.

Furthermore, permeability becoming substantially higher away from the injection well in the north-west direction in the uppermost layer, could offer an explanation for why the injectivity in this layer grew considerably over the years.

Based on comparisons of the aspects relating to the history matching in this research, the model calibration was thought to be successful because the simulation results reproduced the features of the reservoir dynamics shown by the historical data, with discrepancies within an acceptable tolerance.

6.3 Effectiveness of Hydraulic Fracturing

Figure 6-9 shows the difference in the cumulative CO_2 mass between Scenario 1 and Scenario 2, the latter assuming no hydraulic fractures were induced. The cumulative mass in Scenario 1 was nearly 25% higher than in Scenario 2 in the beginning, but this excess declined to 8% in the first few months, and continued declining to below 5% after one year. At the end of the simulation, Scenario 1 had only around 2% more cumulative mass than Scenario 2 did. This trend indicated that the improvement in injectivity caused by the induced fractures was more significant in the early period of injection, especially in the first few months, but the overall improvement for a long period was only a few percent.

Figure 6-10 shows the comparison of cumulative mass ratios in these fractured layers between the two scenarios. Contributions from these layers in Scenario 1 were much higher

than their counterpart in Scenario 2 in the first few months, but their differences became gradually smaller afterwards. In Scenario 1, the contribution from the uppermost fractured layers (with depths of 1910 m to 1923 m) was far more considerable than the other two layers, which coincided with the monitoring data showing that the two lower layers did not absorb CO_2 in the last two injection tests (Figure 5-3). It can therefore be inferred that induced fractures can greatly facilitate the injection at the very beginning of the injection, but this improvement would be limited to a few percentage points over a long period of time. Also, as mentioned earlier, the column height of CO_2 may reduce as the injection pressure at the well head deceases, so CO_2 might not reach to the deeper layers because of the competing permeability in the upper layers.

Compared with the reservoir domain, the area affected by the hydraulic fracturing was very small around the injection well. This small area acted as a tiny reservoir with high permeability, absorbing CO_2 at an advantage in the early stage but, after its capacity was reached, it acted like a pathway for CO_2 to enter the reservoir. Thus, there was only a narrow margin in the cumulative mass at the end of the simulation between Scenarios 1 and 2. So, the overall performance of the reservoir over a long period was still highly related to its natural features.

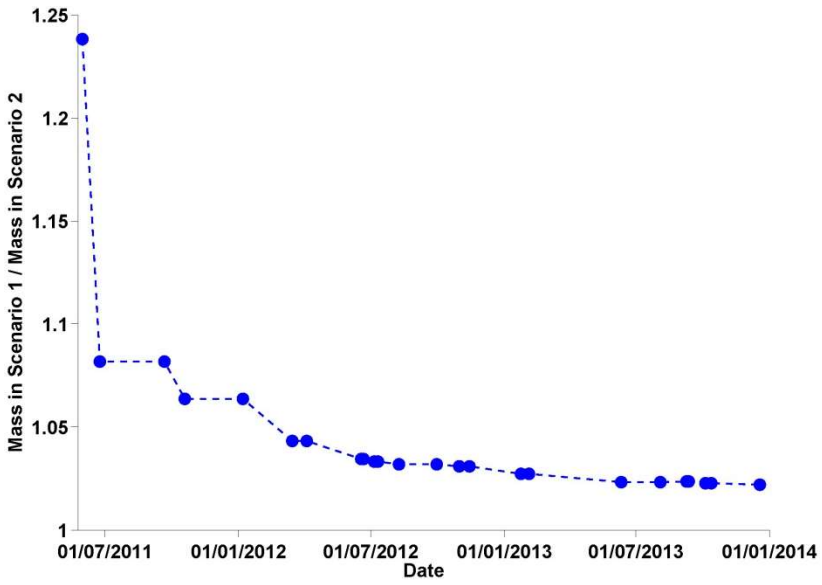

Figure 6-9 Comparison of cumulative masses between Scenario 1 (with fractures) and Scenario 2 (without fractures).

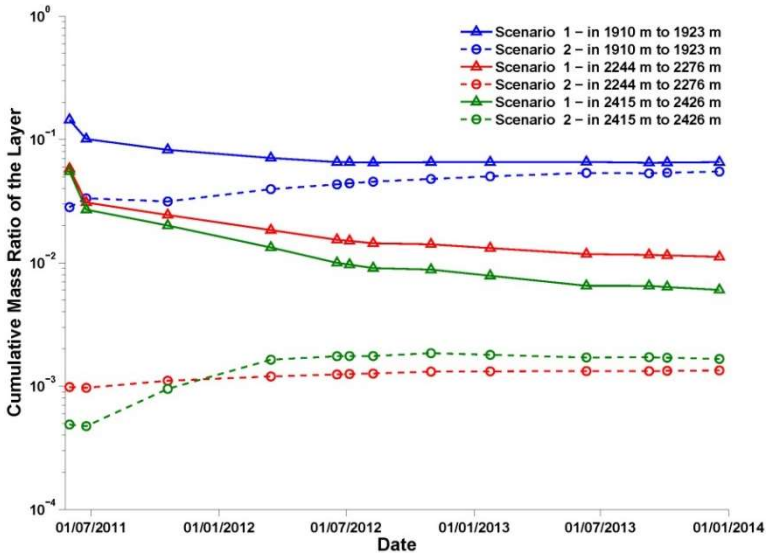

Figure 6-10 Comparison of cumulative mass ratios in hydraulically-fractured layers between Scenario 1 and Scenario 2.

6.4 Impacts of Permeability Heterogeneity

A layer-wise homogeneous model was built in Scenario 3. Permeability and porosity of each injection layer were the average values of their distributions from AVO. The average permeability of the four layers that absorbed most CO_2 used in Scenario 3 was shown in Table 6-1. Figure 6-11 Mass ratios in the four layers in the homogeneous case. shows that the mass ratios in the four layers remained at around the same level throughout the simulation, indicating that the individual performance of these layers did not change greatly over time. The observed performance variation over the years, which was captured in Scenario 1, may therefore be attributed to the heterogeneous permeability of the injection layers. The performance variation over time could be attributed to the heterogeneous permeability of the injection layers.

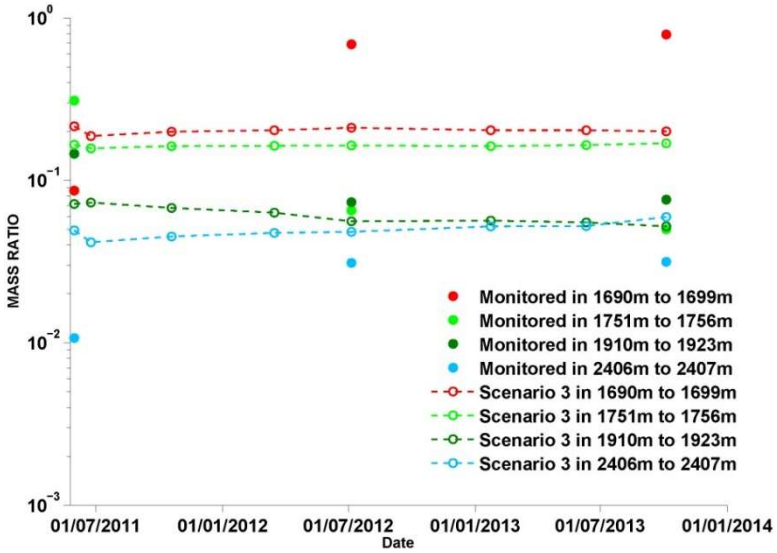

Figure 6-11 Mass ratios in the four layers in the homogeneous case.

6.5 Impacts of Injection Procedure

It was speculated that the intermittent injection procedure (in which injection and shut-in alternated)—a practical response to equipment malfunctions or no CO_2 from the factory sometimes rather than by intentional design—probably was the main reason for no intensive pressure build-up, and this also helped to maintain the injection rates to remain at the target level. Scenario 4 was simulated under a hypothesized continuous injection. The pressure for continuous injection was the averaged pressure during the injection periods in Scenario 1 and followed an overall declining tendency (Figure 6-12).

Figure 6-13 shows the differences in the cumulative mass and the average rate of the actual injection periods obtained in the two scenarios. Due to a shut-in time of more than 300 days in Scenario 1, it was not surprising to see that the cumulative mass in Scenario 1 was around 65% of that in Scenario 4, at the end of the simulation. However, the ratio of the cumulative mass in Scenario 1 to that of Scenario 4, increased after each actual shut-in period (represented by the blue dashed line in Figure 6-13). Most of the average injection rates during the actual injection period in Scenario 1 were higher than those in Scenario 4 (represented by the green bars in Figure 6-13), indicating a better performance in the actual injection periods. The average rate in the injection periods in Scenario 1 was 3.20 kg/s, a little above the target rate (3.17 kg/s), while the average rate in Scenario 4 was 3.01 kg/s.

With regard to the pressure build-up, Figure 6-14 shows the difference in the maximum pressure build-up at different distances from the injection well in the uppermost injection layer (with depths of 1690 m to 1699 m) at the end of each actual injection period between the two

scenarios. Within 10 meters around the injection well, the maximum pressure build-up ratio of Scenario 1 to Scenario 4 was between 0.9 and 1.1, which indicated the difference was between -10% and 10%, but beyond this distance, the ratio became smaller and smaller, which means that Scenario 1 had a lower overall pressure build-up in the reservoir. Therefore, more CO_2 could enter the reservoir in Scenario 4 under the same injection pressure because the resistance to CO_2 was less than in Scenario 1.

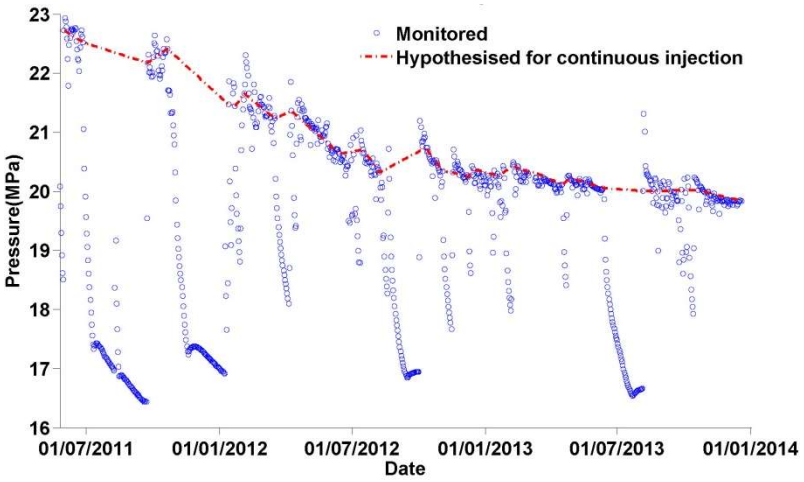

Figure 6-12 Monitored pressure at INJ2 and hypothesized pressure for continuous injection in Scenario 4.

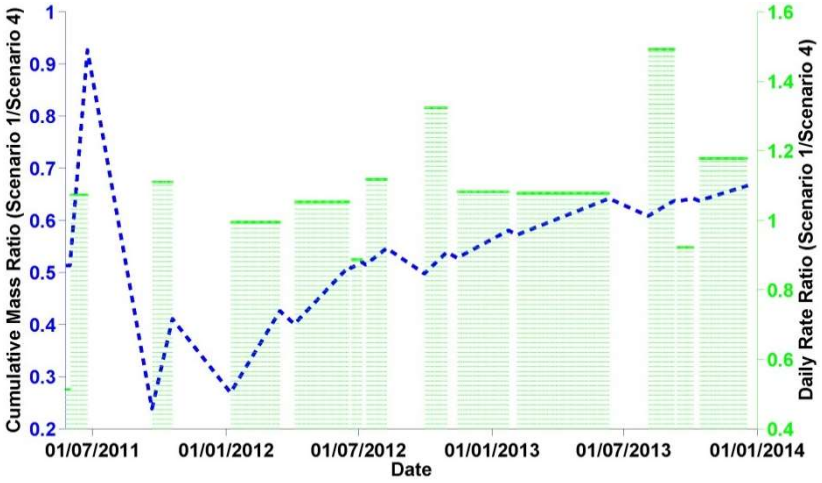

Figure 6-13 Comparisons of cumulative and daily rates between Scenario 1 and Scenario 4.

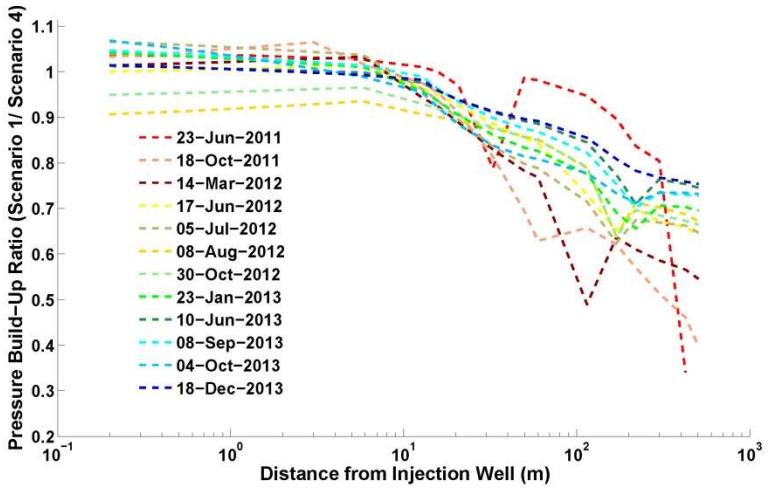

Figure 6-14 Ratio of the maximum pressure build-up at different distances from the injection well between Scenario 1 and Scenario 4 at the end of each injection period.

6.6 Impacts of Hysteresis Effects

As the injection was deployed in an intermittent way, hysteresis effects could have significant effects on the reservoir performance. Unlike the usual situation where residual trapping does not take effect until a continuous injection terminates, residual trapping in this project may be significant because there was always a transition from a drainage process to a wetting process when the injection well was shut-in.

The simulated cumulative mass in the hysteretic case, Scenario 5, was about 56% higher than the non-hysteretic case of Scenario 1 (Figure 6-15). This mass increase mainly came from the aqueous CO_2 mass growth. Figure 6-16 indicated that pressure spread out more easily in the hysteretic case than the non-hysteretic case. Within 20 m to30 m around the injection well, Scenario 5 always had a lower pressure build-up, while beyond these distances, it had a higher pressure build-up. Lower pressure build-up around the well means that the pressure spread quickly. This is because the hysteresis effects caused more gaseous CO_2 to be trapped in the reservoir and increased the chances of CO_2 being dissolved in the water which, in turn, decreased the gas CO_2 pressure in the reservoir. Thus, the injectivity increased and more CO_2 entered into the reservoir under the same injection pressure during the same time duration.

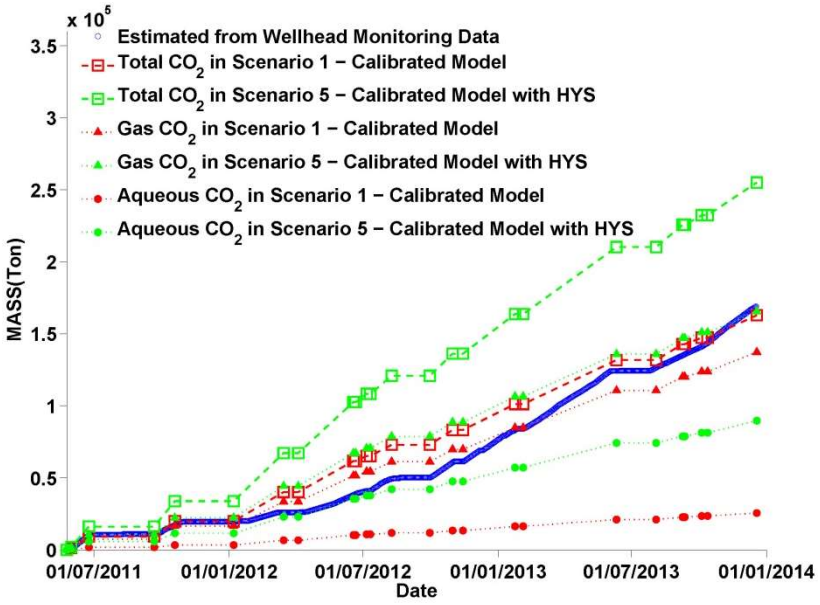

Figure 6-15 Comparison of the cumulative CO_2 mass in different phases between Scenario 1 and Scenario 5.

6.7 Reservoir Performance Prediction

The reservoir performance from December 2013 to December 2015 was estimated in Scenario 6 under the assumption that the injection procedure from December 2012 to December 2013 was repeated twice successively. Figure 6-17 shows that the total injected CO_2 mass reached 300,000 tons in Dec 2015, and that the reservoir performance declined when the average injection rate and the yearly average rate dropped slightly under that injection pressure.

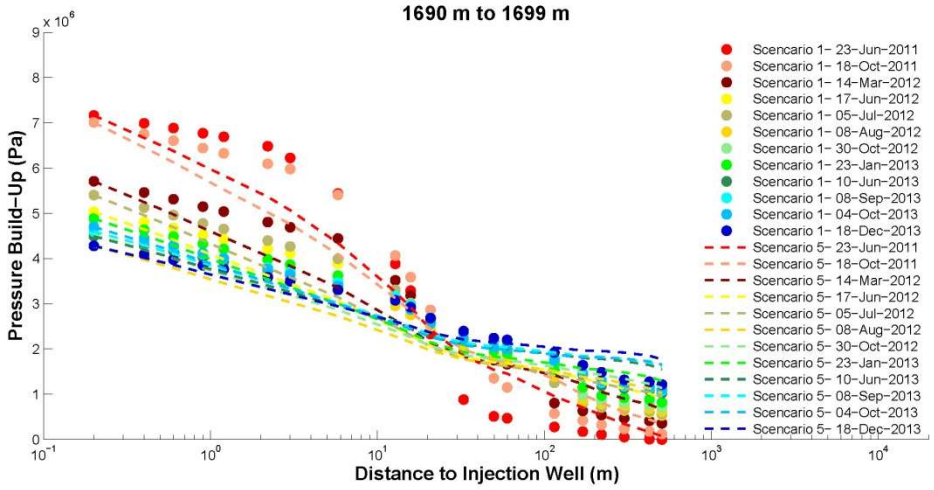

Figure 6-16 Comparison of pressure build-up over distance from the injection well between Scenario 1 and Scenario 5.

Figure 6-18 shows the pressure build-up over time at various distances from the injection well in the uppermost injection layer (with depths from 1690 m to 1699 m) for

Scenarios 1 and 6. Scenario 6 had a lower pressure build-up within 10 m from the injection well, but it had a higher pressure build-up beyond that distance. This means that the pressure from the injection well propagated to the lateral boundary, thus decreasing the pressure gradient to drive CO_2. Therefore, a slightly declining injection rate was seen in Figure 6-17.

The predicted cumulative mass could be underestimated because the higher performance indicated by the 2014 injection test was not accounted for in the calibration. Another possible reason is that the model extension (1 km × 1 km) might be too small for the simulation and that the pressure build-up gradient decreased to smaller than 2 MPa by the end of the simulation.

6.8 Sensitivity Analysis

The sensitivity analysis was conducted to look at how different boundary conditions (for the injection well and for the lateral boundary), compressibility of rock and pore of the injection layers, S_{lr} and S_{gr} and entry capillary pressure of the injection layers, would affect the simulation results. Results of cumulative mass, mass ratios in the selected layers and pressure at CH1 to CH4 from these scenarios for sensitivity analysis were compared to their counterparts in Scenario 1, except for Scenario 7, where only the pressure was compared because the cumulative mass and the mass ratios of the four injection layers absorbing most CO_2 in this scenario were identical to the historical data.

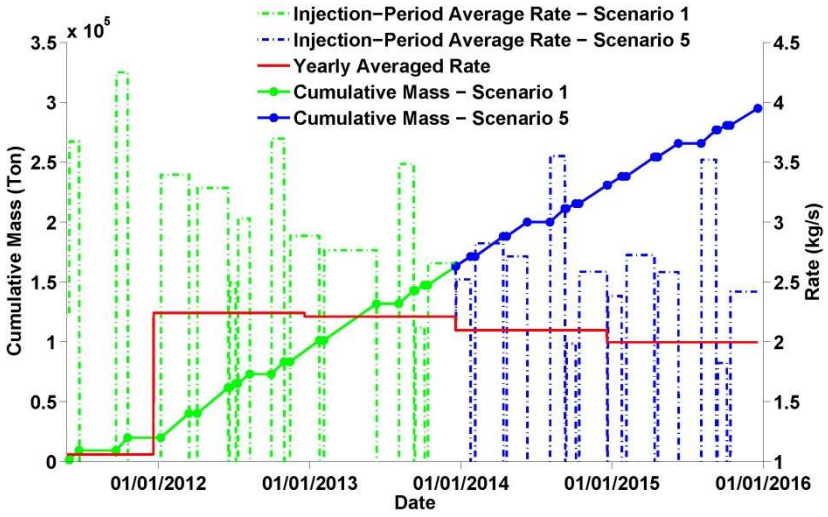

Figure 6-17 Cumulative mass and average rate during the injection periods for Scenario 1 and Scenario 6.

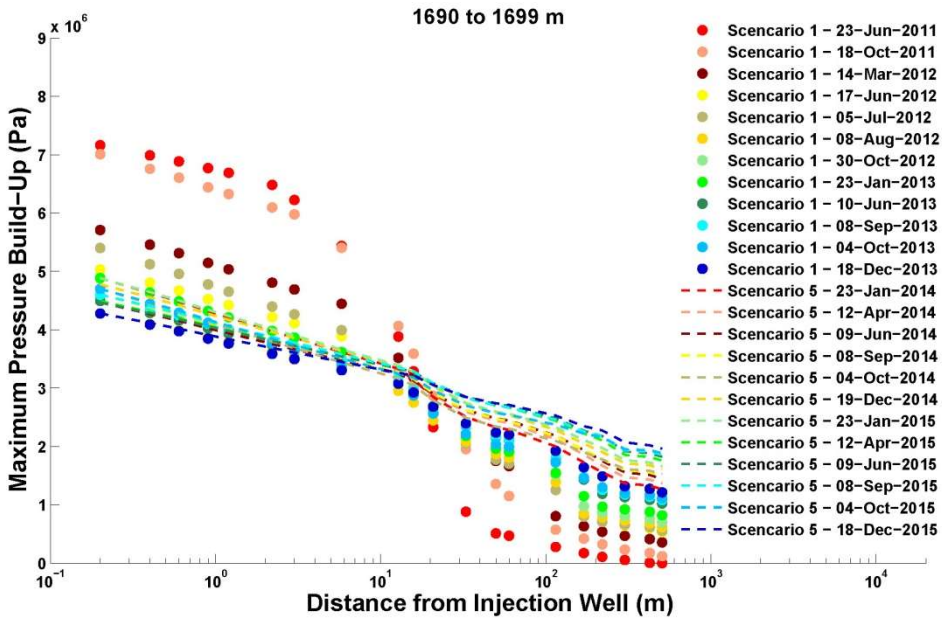

Figure 6-18 Maximum pressure build-up at different distances from the injection well over time in Scenario 1 and Scenario 6.

For the cumulative mass, Figure 6-19 shows that Scenarios 9, 10 and 12 had positive impacts on the results, but Scenarios 8, 11 and 13 had a negative influence. The most positive impact was observed in Scenario 10 at the beginning of simulation, with 43% more cumulative CO_2 mass than in Scenario 1, while the most negative impact was seen in Scenario 8 at the end of simulation, with 52% less cumulative CO_2 mass than in Scenario 1. This indicated that, given the current model size, no-flux boundary conditions (Scenario 8) could introduce serious boundary effects, while constant-pressure boundary conditions (Scenario 9) could provide an estimate of more cumulative mass. The 10% difference between Scenario 9 and Scenario 1 demonstrated that the approach to dealing with the lateral boundaries in Scenario 1 can help to reduce overestimation of the cumulative mass. So, the lateral boundary conditions treated in Scenario 1 were appropriate.

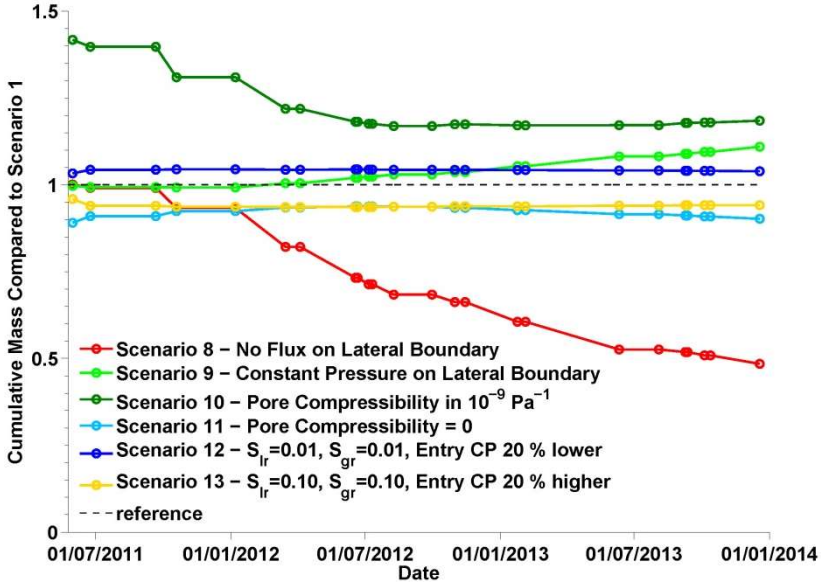

Figure 6-19 Cumulative mass comparison for Scenarios 8 to 13, relative to Scenario 1.

Regarding pore compressibility of the rock, one order of magnitude greater (Scenario 10) affected the results more significantly than the pore compressibility being neglected (Scenario 11), and the most significant effect occurred at the beginning of simulation. This indicated that, for a reservoir with pore compressibility in 10^{-9} pa^{-1}, the CO_2 storage volume gained from the changes in pore volume may be significant and should not be overlooked. However, for a reservoir with pore compressibility in 10^{-10} pa^{-1} or smaller, neglecting such volume in simulation would not make a considerable difference in the results.

Where entry capillary pressure and residual saturation of liquid and gas are concerned, Scenario 12 (making it easier for CO_2 to enter and migrate in the reservoir) and Scenario 13 (making it more difficult for CO_2 to enter and migrate in the reservoir) affected the results differently, but to the same degree. The cumulative mass in Scenario 11 was around 5% more than that in Scenario 1, while, in Scenario 13, it was around 5% less than that in Scenario 1. Given the methods for calculating the relative permeability (RP) and capillary pressure (CP) in the simulation, moderate change in these parameters would not significantly affect the results. Therefore, the cumulative mass was most sensitive to the boundary condition rather than to the fluid retention characteristics.

In terms of the mass ratio of the four injection layers that absorbed the most CO_2, Figure 6-20 shows that Scenario 8 had the most significant impact on the results, while other scenarios influenced the results in a much narrower range, compared to Scenario 1, most being between 0.9 and 1.1. Simulated mass ratios of these layers in these scenarios, except Scenario 8, were not much different from Scenario 1. However, the mass ratio in the major layer (with depths

of 1690 m to 1699 m) in Scenario 8 was up to 42% less than Scenario 1, and the mass ratio in the other layers was up to a couple of times in Scenario 1. In Scenario 9, the mass ratio of the layers at depths from 1751 m to 1756 m and from 1910 m to 1920 m, exceeded Scenario 1 a little more than 10% at the beginning, and the values in the other two layers were around 30% less than Scenario 1 in the same time period, but eventually they became closer to Scenario 1. Scenarios 9, 11, 12 and 13 had a mass ratio close to Scenario 1. Consequently, individual performance of these selected layers was still most sensitive to closed-boundary conditions.

As far as pressure at CH1 to CH4 was concerned, Figure 6-21 indicated that influence by these scenarios was different between the monitoring points. The most significant effect was observed in Scenario 7, which was 5% to 20% less than in Scenario 1. It indicated that the rate boundary condition applied to the injection well would result in significantly-different pressure in the reservoir for the same setup of the reservoir used in Scenario 1. Between the scenarios in which the pressure boundary condition used at the injection well , and with the exception of Scenario 7, which had the simulated pressure at CH4 up to 8% overestimated, pressure differences at CH1 to CH3 did not exceed 2%. This indicated that the simulated pressure was also most sensitive to the closed boundary.

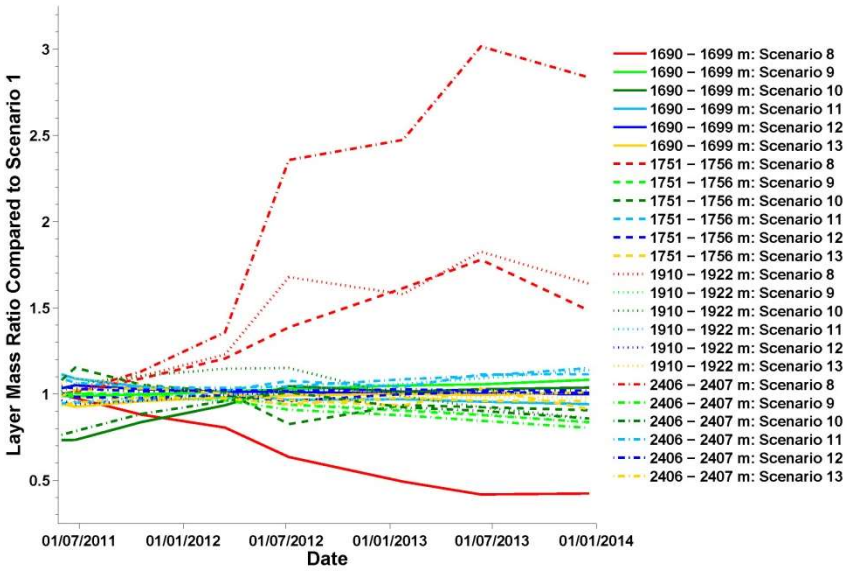

Figure 6-20 Comparison of mass ratios in the four layers for Scenarios 8-13, relative to Scenario 1.

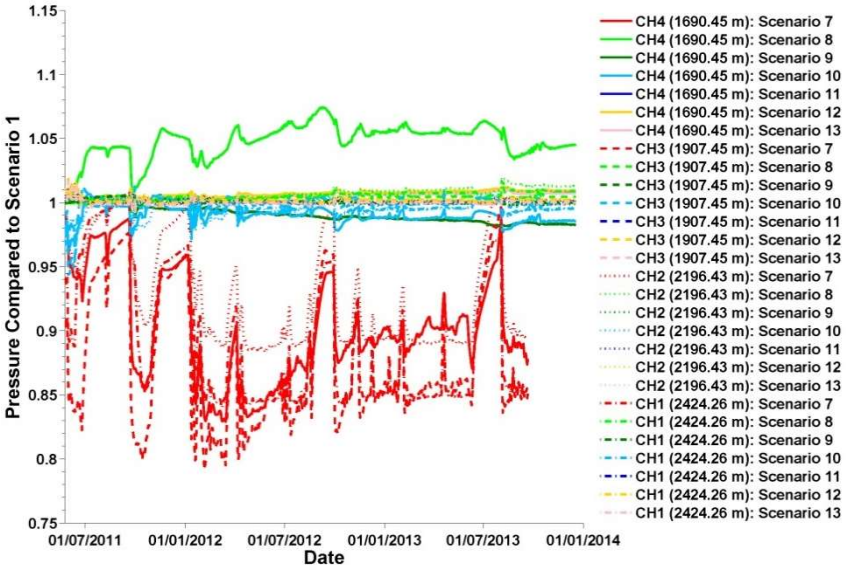

Figure 6-21 Comparison of pressure at CH1 to CH4 for Scenarios 7 to 13, relative to Scenario 1.

Note that the computational cost involved in Scenario 7 was far greater than that in Scenario 1. The main reason for this was that the time step lengths in Scenario 7 were decreased to several to tens of seconds, from thousands of seconds, once two-phase CO_2 and solid salt appeared in the grid blocks of the injection well. However, in the other scenarios, where the pressure boundary condition was used at the injection well, the variability in time step was avoided by fixing the CO_2 saturation and salinity at the injection well.

Furthermore, matching the measured pressure using the rate boundary was more difficult than using the pressure boundary, even though the former could save time in matching the cumulative mass and the mass ratios of the four layers. The difficulties were caused by the uncertainty in the rate allocation between the injection layers, and by the use of Darcy's law to describe the fluid flow in the well. Because the pressure response in a layer depends on the injection rate into that layer, any pressure changes would become negligible if the rate is close to zero. Along this reasoning, the simulated pressure at CH1 and CH2 in Scenario 7 barely showed changes over time (Figure 6-22). A similar unsatisfactory match of pressure was reported by Xie et al. (2015a) using a rate boundary at the injection well. Consequently, in this research, the use of the pressure boundary at the injection well was more reliable and more efficient to conduct the model calibration.

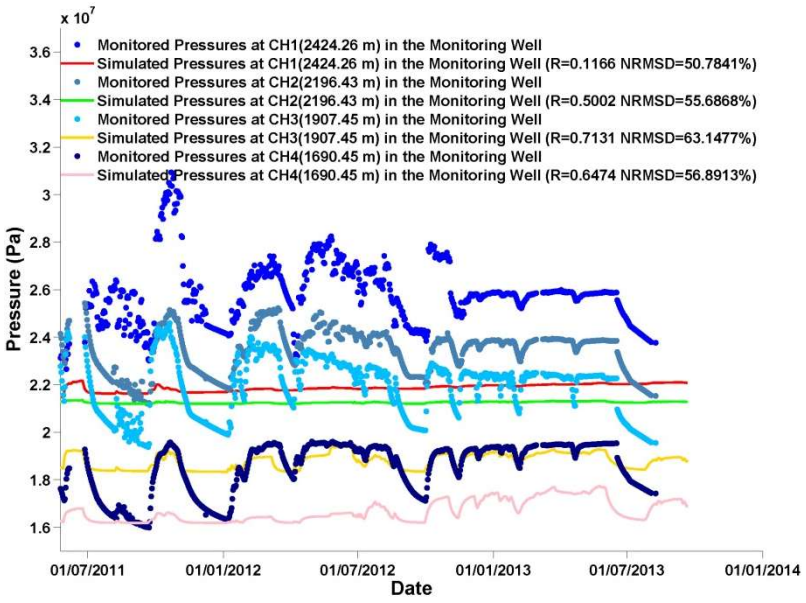

Figure 6-22 Simulated pressure at CH1 to CH4 in Scenario 7, compared with the monitoring data.

6.9 Summary

Numerical simulations using TOUGH2-MP-ECO2N was carried out to investigation into reservoir performance dynamics for this project. The main features of the reservoir performance from 2011 to 2013 were reproduced through a heterogeneous model by using a time-dependent pressure boundary condition at the injection well and calibrating the permeability distributions in the injection layers against the historical data. Several scenarios were simulated to access the impacts of permeability distribution, induced fractures and the intermittent injection procedure on the reservoir performance.

CHAPTER 7 IMPLICATIONS AND IMPROVEMENTS

7.1 Synopsis

This chapter includes the implications in the results of this research and suggestions for the further study for the project, which could be helpful in improving reservoir performance assessment and injection scheme design in practice.

7.2 Implications

It was implied in this research that reservoir heterogeneity and injection procedure could significantly affect the reservoir performance, and should be given much consideration in the pre-assessment of the reservoir performance. The real performance in the SHCCS Project was very dynamic, and it became completely different from the predictions in the pre-assessment after a few years injection. It is necessary to update the reservoir performance assessment when new field data are available.

Injectivity improvement caused by the hydraulic fractures was proved to be highly effective only in the early period of injection. The overall injectivity of the reservoir for a long term was still dependent on the natural features of the reservoir. It was observed in both the field data and the simulation results that most of the fractured layers absorbed very small amounts of CO_2 or even stopped absorbing CO_2 after the first annual injection test. This understanding is of importance when evaluating the necessity of a hydraulic fracturing operation for a reservoir with low permeability to improve its injectivity. The cost-effectiveness should be analyzed in depth to reaching the final decision.

The intermittent injection procedure employed in this project was helpful in controlling pressure build-up in the reservoir and kept the injection rate at the target level. Hysteresis effects accompanying this procedure made gas CO_2 more immobile in the shut-in periods, thus improving the chance of CO_2 to dissolve in the water, which in turn reduced the pressure around the injection well and improved the injectivity in the injection periods. Consequently, the injectivity and storage safety could be improved. This understanding could help the optimum injection scheme design, and also could assist the design to improve the injectivity of a reservoir with low permeability.

7.3 Improvements

Future study relating to this project could be carried out as the following:

(1) Improve the simulation of pressure distribution in the injection well when it was represented as a rate boundary.
(2) Couple a mechanical model in the simulation to describe the change of permeability of the fractured reservoir response to the pressure variation in the injection well;
(3) Study the relationship between the injection initiation pressure and the conductivity of the reservoir;
(4) Optimize the injection procedure for the reservoir to realize a maximum overall injection rate with minimum reservoir pressurization.

CHAPTER 8 CONCLUSIONS

Shenhua (100,000 metric tons/year) Carbon Capture and Storage (SHCCS) Demonstration Project is the first project for geological storage of CO_2 in saline aquifers in China. The reservoir's pre-assessments indicated that none of the candidate injection layers could have an injectivity to meet the target rate, and the pressure build-up was most likely above the safety limit. Therefore, hydraulic fracturing and a multi-layer injection procedure were employed to improve the reservoir injectivity and also to reduce the risk of overpressure.

However, unique reservoir response was observed in the project after the injection started. In-situ data from the annual injection tests showed that the total injection rate and the injection index increased over the years, while the corresponding injection initiation pressure reduced. No strong pressure build-up occurred in the reservoir. Although 21 saline aquifers at depths of between 1600 m and 2500 m, identified by the well log data, were all chosen to be the injection layers, only four of them did absorb CO_2 during all the injection tests from 2011 to 2014. The other layers, including most of the hydraulically-fractured layers, stopped absorbing CO_2 in the injection tests after 2011. Additionally, the uppermost injection layer (with depths of 1690 m to 1699 m), which was not fractured, increased considerably in its injectivity over the years and absorbed more than 60% CO_2 from 2012. According to the data in the last two injection tests, this layer showed a potential to meet the injection target by itself without a strong pressure build-up.

Investigation into the reservoir performance dynamics was conducted through numerical simulations using TOUGH2-MP-ECO2N. Heterogeneous permeability distributions in the injection layers were fully considered. The main features of the reservoir dynamics were reproduced by using a time-dependent pressure boundary condition at the injection well and by calibrating the permeability distributions in the injection layers against historical data. The simulation results of the cumulative injected CO_2 mass, the mass ratios of the four layers that absorbed CO_2 throughout the injection tests, the pressure at the four monitored depths and the gas CO_2 plume in the uppermost injection layer, matched the monitored data with uncertainties and discrepancies within an acceptable tolerance. The average permeability of each of the four injection layers absorbing most CO_2 did not change significantly after the calibration against historical data, except for that of the uppermost layer. The shape of the permeability

distribution in this layer did not change significantly, neither did the planar pattern; however, this layer resulted in being the most effective in absorbing CO_2, because its average permeability was one order of magnitude greater than that of the other layers. Permeability becoming substantially higher away from the injection well in a north-westerly direction in this layer, may explain why its injectivity increased considerably over the years.

Several scenarios were simulated to assess the impacts of permeability distribution, the induced fractures and the intermittent injection procedure on the reservoir performance. Comparisons of the simulation results between these scenarios and the scenario that captured the main reservoir performance features indicated that: (1) the heterogeneous permeability distributions in the injection layers may explain the variable and dynamic performance of these injection layers; (2) the injectivity improvement by the induced fractures were highly effective in the early period of injection, but dramatically reduced afterwards, so the overall injectivity over a long period of time was dependent on the reservoir's natural features; (3) the intermittent injection procedure could effectively reduce the pressure build-up in the reservoir and help maintain the injection rates at the target level because the reservoir could recover to some extent during the shut-in periods; and (4) the hysteresis effects accompanying the intermittent injection procedure made gas CO_2 more mobile during the injection periods, which facilitating the pressure to propagate from the injection well and increased the chances of CO_2 dissolving into the water in the shut-in periods.

The reservoir performance from December 2013 to December 2015 was estimated by assuming that the injection procedure from December 2012 to December 2013 was repeated twice, successively. The cumulative injected CO_2 mass reached 300,000 tons in December 2015, but the yearly average injection rate dropped slightly. The prediction could underestimate the cumulative mass and the average injection rate because the higher performance in the 2014 injection test was not accounted for in the calibration. Another reason was probably that the extension of the model was relatively small for the simulation for prediction.

The sensitivity analysis showed that the model was most sensitive to boundary conditions. A closed lateral boundary condition could cause serious boundary effects for the simulation. The storage volume for CO_2 gained from the changes of pore volume response to injection pressure, could be of significance if the reservoir had compressibility in the magnitude order of 10^{-9} pa^{-1} or greater. Changes in S_{lr}, S_{gr} and entry capillary pressure in this research did not show significant influence. The use of the rate boundary at the injection well made it more

challenging to match the monitored pressure at the four points than the use of the pressure boundary. The main reason for this may stem from the uncertainty in the rate allocation between the injection layers, and the use of Darcy's law to describe the fluid flow in the well.

In summary, the heterogeneous distributions of permeability in the injection layers could be the cause for the dynamic reservoir performance shown by the monitoring data in the SHCCS Project. Predominance of the uppermost injection layer in absorbing CO_2 could be attributed to its much higher overall permeability than that of other injection layers. A substantial increase in injectivity of this layer over the years could be attributed to the permeability becoming considerably higher away from the injection well in a north-westerly direction. The induced fractures in the reservoir greatly improved the injectivity at the beginning of the injection, but this improvement dramatically reduced afterwards. The intermittent injection procedure employed in this project was helpful in retaining the pressure build-up low in the reservoir and kept the injection rate at the target level.

ACKNOWLEDGMENTS

I would like to give many thanks to all the persons that have made this thesis possible.

Firstly, my deepest gratitude is to my supervisor, Dr. Federico Maggi. He gave me the freedom to explore the field I was interested in, and provided me with immeasurable support. His patience and guidance helped me overcome my difficulties in academic writing and presentation.

I am also deeply thankful to my co-supervisor, Prof. Keni Zhang. He offered me the precious opportunity to take part in the first geological CO_2 storage project in China. He helped me sort out many difficulties in my research work, and provided the super computer resources for me to complete the simulations.

I am also grateful to the Tianda Group Limited for sponsoring me to pursue the PhD degree in the University of Sydney. My thanks specially go to Mr. Alan Fang, Ms. Tina Xu, and Mr. Sam Tam in this company for their enthusiasm and help in the past three years.

I am also indebted to my employer—the China Institute of Geo-Environmental Monitoring—for reserving my post and also financially supporting me. My special appreciation goes to Mr. Jinwu Hou and Dr. Qingcheng He, who initially encouraged me to take this program.

I would like to acknowledge Mr. Yongsheng Wang in Shenhua Group for feeding me with the field data. I also appreciate Prof. Litang Hu in Beijing Normal University, and Changbin Guo in Tongji University, for their help in reservoir modeling and computational problems.

I am also grateful to my coworkers and friends in School of Civil Engineering for their wonderful company in my life in Sydney.

Finally, I appreciate my family for their unconditional love and support.

PUBLICATIONS

1. Li, C., Tien, N.C., Zhang, K., Jen, C.P., Hsieh, P.S., Huang, S.Y., Maggi, F. Assessment of large-scale offshore CO_2 geological storage in Western Taiwan Basin. International Journal of Greenhouse Gas Control 19 (2013): 281-298.

2. Li, C. Guo, C., Zhang, K., Maggi, F., Impacts of formation heterogeneity, injection procedure and hysteresis effects on the reservoir performance in CO_2 geological storage in the Ordos Basin in China. TOUGH2 Symposium in 2015, Lawrence Berkely National Lab, California, US, September 28–30, 2015.

3. Li, C., Zhang, K., Wang, Y., Guo, C., Maggi, F. Experimental and numerical analysis of reservoir performance for geological CO_2 storage in the Ordos Basin in China. Int. J. Greenhouse Gas Control. 45 (2016): 216-232.

4. Guo, C., Zhang, K., Li, C. Influence of permeability on the initial gas bubble evolution in compressed air energy storage in aquifers. TOUGH2 Symposium 2015, Lawrence Berkely National Lab, California, US, September 28-30, 2015.

REFERENCES

Abou-Kassem, J.H., Farouq-Ali, S., Islam, M.R., 2013. Petroleum Reservoir Simulations. Elsevier.

Altunin, V.V., 1975. Thermophysical Properties of Carbon Dioxide. Publishing House of Standards, Moscow.

Aunzo, Z.P., 2008. Wellbore models GWELL, GWNACL, and HOLA user's guide. Lawrence Berkeley National Laboratory.

Bachu, S., 2000. Sequestration of CO2 in geological media: criteria and approach for site selection in response to climate change. Energ Convers Manage 41, 953-970.

Bachu, S., 2002. Sequestration of CO2 in geological media in response to climate change: road map for site selection using the transform of the geological space into the CO2 phase space. Energ Convers Manage 43, 87-102.

Bachu, S., 2015. Review of CO2 storage efficiency in deep saline aquifers. Int J Greenh Gas Con 40, 188-202.

Bachu, S., Adams, J.J., 2003. Sequestration of CO2 in geological media in response to climate change: capacity of deep saline aquifers to sequester CO2 in solution. Energ Convers Manage 44, 3151-3175.

Bandilla, K.W., Celia, M.A., Elliot, T.R., Person, M., Ellett, K.M., Rupp, J.A., Gable, C., Zhang, Y., 2012. Modeling carbon sequestration in the Illinois Basin using a vertically-integrated approach. Computing and Visualization in Science 15, 39-51.

Bandilla, K.W., Celia, M.A., Leister, E., 2014. Impact of Model Complexity on CO_2 plume modeling at Sleipner. Energy Procedia 63, 3405-3415.

Barenblast, G., Zheltov, Y.P., 1960. Fundamental equations of filtration of homogeneous liquids in fissured rocks, Soviet Physics Doklady, p. 522.

Benson, S.M., 2006. Monitoring Carbon Dioxide Sequestration in Deep Geological Formations for Inventory Verification and Carbon Credits, SPE Annual Technical Conference and Exhibition. Society of Petroleum Engineers, San Antonio, Texas, U.S.A.

Birkholzer, J.T., Nicot, J.P., Oldenburg, C.M., Zhou, Q., Kraemer, S., Bandilla, K., 2011. Brine flow up a well caused by pressure perturbation from geologic carbon sequestration: Static and dynamic evaluations. Int J Greenh Gas Con 5, 850-861.

Birkholzer, J.T., Zhou, Q.L., Tsang, C.F., 2009. Large-scale impact of CO2 storage in deep saline aquifers: A sensitivity study on pressure response in stratified systems. Int J Greenh Gas Con 3, 181-194.

Bond, C.E., Wightman, R., Ringrose, P.S., 2013. The influence of fracture anisotropy on CO_2 flow. Geophys Res Lett 40, 1284-1289.

Bourbiaux, B., Cacas, M., Sarda, S., Sabathier, J., 1998. A rapid and efficient methodology to convert fractured reservoir images into a dual-porosity model. Oil & Gas Science and Technology 53, 785-799.

Cacas, M.C., Ledoux, E., Demarsily, G., Barbreau, A., Calmels, P., Gaillard, B., Margritta, R., 1990a. Modeling Fracture Flow with a Stochastic Discrete Fracture Network - Calibration and Validation .2. The Transport Model. Water Resources Research 26, 491-500.

Cacas, M.C., Ledoux, E., Demarsily, G., Tillie, B., Barbreau, A., Durand, E., Feuga, B., Peaudecerf, P., 1990b. Modeling Fracture Flow with a Stochastic Discrete Fracture Network - Calibration and Validation .1. The Flow Model. Water Resources Research 26, 479-489.

Cavanagh, A.J., Haszeldine, R.S., 2014. The Sleipner storage site: Capillary flow modeling of a layered CO_2 plume requires fractured shale barriers within the Utsira Formation. Int J Greenh Gas Con 21, 101-112.

Celia, M., Bachu, S., Nordbotten, J., Bandilla, K., 2015. Status of CO_2 storage in deep saline aquifers with emphasis on modeling approaches and practical simulations. Water Resour Res.

Chang, C., Zhou, Q., Guo, J., Yu, Q., 2014. Supercritical CO 2 dissolution and mass transfer in low-permeability sandstone: Effect of concentration difference in water-flood experiments. Int J Greenh Gas Con 28, 328-342.

Chang, C., Zhou, Q., Xia, L., Li, X., Yu, Q., 2013. Dynamic displacement and non-equilibrium dissolution of supercritical CO 2 in low-permeability sandstone: An experimental study. Int J Greenh Gas Con 14, 1-14.

CNPC, 2010. Well Completion Report of Exploration Well for Shenhua 100000 ton/year CCS Projection (Internal report in Chinese). North China Headquarters, CNPC Logging CO., LTD.

CNPC, 2013. Application of Time-Lapse VSP Survey in Monitoring Geological CO_2 Storage for the SHCCS Project (internal report in Chinese). CNPC, CO. LTD.

Corey, A.T., 1954. The Interrelation between Gas and Oil Relative Premeabilities. Producers Monthly, 4.

Cronshaw, M.B., Bolling, J.D., 1982. A numerical model of the non-isothermal flow of carbon dioxide in wellbores, SPE California Regional Meeting. Society of Petroleum Engineers.

David, C., Gueguen, Y., Pampoukis, G., 1990. Effective medium theory and network theory applied to the transport properties of rock. Journal of Geophysical Research: Solid Earth (1978–2012) 95, 6993-7005.

De Marsily, G., 1986. Quantitative hydrogeology.

Dershowitz, B., LaPointe, P., Eiben, T., Wei, L.L., 2000. Integration of discrete feature network methods with conventional simulator approaches. Spe Reservoir Evaluation & Engineering 3, 165-170.

Dershowitz, W., Lapointe, P., 1994. Discrete Fracture Approaches for Oil and Gas Applications. Rock Mechanics: Models and Measurements Challenges from Industry, 19-30.

Doetsch, J., Kowalsky, M.B., Doughty, C., Finsterle, S., Ajo-Franklin, J.B., Carrigan, C.R., Yang, X., Hovorka, S.D., Daley, T.M., 2013. Constraining CO 2 simulations by coupled modeling and inversion of electrical resistance and gas composition data. Int J Greenh Gas Con 18, 510-522.

Doughty, C., Freifeld, B., Trautz, R., 2008. Site characterization for CO2 geologic storage and vice versa: the Frio brine pilot, Texas, USA as a case study. Environ Geol 54, 1635-1656.

Doughty, C., Pruess, K., 2004. Modeling supercritical carbon dioxide injection in heterogeneous porous media. Vadose Zone J 3, 837-847.

Eiken, O., Ringrose, P., Hermanrud, C., Nazarian, B., Torp, T.A., Hoier, L., 2011. Lessons Learned from 14 years of CCS Operations: Sleipner, In Salah and Snohvit. Enrgy Proced 4, 5541-5548.

Estublier, A., Lackner, A.S., 2009. Long-term simulation of the Snøhvit CO 2 storage. Energy Procedia 1, 3221-3228.

Finley, R.J., 2014. An overview of the Illinois Basin–Decatur project. Greenhouse Gases: Science and Technology 4, 571-579.

Gasda, S.E., Stephansen, A., Aavatsmark, I., Dahle, H.K., 2013. Upscaled Modeling of CO_2 Injection and Migration with Coupled Thermal Processes. Energy Procedia 40, 384-391.

GCCSI, 2014. The Global Status of CCS: 2014 Summary Report. Global CCS Institute, p. 12.

GCCSI, 2015. What is CCS? Global CCS Institute.

Gemmer, L., Hansen, O., Iding, M., Leary, S., Ringrose, P., 2012. Geomechanical response to CO_2 injection at Krechba, In Salah, Algeria. First Break 30, 79-84.

Gilman, J.R., Kazemi, H., 1988. Improved Calculations for Viscous and Gravity Displacement in Matrix Blocks in Dual-Porosity Simulators. Journal of Petroleum Technology 40, 60-70.

Gollakota, S., McDonald, S., 2014. Commercial-scale CCS Project in Decatur, Illinois–Construction Status and Operational Plans for Demonstration. Energy Procedia 63, 5986-5993.

Goodarzi, S., Settari, A., Keith, D., 2011. Geomechanical modeling for CO_2 Storage in Wabamun Lake Area of Alberta, Canada. Enrgy Proced 4, 3399-3406.

Haas Jr, J.L., 1976. Physical properties of the coexisting phases and thermochemical properties of the H 2 O component in boiling NaCl solutions. US Govt. Print. Off.

He, T., Ruan, Z., Guo, Q., Zhou, J., 2010. Interpretation Results of 3D Seismic Data Aquisition for Shenhua Ordos 100000 ton/year CCS Project (Internal Report in Chinese). Changqing Institute of BGP INC., China National Peteroleum Corporation.

He, Z., 2003. Evolution of the Ordos Basin and its Oil and Gas Resources. Petroleum Industry Press, Beijing.

Herzog, H., Eliasson, B., Kaarstad, O., 2000. Capturing greenhouse gases. Sci Am 282, 72-79.

Hill, A., Thomas, G., 1985. A new approach for simulating complex fractured reservoirs, Middle East Oil Technical Conference and Exhibition.

Himmelblau, D., 1959. Partial Molar Heats and Entropies of Solution for Gases Dissolved in Water from the Freezing to Near the Critical Point. The Journal of Physical Chemistry 63, 1803-1808.

Hitchon, B., Gunter, W.D., Gentzis, T., Bailey, R.T., 1999. Sedimentary basins and greenhouse gases: a serendipitous association. Energ Convers Manage 40, 825-843.

Holloway, S., 1996. An overview of the Joule II project the underground disposal of carbon dioxide. Energ Convers Manage 37, 1149-1154.

Holloway, S., 2005. Underground sequestration of carbon dioxide - a viable greenhouse gas mitigation option. Energy 30, 2318-2333.

Hosa, A., Esentia, M., Stewart, J., Haszeldine, S., 2011. Injection of CO_2 into saline formations: Benchmarking worldwide projects. Chem Eng Res Des 89, 1855-1864.

Hosseini, S.A., Lashgari, H., Choi, J.W., Nicot, J.-P., Lu, J., Hovorka, S.D., 2013. Static and dynamic reservoir modeling for geological CO_2 sequestration at Cranfield, Mississippi, USA. Int J Greenh Gas Con 18, 449-462.

Hovorka, S.D., Benson, S.M., Doughty, C., Freifeld, B.M., Sakurai, S., Daley, T.M., Kharaka, Y.K., Holtz, M.H., Trautz, R.C., Nance, H.S., 2006. Measuring permanence of CO2 storage in saline formations: the Frio experiment. Environmental Geosciences 13, 105-121.

Hovorka, S.D., Doughty, C., Benson, S.M., Pruess, K., Knox, P.R., 2004. The impact of geological heterogeneity on CO2 storage in brine formations: a case study from the Texas Gulf Coast. Geological Society, London, Special Publications 233, 147-163.

Hu, L., Pan, L., Zhang, K., 2012. Modeling brine leakage to shallow aquifer through an open wellbore using T2WELL/ECO2N. Int J Greenh Gas Con 9, 393-401.

Iding, M., Ringrose, P., 2010. Evaluating the impact of fractures on the performance of the In Salah CO 2 storage site. Int J Greenh Gas Con 4, 242-248.

IPCC, 2005. IPCC special report on carbon dioxide capture and storage / edited by Bert Metz ... [et al.] ; prepared by Working Group III of the Intergovernmental Panel on Climate Change. Cambridge : Cambridge University Press, for the Intergovernmental Panel on Climate Change, 2005.

IPCC, 2014. Climate Change 2014: Synthesis Report. Contribution of Working Groups I, II and III to the Fifth Assessment Report of the Intergovernmental Panel on Climate Change. IPCC, Geneva, Switzerland.

Jafari, A., 2011. Permeability estimation of fracture networks, University of Alberta. Dept. of Civil and Environmental Engineering.,.

Jafari, A., Babadagli, T., 2012. Estimation of equivalent fracture network permeability using fractal and statistical network properties. J Petrol Sci Eng 92-93, 110-123.

Jiang, P., Li, X., Xu, R., Wang, Y., Chen, M., Wang, H., Ruan, B., 2014. Thermal modeling of CO_2 in the injection well and reservoir at the Ordos CCS demonstration project, China. Int J Greenh Gas Con 23, 135-146.

Johnson, J.W., Nitao, J.J., Knauss, K.G., 2004. Reactive transport modeling of CO2 storage in saline aquifers to elucidate fundamental processes, trapping mechanisms and sequestration partitioning. Geological storage of carbon dioxide 233, 107-128.

Kempka, T., Class, H., Görke, U.-J., Norden, B., Kolditz, O., Kühn, M., Walter, L., Wang, W., Zehner, B., 2013a. A dynamic flow simulation code intercomparison based on the revised static model of the Ketzin pilot site. Energy Procedia 40, 418-427.

Kempka, T., Klein, E., De Lucia, M., Tillner, E., Kühn, M., 2013b. Assessment of Long-term CO_2 Trapping Mechanisms at the Ketzin Pilot Site (Germany) by Coupled Numerical Modelling. Energy Procedia 37, 5419-5426.

Kempka, T., Kühn, M., 2013. Numerical simulations of CO2 arrival times and reservoir pressure coincide with observations from the Ketzin pilot site, Germany. Environ Earth Sci 70, 3675-3685.

Kempka, T., Kühn, M., Class, H., Frykman, P., Kopp, A., Nielsen, C., Probst, P., 2010. Modelling of CO_2 arrival time at Ketzin–Part I. Int J Greenh Gas Con 4, 1007-1015.

Kirkpatrick, S., 1973. Percolation and conduction. Reviews of modern physics 45, 574.

Klein, E., De Lucia, M., Kempka, T., Kühn, M., 2013. Evaluation of long-term mineral trapping at the Ketzin pilot site for CO_2 storage: An integrative approach using geochemical modelling and reservoir simulation. Int J Greenh Gas Con 19, 720-730.

Kuang, D.-q., Li, Q., Wang, Y.-s., Wang, X.-j., Lin, Q., Wei, X.-c., Song, R.-r., 2014. Numerical simulation of distribution of migration of CO_2 in Shenhua carbon capture and storage demonstration project. Rock and Soil Mechanics 35, 2623-2633.

Lake, L.W., Jenson, J.L., 1991. A Revie of Heterogeneity Measures used in Reserovoir Characterization. In Situ 15, 409-439.

Lengler, U., De Lucia, M., Kühn, M., 2010. The impact of heterogeneity on the distribution of CO_2: Numerical simulation of CO_2 storage at Ketzin. Int J Greenh Gas Con 4, 1016-1025.

Li, C., Tien, N.-C., Zhang, K., Jen, C.-P., Hsieh, P.-S., Huang, S.-Y., Maggi, F., 2013. Assessment of large-scale offshore CO< sub> 2</sub> geological storage in Western Taiwan Basin. International Journal of Greenhouse Gas Control 19, 281-298.

Ling, L.-l., Xu, Y.-q., Wang, Y.-s., Zhang, K.-n., 2013. Application of numerical simulation to pilot project of CO_2 geological sequestration. Rock and Soil Mechanics 34, 2017-2022.

Liu, H., Hou, Z., Were, P., Gou, Y., Sun, X., 2014. Simulation of CO_2 plume movement in multilayered saline formations through multilayer injection technology in the Ordos Basin, China. Environ Earth Sci 71, 4447-4462.

Liu, H., Hou, Z., Were, P., Gou, Y., Xiong, L., Sun, X., 2015. Modelling CO_2-brine-rock interactions in the Upper Paleozoic formations of Ordos Basin used for CO_2 sequestration. Environ Earth Sci 73, 2205-2222.

Long, J.C.S., Gilmour, P., Witherspoon, P.A., 1985. A Model for Steady Fluid-Flow in Random 3-Dimensional Networks of Disc-Shaped Fractures. Water Resources Research 21, 1105-1115.

Long, J.C.S., Remer, J.S., Wilson, C.R., Witherspoon, P.A., 1982. Porous-Media Equivalents for Networks of Discontinuous Fractures. Water Resources Research 18, 645-658.

Lough, M.F., Lee, S.H., Kamath, J., 1997. A new method to calculate effective permeability of gridblocks used in the simulation of naturally fractured reservoirs. SPE Reservoir Engineering 12, 219-224.

Lu, M., Connell, L.D., 2008. Non-isothermal flow of carbon dioxide in injection wells during geological storage. Int J Greenh Gas Con 2, 248-258.

Lucier, A., Zoback, M., 2008. Assessing the economic feasibility of regional deep saline aquifer CO2 injection and storage: A geomechanics-based workflow applied to the Rose Run sandstone in Eastern Ohio, USA. Int J Greenh Gas Con 2, 230-247.

Maldal, T., Tappel, I., 2004. CO_2 underground storage for Snøhvit gas field development. Energy 29, 1403-1411.

Martens, S., Kempka, T., Liebscher, A., Lüth, S., Möller, F., Myrttinen, A., Norden, B., Schmidt-Hattenberger, C., Zimmer, M., Kühn, M., 2012. Europe's longest-operating on-shore CO_2 storage site at Ketzin, Germany: a progress report after three years of injection. Environ Earth Sci 67, 323-334.

Meng, X., 2010. Summary Report of the Hydraulic Fracturing Opertation for the Shenhua CCS Project (internal report in Chinese). Anton Oilfield Services (Group) Ltd.

Min, K.B., Jing, L.R., Stephansson, O., 2004. Determining the equivalent permeability tensor for fractured rock masses using a stochastic REV approach: Method and application to the field data from Sellafield, UK. Hydrogeology Journal 12, 497-510.

Morris, J.P., Hao, Y., Foxall, W., McNab, W., 2011. A study of injection-induced mechanical deformation at the In Salah CO 2 storage project. Int J Greenh Gas Con 5, 270-280.

Mualem, Y., 1976. A new model for predicting the hydraulic conductivity of unsaturated porous media. Water Resour. Res 12, 513-522.

Nakashima, T., Sato, K., Arihara, N., Yazawa, N., 2000. Effective permeability estimation for simulation of naturally fractured reservoirs, SPE Asia Pacific Oil and Gas Conference and Exhibition.

Narr, W., Schechter, D.S., Thompson, L.B., 2006. Naturally fractured reservoir characterization. Society of Petroleum Engineers.

Nilsen, H.M., Herrera, P.A., Ashraf, M., Ligaarden, I., Iding, M., Hermanrud, C., Lie, K.-A., Nordbotten, J.M., Dahle, H.K., Keilegavlen, E., 2011. Field-case simulation of CO_2-plume migration using vertical-equilibrium models. Energy Procedia 4, 3801-3808.

Norden, B., Frykman, P., 2013. Geological modelling of the Triassic Stuttgart Formation at the Ketzin CO_2 storage site, Germany. Int J Greenh Gas Con 19, 756-774.

Oda, M., 1985. Permeability Tensor for Discontinuous Rock Masses. Geotechnique 35, 483-495.

Odling, N.E., 1992. Permeability of natural and simulated fracture patterns, structural and tectonic modelling and its application to petroleum geology,. NPF Special Publication 1, 365-380.

Pan, L., Webb, S.W., Oldenburg, C.M., 2011. Analytical solution for two-phase flow in a wellbore using the drift-flux model. Adv Water Resour 34, 1656-1665.

Parney, R., Cladouhos, T., La Pointe, P., Dershowitz, W., Curran, B., 2000. Fracture and production data integration using discrete fracture network models for carbonate reservoir management, South Oregon basin field, Wyoming, SPE Rocky Mountain Regional/Low-Permeability Reservoirs Symposium and Exhibition.

Paterson, L., Boreham, C., Bunch, M., Dance, T., Ennis-King, J., Freifeld, B., Haese, R., Jenkins, C., LaForce, T., Raab, M., 2013. Overview of the CO2CRC Otway residual saturation and dissolution test. Energy Procedia 37, 6140-6148.

Person, M., Banerjee, A., Rupp, J., Medina, C., Lichtner, P., Gable, C., Pawar, R., Celia, M., McIntosh, J., Bense, V., 2010. Assessment of basin-scale hydrologic impacts of CO_2 sequestration, Illinois basin. Int J Greenh Gas Con 4, 840-854.

Pham, T., Maast, T., Hellevang, H., Aagaard, P., 2011. Numerical modeling including hysteresis properties for CO 2 storage in Tubåen formation, Snøhvit field, Barents Sea. Energy Procedia 4, 3746-3753.

Phillips, S.L., 1981. A technical databook for geothermal energy utilization. Lawrence Berkeley National Laboratory.

Pruess, K., 1985. A practical method for modeling fluid and heat flow in fractured porous media. Society of Petroleum Engineers Journal 25, 14-26.

Pruess, K., 2005. ECO2N: A TOUGH2 Fluid Property Module for Mixtures of Water, NaCl, and CO2. Lawrence Berkeley National Laboratory, Berkeley, Calif.

Pruess, K., Garcia, J., Kovscek, T., Oldenburg, C., Rutqvist, J., Steefel, C., Xu, T., 2002. Intercomparison of numerical simulation codes for geologic disposal of CO2. Lawrence Berkeley National Laboratory.

Pruess, K., Narasimhan, T.N., 1985. A practical method for modeling fluid and heat flow in fractured porous media. Old SPE Journal 25, 14-26.

Pruess, K., Oldenburg, C., Moridis, G., 1999. TOUGH2 USER'S GUIDE, Version 2.0. Lawrence Berkeley National Laboratory, Berkeley, Calif.

Quandalle, P., Sabathier, J., 1989. Typical features of a multipurpose reservoir simulator. SPE reservoir Engineering 4, 475-480.

Raziperchikolaee, S., Alvarado, V., Yin, S., 2013. Effect of hydraulic fracturing on long-term storage of CO_2 in stimulated saline aquifers. Appl Energ 102, 1091-1104.

Rinaldi, A.P., Rutqvist, J., 2013. Modeling of deep fracture zone opening and transient ground surface uplift at KB-502 CO_2 injection well, In Salah, Algeria. Int J Greenh Gas Con 12, 155-167.

Ringrose, P., Atbi, M., Mason, D., Espinassous, M., Myhrer, Ø., Iding, M., Mathieson, A., Wright, I., 2009. Plume development around well KB-502 at the In Salah CO_2 storage site. First break 27.

Rutqvist, J., Vasco, D.W., Myer, L., 2010. Coupled reservoir-geomechanical analysis of CO_2 injection and ground deformations at In Salah, Algeria. Int J Greenh Gas Con 4, 225-230.

Senel, O., Will, R., Butsch, R.J., 2014. Integrated reservoir modeling at the Illinois Basin–Decatur Project. Greenhouse Gases: Science and Technology 4, 662-684.

Shi, J.-Q., Imrie, C., Sinayuc, C., Durucan, S., Korre, A., Eiken, O., 2013. Snøhvit CO 2 storage project: Assessment of CO 2 injection performance through history matching of the injection well pressure over a 32-months period. Energy Procedia 37, 3267-3274.

Singh, V.P., Cavanagh, A., Hansen, H., Nazarian, B., Iding, M., Ringrose, P.S., 2010. Reservoir modeling of CO_2 plume behavior calibrated against monitoring data from Sleipner, Norway, SPE annual technical conference and exhibition. Society of Petroleum Engineers.

Span, R., Wagner, W., 1996. A new equation of state for carbon dioxide covering the fluid region from the triple‐point temperature to 1100 K at pressures up to 800 MPa. Journal of physical and chemical reference data 25, 1509-1596.

SPTEGI, 2011. Construction Summary Report of 2011 for Monitoring Equipment and Service Provided to SHCCS Demonstration Project (internal report in Chinese). SPT Energy Group Inc.

SPTEGI, 2012. Construction Summary Report of 2012 for Monitoring Equipment and Service Provided to SHCCS Demonstration Project (internal report in Chinese). SPT Energy Group Inc.

SPTEGI, 2013. Construction Summary Report of 2013 for Monitoring Equipment and Service Provided to SHCCS Demonstration Project (internal report in Chinese). SPT Energy Group Inc.

SPTEGI, 2014. Construction Summary Report of 2014 for Monitoring Equipment and Service Provided to SHCCS Demonstration Project (internal report in Chinese). SPT Energy Group Inc.

Spycher, N., Pruess, K., 2005. CO_2 -H_2O Mixtures in the Geological Sequestration of CO_2. II. Partitioning in Chloride Brines at 12-100 ^oC and up to 600 bar. Geochim. Cosmochim. Acta 69, 3309-3320.

Teimoori, A., Chen, Z., Rahman, S., Tran, T., 2003. Calculation of permeability tensor using boundary element method provides a unique tool to simulate naturally fractured reservoirs, SPE Annual Technical Conference and Exhibition.

Underschultz, J., Boreham, C., Dance, T., Stalker, L., Freifeld, B., Kirste, D., Ennis-King, J., 2011. CO_2 storage in a depleted gas field: an overview of the CO2CRC Otway Project and initial results. Int J Greenh Gas Con 5, 922-932.

USEPA, 2012. Carbon Dioxide Capture and Sequestration. United States Environmental Protection Agency.

van der Meer, L.G.H., 1992. Proceedings of the First International Conference on Carbon Doxide Removal Investigations regarding the storage of carbon dioxide in aquifers in the Netherlands. Energ Convers Manage 33, 611-618.

van Genuchten, M.T., 1980. A Closed-Form Equation for Predicting the Hydraulic Conductivity of Unsaturated Soils. Soil Sci Soc Am J 44, 892-898.

Vasco, D., Ferretti, A., Novali, F., 2008. Estimating permeability from quasi-static deformation: Temporal variations and arrival-time inversion. Geophysics 73, O37-O52.

Vasco, D., Rucci, A., Ferretti, A., Novali, F., Bissell, R., Ringrose, P., Mathieson, A., Wright, I., 2010. Satellite - based measurements of surface deformation reveal fluid flow associated with the geological storage of carbon dioxide. Geophysical Research Letters 37.

Wang, Y., Zhang, H., Sun, C., Cui, L., Hu, J., Zhou, L., Chen, L., Sun, Y., Li, W., He, Q., Li, C., Liu, Y., Gu, Y., Fang, H., 2010. Environmental Impact Assessment of Shenhua 100000 tons/year CO_2 Capture and Storage Demenstration Project (in Chinese). Hydrogeology, Geotechnics and Environmental Geology Survey of Jinlin Province, China.

Warren, J.E., Root, P.J., 1963. The behavior of naturally fractured reservoirs. Society of Petroleum Engineers Journal 3, 245-255.

Wei, N., Gill, M., Crandall, D., McIntyre, D., Wang, Y., Bruner, K., Li, X., Bromhal, G., 2014. CO_2 flooding properties of Liujiagou sandstone: influence of sub - core scale structure heterogeneity. Greenhouse Gases: Science and Technology 4, 400-418.

White, C.M., Strazisar, B.R., Granite, E.J., Hoffman, J.S., Pennline, H.W., 2003. Separation and capture of CO2 from large stationary sources and sequestration in geological formations - Coalbeds and deep saline aquifers. J Air Waste Manage 53, 645-715.

Wiese, B., Böhner, J., Enachescu, C., Würdemann, H., Zimmermann, G., 2010. Hydraulic characterisation of the Stuttgart formation at the pilot test site for CO_2 storage, Ketzin, Germany. Int J Greenh Gas Con 4, 960-971.

Woodbury, A., Zhang, K., 2001. Lanczos method for the solution of groundwater flow in discretely fractured porous media. Adv Water Resour 24, 621-630.

Wu, X., 2014. Shenhua Group's carbon capture and storage (CCS) demonstration. Mining Report 150, 81-84.

Wu, Y., Forsyth, P., Jiang, H., 1996. A consistent approach for applying numerical boundary conditions for multiphase subsurface flow. Journal of Contaminant Hydrology 23, 157-184.

Würdemann, H., Möller, F., Kühn, M., Heidug, W., Christensen, N.P., Borm, G., Schilling, F.R., 2010. CO2SINK—From site characterisation and risk assessment to monitoring and verification: One year of operational experience with the field laboratory for CO_2 storage at Ketzin, Germany. Int J Greenh Gas Con 4, 938-951.

Xiao, X., Zhao, B., Thu, Z., Song, Z., Wilkins, R., 2005. Upper Paleozoic petroleum system, Ordos Basin, China. Mar Petrol Geol 22, 945-963.

Xie, J., Zhang, K., Hu, L., Pavelic, P., Wang, Y., Chen, M., 2015a. Field-based simulation of a demonstration site for carbon dioxide sequestration in low-permeability saline aquifers in the Ordos Basin, China. Hydrogeol J, 1-16.

Xie, J., Zhang, K., Hu, L., Wang, Y., Chen, M., 2015b. Understanding the carbon dioxide sequestration in low‐permeability saline aquifers in the Ordos Basin with numerical simulations. Greenhouse Gases: Science and Technology.

Yang, Y., Li, W., Ma, L., 2005. Tectonic and stratigraphic controls of hydrocarbon systems in the Ordos basin: A multicycle cratonic basin in central China. Aapg Bull 89, 255-269.

YLHYOIL, 2010. Feasibility Study of Shenhua 100000 ton/year Carbon Capture and Storage Project - Underground Part (Internal Report in Chinese). Beijing YilongHengye Oil Engineering Technical Co., Ltd.

Zhang, K., Ling, L., Wang, Y., 2012. Modeling Approaches for Wellbore Boundary Conditions for Simulation of CO_2 Geologic Sequestration in Saline Aquifers, TOUGH Symposium, Berkeley, California, USA.

Zhang, K., Woodbury, A., Dunbar, W., 2000. Application of the Lanczos algorithm to the simulation of groundwater flow in dual-porosity media. Adv Water Resour 23, 579-589.

Zhang, K., Woodbury, A.D., 2000. The Arnoldi reduction technique for efficient direct solution of radionuclide decay chain transport in dual-porosity media. Journal of contaminant hydrology 44, 387-416.

Zhang, K., Woodbury, A.D., 2002. A Krylov finite element approach for multi-species contaminant transport in discretely fractured porous media. Adv Water Resour 25, 705-721.

Zhang, K., Wu, Y.-S., Pruess, K., 2008. User's guide for TOUGH2-MP-A massively parallel version of the TOUGH2 code. Lawrence Berkeley National Laboratory, Berkeley, Calif.

Zhou, Q.L., Birkholzer, J.T., Mehnert, E., Lin, Y.F., Zhang, K., 2010. Modeling Basin- and Plume-Scale Processes of CO_2 Storage for Full-Scale Deployment. Ground Water 48, 494-514.